© 2017 Erik Ziehm

ION-CATHODE BOMBARDMENT FOR THE CREATION OF TIGHTLY BOUND DEUTERIUM CLUSTERS IN PALLADIUM

BY

ERIK ZIEHM

THESIS

Submitted in partial fulfillment of the requirements
for the degree of Master of Science in Nuclear, Plasma, and Radiological Engineering
in the Graduate College of the
University of Illinois at Urbana-Champaign, 2017

Urbana, Illinois

Master's Committee:

Professor Emeritus George H. Miley, Adviser
Professor Jean Paul Allain

Abstract

A complementary approach of experimental and computational methods was used in pursuit of determining optimal ion bombardment parameters for the creation of deuterium clusters with high binding energies. The incident ions create damage cascades leading to the production of defects such as vacancies, dislocations, and voids. These defects are known to trap interstitial deuterium with binding energies dependent on the trap's geometry and volume.

To simultaneously obtain high concentrations of defects and hydrogen, a simple DC glow discharge method was employed. Deuterium ions bombarded a palladium cathode at varying fluences ($1\ x\ 10^{18}\ \text{ions/cm}^3, 1\ x\ 10^{19}\ \text{ions/cm}^3, \text{and}\ 1\ x\ 10^{20}\ \text{ions/cm}^3$) and incident energies dependent on cathode bias ($-0.75\ \text{kV}, -0.875\ \text{kV}, \text{and}\ -1.0\ \text{kV}$). Langmuir probe measurements of the Electron Energy Distribution Function (EEDF) validated a COMSOL simulation's accuracy which confirmed the proper methodology for reproducing discharge dynamics. The simulation was a sequential coupling between COMSOL's Plasma module and Boltzmann Equation, Two-Term Approximation module allowing for more exact calculations of the Townsend coefficients. Properly accounting for the Townsend coefficients is necessary to represent the kinetics of DC discharges with low ionization fractions and species mobility highly dependent on the electric field. With these corroborating results, the model was expanded to conditions where measuring plasma properties became no longer feasible.

The model produced Ion Angular Energy Distribution Functions (IAENDF) at the cathode which allowed for finding trends in Thermal Desorption Spectroscopy (TDS) curves. The desorption peaks centered around 600-800 K. There appeared to be a deuterium trapping limit dependent on defect concentration where once a distinct defect density was met any further damage was counterproductive to deuterium trapping. The

condition that produced the most trapped deuterium was -0.75 kV cathode bias in 1 Torr deuterium with a fluence of 1×10^{18} ions/cm^3.

To further investigate these TDS trends some samples were observed under SEM and TEM. The results showed surface pit and blister formations which grew in concentration as the fluence increased. Beneath the surface formations, cross-section images showed large voids and holes in the material with cracks at grain boundaries. TEM images displayed the resulting damage structure which extended ~250 nm into the cathode for a sample at 1.0 Torr and -1.0 kV. A proposal is that as the damage concentration increased, these voids grew to such an extent that they formed the blisters and eventually ruptured leading to the release of the trapped deuterium.

Acknowledgements

To my friend and uncle, David Ziehm: I owe you my love of scientific discovery and exploration. I cherish our long-lasting phone calls, Thank You!

I am incredibly fortunate to be a part of a research group led by Dr. George Miley. His wisdom, good judgment, persistence, and support have helped shaped me into the student and person I am today. It is under his guidance that I continually experience the rewards of research, and for that I am grateful. Thanks must also go out to the other group members: Matthew Bergschneider for his help with the Thermal Desorption Spectroscopy apparatus, Jacob Mayer for materials science and imaging advice, along with Tapan Patel, Shriji Barot, Zhiheng Xu, and Erik Smith.

I would also like to thank Dr. Jean Paul Allain for developing my interest in plasma-material interactions and the emergent phenomena therein. His insightful and encouraging comments have helped lay the foundations for future work.

Thanks must also be given to Industrial Heat, LLC and New York Community Trust for their support and funding this project. Lastly, this work was carried out in part in the Frederick Seitz Materials Research Laboratory Central Research Facilities, University of Illinois. I am in debt to the staff for hours spent on training and answering any questions.

Table of Contents

List of Figures and Tables

Chapter 1: Introduction

The pervasive nature of hydrogen interacting with metals has led to its study in a variety of disciplines. These range across physical chemistry, nuclear engineering, physics, and material science with a broad spectrum of topics such as fuel cells, hydrogen embrittlement, superconductivity, fusion and fission reactors, and inorganic catalysis [1]. Since the metal-hydrogen system is ubiquitous, it is only natural for it to be relevant to so many applied sciences. However, it also holds ground in a much broader sense - it stands as an ideal prototype to investigate fundamental phenomena such as non-stoichiometric compounds (the first measurements of a nonstoichiometric system were from hydrogen-palladium), the dynamics of solid state diffusion, and the theories of dislocations and interstitials [2]. Currently, a common interest is the trapping of hydrogen to defects in metals, which is the primary concern in this thesis.

Hydrogen is the lightest, smallest, and most abundant element, coupling this to its reactivity, makes the metal-hydrogen interaction inescapable. As previously stated, its effects appear across an extensive area forming a rich gestalt of relevant topics. Figure 1 attempts to provide a brief demonstration of applications along with areas of fundamental science that were studied through the use of the metal-hydrogen system. This distinction between application and fundamental science is arbitrary; the purpose is to display that some metal-hydrogen systems had well defined applicable objectives such as metal-hydride heat pumps while others acted as tools to study fundamental principles such as solid-state diffusion. Even further still, some straddled the distinction presenting a useful application while simultaneously granting edification of basic research. It should be noted here that when the term hydrogen is used, it is referring to all of the hydrogen isotopes unless stated otherwise.

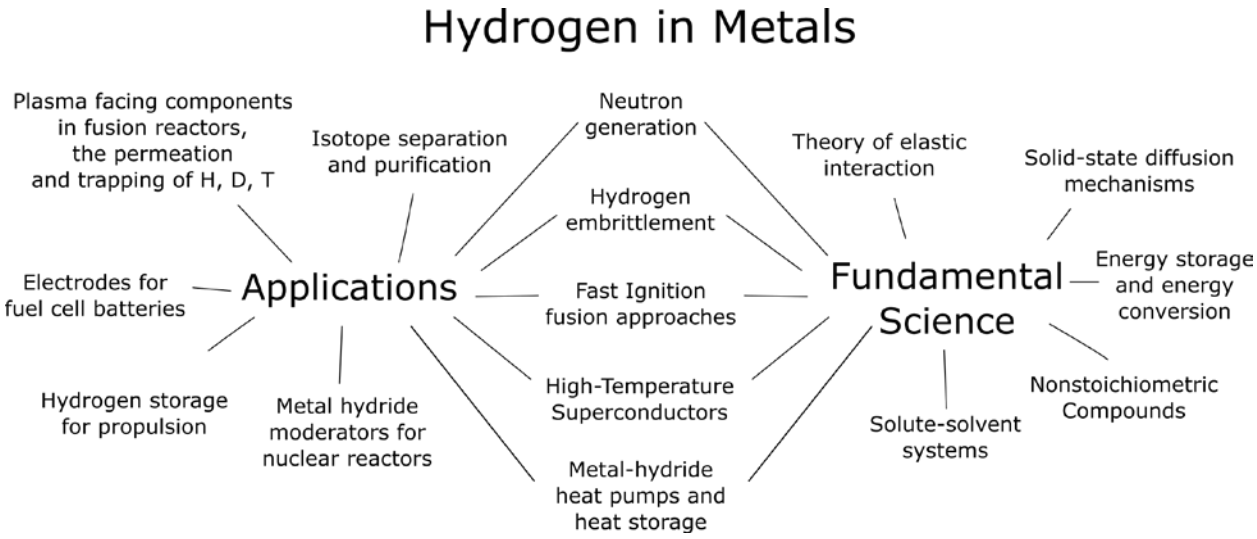

Figure 1. Metal-hydrogen applications and influenced fundamental sciences [4] - [7].

Each of these topics deals with understanding the role of hydrogen within the system - be it optimizing its concentrations, determining trapping mechanisms, changing the interstitial solubility and mobility characteristics, etc. Displaying Figure 1 as a web emphasizes the widespread value of the metal-hydrogen field and how gaining an understanding of one fundamental aspect of a simple system benefits the whole allowing for application in other more complicated cases. At present, most research is in the property of metal defects to trap and store hydrogen. The importance of understanding these characteristics is explicitly seen in the technological developments in the fusion sciences. Within large-scale fusion devices, high fluxes of hydrogen ions interact with plasma facing materials which simultaneously affects the materials' mechanical properties and the plasma properties. The role of hydrogen solubility, diffusion, and re-emission from the plasma facing materials is therefore of importance for the understanding and longevity of the device [4].

A traditional choice for studying the metal-hydrogen system is palladium due in part to its affinity for the absorption of hydrogen at room temperature, i.e. its high solubility and mobility for interstitial hydrogen. These properties allow to quickly and reliably obtain

hydrogen concentrations along with any material property changes that result as shown in the first record of the palladium-hydrogen system by Graham in 1866 [5]. It wasn't until 1932 where Wagner [6] suggested the absorption proceeded with at least two steps: the dissociation and chemisorption of hydrogen molecules at the material surface, and then the passage of hydrogen atoms from surface sites into the bulk lattice. The general equation as seen in (1.1) transitioned to a multi-step one, (1.2)

$$\frac{1}{2}xH_2 + M \rightleftarrows MH_x \tag{1.1}$$

$$H_2 \rightleftarrows 2H_{ad} \quad \rightarrow \quad xH_{ad} \rightleftarrows MH_x \tag{1.2}$$

Where H_2 is in the gaseous phase, H_{ad} is the adsorbed hydrogen, M is a general metal atom, and x is the atomic ratio [H]/[Pd]. At thermodynamic equilibrium, the rate-limiting step in this absorption process is the dissociation of the hydrogen molecule to two atoms on the Pd surface [7]. Once the hydrogen is inside the metal, it occupies interstitial sites in the lattice leading to these systems often being referred as interstitial alloys.

In order to study the properties of hydrogen-defect interactions, the formation of defects must be understood. It is possible to produce defects in metals via a variety of methods ranging from mechanical to chemical means. The most traditional technique is cold-working the material where the sample is deformed in the absence of heat typically at ambient temperatures resulting in an increased dislocation density. Cryomilling is a similar technique for creating defects in a material, deforming and pulverizing the sample into micro and nanoparticles while at cryogenic temperatures. Another method is the cycling through the phases of the metal hydride. However, a subsequent chapter covers this. For now, suffice it to say, the cryomilling and cold-working techniques create inhomogeneous distributions of dislocations in the crystal whereas hydride cycling creates dislocations more evenly dispersed and at higher densities [8].

There is an alternate approach for introducing defects into a material via plasma ion implantation which is the approach chosen in this thesis. If hydrogen is selected as the source gas, the method can be seen as a type of plasma electrolysis where a direct-current discharge is formed between two electrodes - the cathode being the desired target material. The plasma simultaneously introduces hydrogen into the metal while damaging it producing defects via primary knock on damage. The plasma methods are useful in their abilities to create non-equilibrium concentrations of hydrogen in the material producing stress on the lattice. The combination of the added stress and the damage produced by the ion's athermal interactions affects thermodynamic quantities such as vacancy production energy barriers and leads to further defect creation [9]. A strong coupling then appears between the non-equilibrium hydrogen conditions, athermal collisional effects, and the local thermodynamic equilibrium of the system which leads to a different rate-limiting step than that of hydrogen dissociation in (1.2). The new rate-limiting step is then dependent on the properties of the metastable non-equilibrium hydrogen concentrations in the material as it interacts with incident ions resulting in an altered rate of hydrogen diffusion and emission back out of the surface.

The plasma conditions can then control the incident energies of the ions to a certain degree. If the plasma sheath is collisionless, the ions will gain a kinetic energy equal to the potential energy drop in the sheath as they collide with the cathode. If the plasma is within the collisional regime, this method has the benefit of producing low energy incident ions - ~2 eV - at fluxes high enough where obtaining typical fluences on the order of $1 \times 10^{18} - 1 \times 10^{20}$ ions/cm^2 is not cumbersome. These fluences allow easily reaching hydrogen concentrations which are sufficient enough to be detected using TDS. However, within both regimes, the energy distributions are far broader compared to a collimated ion beam method which has finer tuning of the desired ion energies. Another disadvantage of this method is the difficulty in understanding the creation of the defects via both

incident ion damage and interstitial hydrogen atoms interacting with the lattice. Lastly, it can be difficult to accurately quantify the fluence as the treatment continues due to sputtering of the material coating any holder and increasing the electrode area.

While the primary principles are the same for other metal-hydrogen systems such as the thermodynamic laws governing heat of solution and chemical potential, the primary focus of this thesis is on the palladium-hydrogen system. And so these topics are presented in such context. The presented background on the properties of hydrogen absorption is beneficial in obtaining a phenomenological understanding of the creation and measurement of bound hydrogen clusters and so is introduced first. Then the method of ion implantation and irradiation damage are covered concerning defect formation. Finally, a brief overview of TDS is included.

1.1 Palladium - Hydrogen Properties

Palladium is a group 10 transition metal with a face-centered cubic (FCC) unit cell as seen in Figure 2 below.

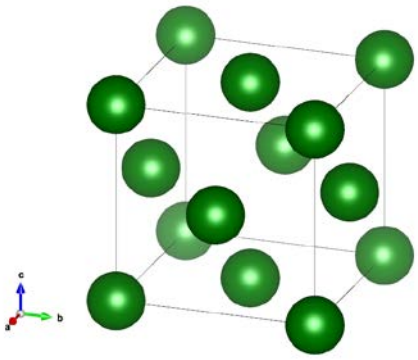

Figure 2. Palladium FCC unit cell created in the Visualization for Electronic and Structural Analysis software (VESTA) [10]

It has an electron configuration of $[Kr]4d^{10}$ which becomes relevant in the explanation of its hydrogen solubility and diffusivity. Hydrogen absorption into the Pd FCC lattice has been well documented throughout the years, and there were - and still are - many

questions as to how a hydrogen molecule enters the palladium crystal structure. How does the orientation of the molecule and the material's open surface structure affect the absorption rate? What happens to the hydrogen once absorbed? Under what framework is the metal-hydrogen system best described, i.e. is bringing in quantum mechanical effects necessary? With recent techniques such as Electron Energy Loss Spectroscopy (EELS) and Low Energy Electron Diffraction (LEED) complimented with TDS and ab initio modeling these questions can be probed directly.

Using these methods, Okuyama et al. put forth a valuable study on the absorption path of hydrogen. He focused on H_2 absorption through the (100) plane, and his results corroborated the previous theories on the reaction pathways [11]. He proposed a simple model for the absorption process with the hydrogen first dissociating to chemisorb to the (100) surface, penetrating through the surface past a tetrahedral site to an octahedral site, then migrating further into the bulk. However, as previously depicted by Wagner [6], this was not the first proposal of a hydrogen absorption pathway. The significance lies in its methods of detection to support the theory and on the specific lattice plane on which hydrogen absorbed. Similar channels were found for the absorption of H_2 on the (111) plane of Pd and complemented by a Density Functional Theory approach. They showed that the absorption of the hydrogen molecule on the (111) site had a lower activation energy than the (100) site [12]. To better visualize the different lattice planes Figure 3 displays a Pd cell with varying planes on the topmost layer. It highlights two types of volumetric cells that exhibit symmetry - the tetrahedral and octahedral sites. Tetrahedral sites are composed of four atoms with fourfold symmetry while octahedral sites have six atoms with sixfold symmetry. The octahedral sites contain a larger volume than the tetrahedral ones which contributes to hydrogen's preference for the octahedral site [13].

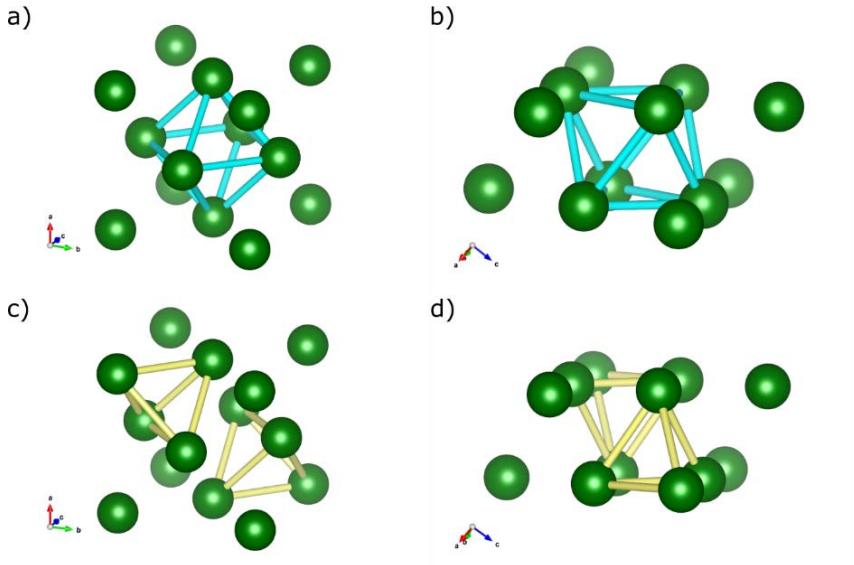

Figure 3. Pd FCC crystals with varying lattice plane orientations. (a) Blue octahedral cell with a (100) upper surface plane (b) Blue octahedral cell with a (111) upper surface plane (c) Two yellow tetrahedral cells with a (100) upper surface plane (d) Two yellow tetrahedral cells with a (111) upper surface plane

Computational modeling is another topic where the palladium-hydrogen system was at the forefront. The Pd-H system was the first stoichiometric metal-hydrogen system on which electron band calculations were done [7]. These calculations transitioned to microscopic modeling methods such as effective-medium theory and the embedded-atom model. The effective-medium theory replaces the multi-component metal lattice with a smoothed out effective medium for which it is possible to perform self-consistent quantum mechanical calculations. The medium is typically a homogeneous electron gas with corrections applied using perturbation theory to account for the lattice structure. The embedded-atom model expands upon this allowing one to embed an atom into the medium and calculate its energy landscape [4].

Using these computational methods, eventually, a consensus was met over the bonding between Pd-H and some of its properties. Notably, once hydrogen is inside Pd, a charge transfer occurs from Pd-Pd bonds to nearby regions containing hydrogen. Nørskov [14] utilizing a type of effective-medium model calculated the electronic states of hydrogen and showed that the electron density distribution around the hydrogen atom made it more

similar to an H^- anion. The charge transfer takes place between the H 1s and Pd 4d orbitals forming a hybridization state between them, i.e. a superposition of two independent orbitals with the emergence of a new orbital with a new energy and shape. The hybridization not only creates new orbitals for the electrons to occupy but can dramatically broaden the d orbital. While the H 1s electron wavefunction can be considered delocalized through the hybridization, the new Pd-H bonding wavefunction is deemed to be localized inside the host lattice. Therefore it does not extend past the nearest neighbor metal atoms [4][7].

With the progression of computational power came an increase in complexity of the modeling methods used. Implementations of DFT are seen as successors to the effective-medium and embedded-atom models. It is useful in its ability to capture the potential energy structure of crystalline lattices and how the kinetics are affected ab initio. DFT studies can take quantum mechanical effects into account and implement them into effective band theory by approximating the Schrödinger wave equation for electrons in a self-consistent way [4]. This is particularly vital for approximating the hydrogen-metal system as hydrogen's low mass and size lead to a wavefunction on the order of ~0.8 Å which is comparable to the distance between octahedral and tetrahedral sites. The similar lengthscales then allow for the possibility of tunneling to occur [4]. Incorporating this effect along with the aforementioned delocalized H 1s electron wavefunction and localized Pd-H bonding wavefunction into a simulated study is, therefore, a drastic improvement to accurately represent the system. However, calculating this with high precision takes a significant amount of computational power which constrains the simulated space to 10-100 atoms with periodic boundary conditions imposed to simulate larger volumes. Another shortcoming of the DFT technique is its restriction to a static configuration with no time dependence, i.e. the simulations assume everything is in the ground state at 0 K. These downsides coupled with inherent assumptions on the chosen form of the structures can

lead to erroneous results [4]. The resulting volumetric electronic data from the DFT study is often then applied to a molecular dynamics simulation which allows for dynamic studies of larger scale atomistic systems.

DFT studies have shed light on the unique molecular orientation dependence on the activation energies for absorption. Roques et al. focused their DFT study on the dissociative adsorption of molecules on small palladium clusters Pd_n with $5 \leqslant n \leqslant 10$ [15]. The hydrogen molecules followed the same process as Okuyama et al. proposed, but with an added step of depicting physisorption above the surface layer of Pd atoms. Physisorption is where the adsorbed molecule is weakly bound to the surface due to Van der Waals forces and no charge transfer occurs. DFT studies found in [12] showed further insight into a caveat on the potential energy surface of Pd (111): that for molecules with their axis perpendicular to the surface the interaction is repulsive and no absorption takes place. They also showed that the dissociation energies were highly dependent on where the molecule approached the Pd surface atoms. A molecule nearing the bridge site, Figure 4, with its axis pointing toward a hollow site can dissociate immediately without any barrier. While a molecule nearing the on-top site first is attracted to the surface plane of the Pd atoms, but then an activation energy is needed for dissociation. This all shows the unique dependence on the path of approach for hydrogen molecule absorption.

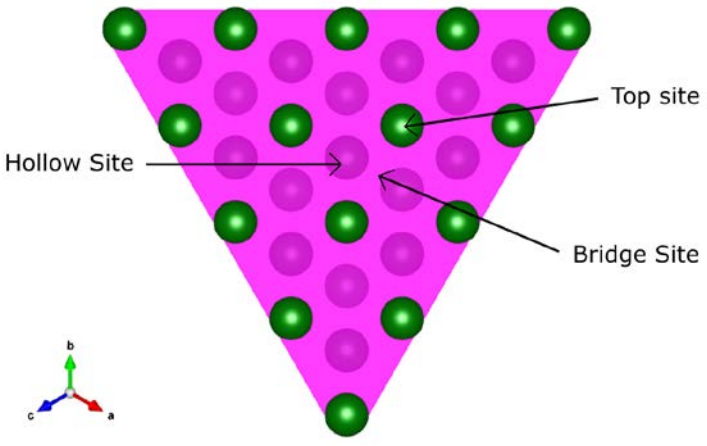

Figure 4. Site locations on Pd looking down [111] direction with (111) plane highlighted

While these DFT studies resulted in valuable quantitative information like estimates for the heat of solution, diffusion activation barrier, and electronic band structures, the purpose of including them here is to show a qualitative understanding of the absorption process. That it depends on not only the geometrical structure of the adsorbing molecule and host palladium lattice, but there is a simultaneous importance on the electronic structure. Both contribute to the dynamics of the palladium-hydrogen system and while not previously stated both can be taken into account through various assumptions, e.g. density of defects, interatomic potential calculations being classical or including quantum mechanical effects, etc. As a visual aid, an example of hydrogen absorption through the (100) face of palladium was chosen - Figure 5. The (100) face was selected as the plane of absorption not because it is the most abundant surface plane - the densely packed (111) plane is [7] - but because it is the most visually forthright. The electron densities are also plotted on 2D slices for the (100) and (200) planes which include the contribution from the hydrogen atom. They were calculated through VESTA which utilizes a Fourier transform of structure factors derived from structure parameters and atomic scattering factors [10]. The electron density takes the form of

$$\rho(x,y,z) = \frac{1}{V} \sum_{h=-\frac{N_x}{2}}^{\frac{N_x}{2}} \sum_{k=-\frac{N_y}{2}}^{\frac{N_y}{2}} \sum_{l=-\frac{N_z}{2}}^{\frac{N_z}{2}} F(h)\exp[-2\pi i(hx+ky+lz)] \qquad (1.3)$$

where N_x, N_y, and N_z designate the number of grids along each crystallographic axis.

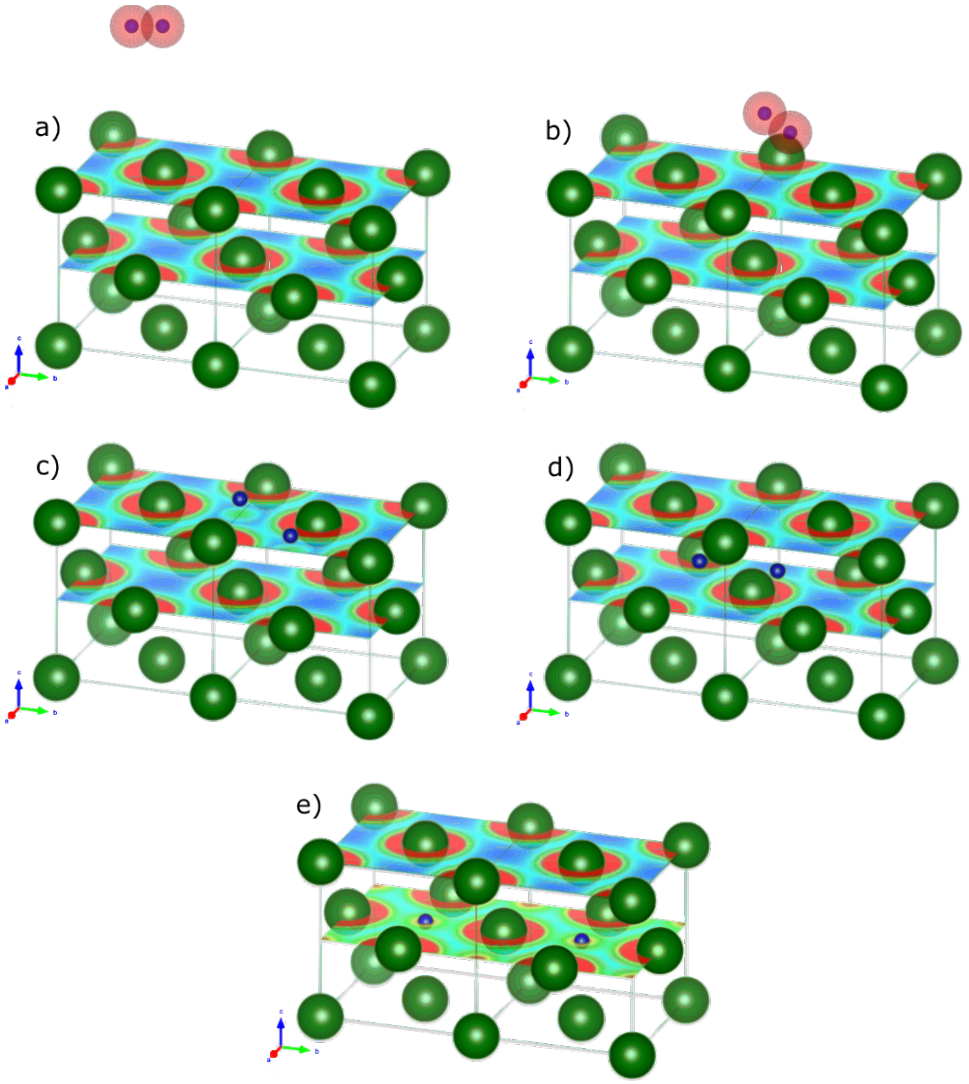

Figure 5. Representation of hydrogen absorption (blue atoms) through the (100) Pd plane. (a) Hydrogen approaches the (100) face (b) Physisorption occurs with no charge transfer (c) Dissociation and chemisorption at a surface octahedral site (d) Transit into the subsurface tetrahedral site (e) Hydrogen stable in the octahedral site

For parts (a) and (b) red spheres were superimposed on the image to represent the molecules electron cloud. They were removed for (c)-(e) as the hydrogen's electrons are donated to the conduction band, and the influence of the hydrogen atom on the lattice electron density was subsequently calculated through VESTA [4]. For (e) the electron density was calculated assuming a hydrogen atom at every octahedral site producing a periodic boundary. The process depicted is as follows

a) Hydrogen molecule is approaching the (100) Pd face.

b) Physisorption with no charge transfer takes place at a bridge surface site.

c) Dissociation and chemisorption of individual hydrogen atoms at a surface octahedral site.

d) Hydrogen atoms diffuse into the lattice transiting a tetrahedral site.

e) Hydrogen situates itself at the octahedral site with electrons shielding it.

Once the hydrogen atom reaches the octahedral location, it can diffuse into the bulk or remain bound to the subsurface.

1.1.1 Palladium Hydride Phases

With the palladium-hydrogen system often being referred to as an interstitial alloy it should come as no surprise that it has a characteristic phase diagram. Its phase diagram - typically along with other metal-hydrogen systems - shows characteristics of a single component lattice gas—lattice liquid system [1]. Early studies on palladium-hydrogen systems showed that the interstitial hydrogen deforms the lattice which creates attractive long-range strain fields, i.e. at long ranges, two interstitials attract one another in the crystal lattice. As more hydrogen enters the lattice, the strain energy increases and at a critical value palladium has a lower Gibbs free energy if it separates into two phases: diffuse α phase and a high concentration β phase [1]. The phase diagram is shown in Figure 6 below

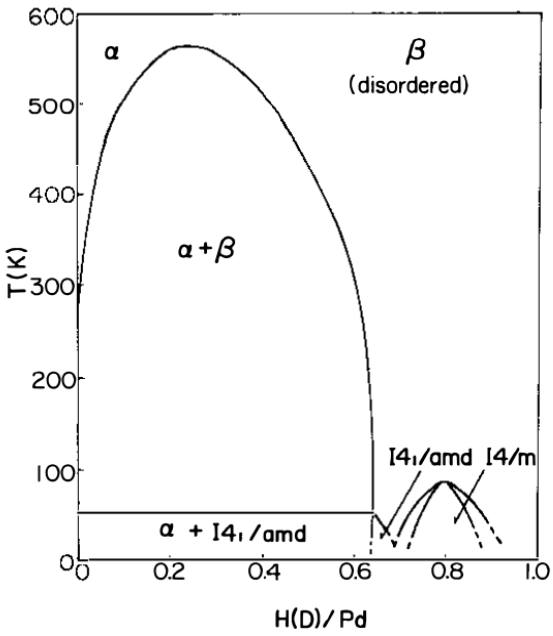

Figure 6. Pd-H phase diagram. At 298 K, α $[H]/[Pd]_{max} \approx 0.015$ and β $[H]/[Pd]_{max} \approx 0.7$ [16]

Both α and β phases have the FCC structure of the original palladium lattice; only the lattice constants change which are shown below in Table 1. The low temperature ordered phases also share the FCC structure, but the Pd atoms positions are undistorted relative to the distorted other phases at the same hydrogen concentration [16]. These have not been given proper names.

Table 1. Lattice constants for pure palladium and palladium hydride phases where x = [H]/[Pd] [1][6]

Phase	Lattice Constant (Å)
Pure Pd	3.890
α phase with PdH_x ($x \leq 0.015$ - 0.025)	3.894
β phase with PdH_x ($x \geq 0.6$ - 0.7)	4.025

The α phase is considered to be a disordered solid solution of hydrogen while the β phase is more ordered and stable. The β phase contains hydrogen atoms that are packed densely enough where H-H interactions come into effect and result in the increased lattice expansion [1]. As previously stated it was found that for both phases hydrogen atoms

occupy the octahedral sites of the Pd lattice as verified through neutron diffraction [7]. Between ~0.015 < x < ~0.6 there is a mixture of the two hydride phases and what is interesting is the discontinuous lattice constant expansion during the first-order phase transition from the α to β phase. These changes in lattice constants correlate to volume expansion of the Pd lattice by 10.4%. However, it does not take place uniformly at all points. The anisotropic expansion leads to increased stress and the generation of defects such as vacancies and dislocations [1], [17]. To further exemplify the transition from the α to β phase see Figure 7.

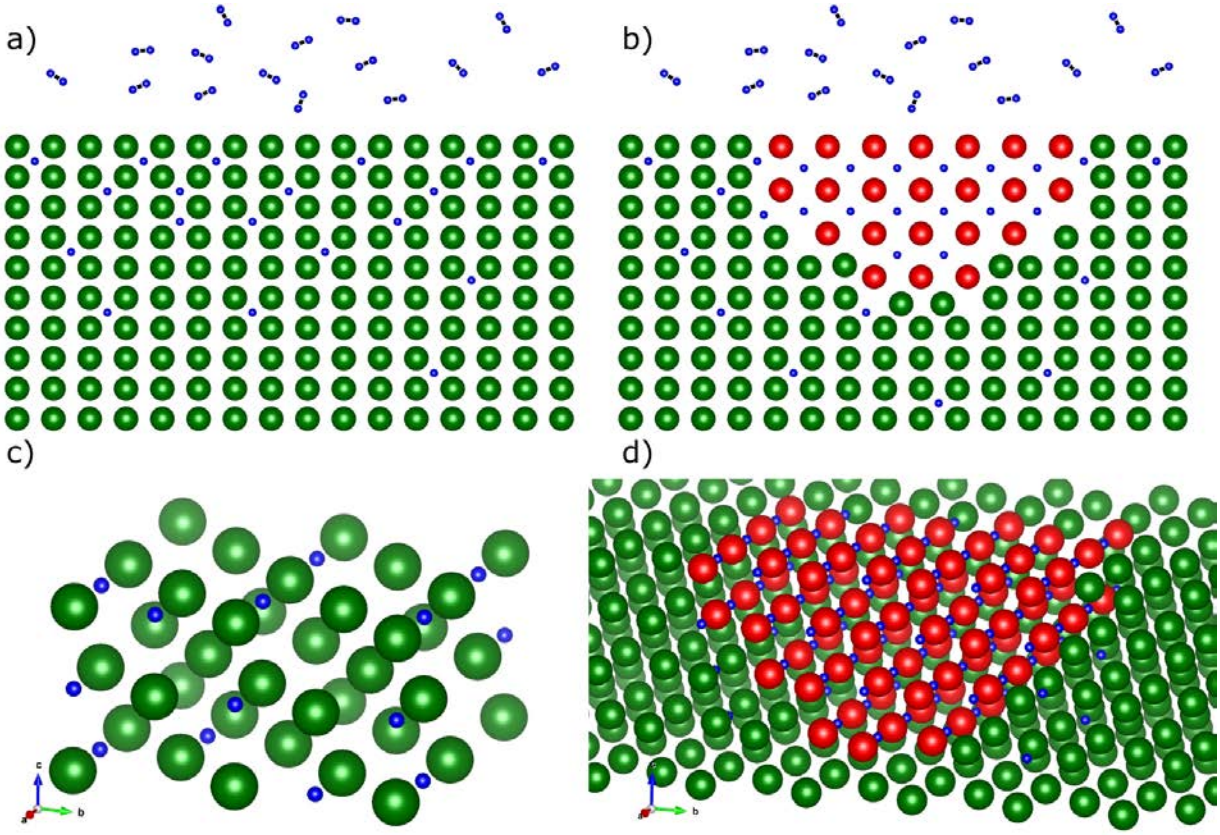

Figure 7. Representation of the α (green) and β (red) phases in Pd. (a) Low concentration of interstitial hydrogen atoms form the solid solution alpha phase (b) An increasing concentration leads to lattice expansion and the nucleation of the ordered beta phase; Lattice constant mismatch is exaggerated (c) and (d) show the 3D representation of (a) and (b) respectively

The exchange of hydrogen between the surrounding environment's atmosphere and the metal must be taken into account when making phase diagrams like Figure 6 for PdH_x and similarly for other metal-hydrogen systems. The hydrogen concentration changes with temperature and pressure, so unlike solid-solid alloy systems, the hydrogen concentration is not stable with varying temperature. To circumvent this and construct the phase diagram, isothermal measurements are taken for the equilibrium composition as a function of pressure. The resulting plots are called p-c-T diagrams (or p-x-T) for pressure-composition-isotherms [4], [7]. Electrical resistivity relationships commonly determine the hydrogen concentration within the solid while under pressure. The resistance of the material increases as the hydrogen concentration increases until the β phase develops and the resistance drops slightly - explained by the adverse effects of disorder on conduction [18]. Other methods include gas volumetry and gravimetric analysis. P-c-T diagrams are shown below for the PdD_x system in Figure 8. Following a curve for a single temperature, concentration in the α phase slowly increases with increasing pressure until $x \approx 0.01$ where an inflection point occurs and the curve plateaus. This region of gradually increasing pressure is known as the miscibility gap and implies that two phases coexist. The second inflection point designates the transition to the β phase. Connecting the inflection points of each isothermal curve creates the phase boundary for the system, i.e. each inflection point corresponds to its respective $\alpha \rightarrow \alpha + \beta$ or $\alpha + \beta \rightarrow \beta$ transition.

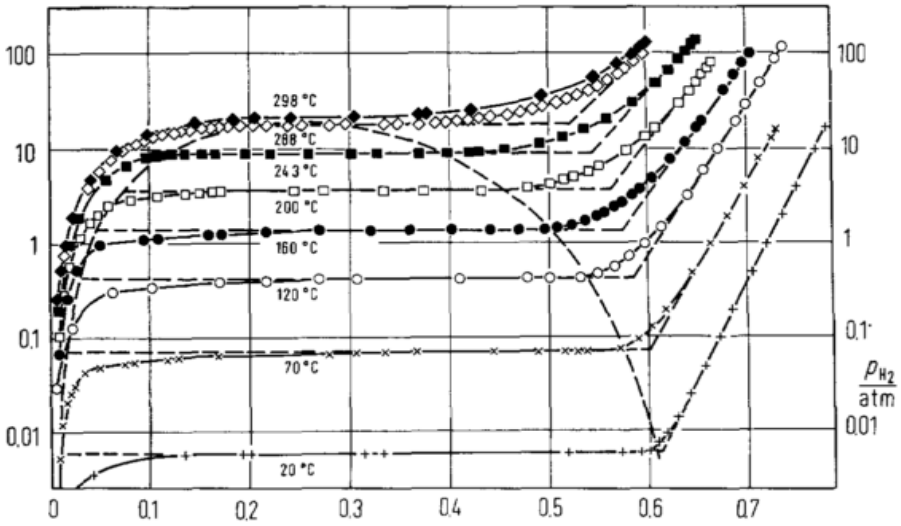

Figure 8. Pressure-Composition-Isotherms for PdH_x [7]

The p-c-T diagram in Figure 8 shows that getting to concentrations above $x \approx 0.7$ requires considerable pressures upwards of 10 - 100 atm or 1 - 10 MPa. Fukai and Okuma [19] presented a study on the formation of superabundant vacancy formations - 18 ± 3 at. % - via baking for 2 to 3 hours at $700 - 800^{\circ}C$ in a 5 GPa hydrogen atmosphere. In situ x-ray diffraction showed a two-phase separation of stoichiometric PdH and a vacancy-ordered phase Pd_3VacH_4 structure or $x \approx 1.33$. Mayerset al. [20] were able to reach PdD_x concentrations of $x > 1.0$ through the use of ion implantation at cryogenic temperatures which is similar to the methods used herein. Between 41 and 81 K and using a 10 keV D ion beam - which reaches a depth of ~100 nm - they reached concentrations as high as $x = 1.6 \pm 0.2$. The concentration was found through ion channeling where the technique makes use of MeV ions incident on a low-index crystal plane preferentially channeling through the open area between metal lattice planes. This reduces the backscattered ions and increases the average penetration depth as the ions become focused towards the minimum potential energy at the channel center. During the ion's transit of the channel, it interacts with interstitial atoms such as H and D through nuclear reactions, $H(^{11}B,\alpha)\alpha\alpha$

or D(^{3}He,p)α respectively. Reaction products measured for various orientations allow for the determination of the interstitial atom's site [4].

1.2 Ion-Metal Interactions

The effects of ion bombardment on a crystalline lattice have been an essential and well-studied topic for some time. As the incident ion collides with the host target, it locally deposits energy in the form of heat to the electronic bands and phonon vibrations which can induce lattice atom displacements and defect production. The disorder caused by this process is referred to as a collision cascade as the energetic ion goes through multiple ballistic collision events until it loses enough energy to come to thermal equilibrium with the host lattice. Despite the ion depositing energy to the electronic bands in the form of heat, the cascade is quenched to ambient temperatures on the order of 10^{-11} s and is considered of an athermal nature [21]. These lattice atoms that are displaced due to the incident ion are known as primary knock-on atoms (PKAs) and can further displace other atoms. The initial PKAs and their corresponding vacancies - collectively called a Frenkel-pair - are the primary source of damage from incident ion irradiation. This section focuses on the ion's ballistic damage, but it is crucial not to forget the coupling between the athermal effects resulting in the Frenkel-pair production and the local thermodynamic effects surrounding them.

The collision cascades take on varying characteristics depending on the incident ion species and energy. Some displaced atoms will transfer their momentum back to the surface of the material. If the energy of these backward recoiling atoms surpasses the surface binding energy - 3.91 eV for Pd - then they will break free from the surface and be sputtered. For an ion incident to the material's surface, the energy it can transfer to a stationary atom is given by

$$T = \frac{4M_1M_2}{(M_1 + M_2)^2} E_0 \sin^2 \frac{\theta_c}{2} \tag{1.4}$$

Where E_0 is the incident ion energy, M_1 is the incident ion mass, M_2 is the stationary atom mass, and θ_c is the target atom's scattering angle.

The transferred energy must be larger than the minimum displacement energy for the target material for Frankel-pair creation. For palladium, this is 25 eV as given by the software Stopping and Range of Ions in Matter (SRIM) [22] which matches closely with the given value of 26 eV in Nastasi et al. [21]. Using (1.4) it is seen that a minimum incident energy of 343 eV is required for the maximum transfer energy to equal the minimum displacement energy for Pd. As an example of the utility of SRIM, it is used to check the dependence of average vacancy creation (vacancy/ion) and sputtering yield (atoms/ion). The average vacancy/ion and sputtering yield are plotted in Figure 9 below.

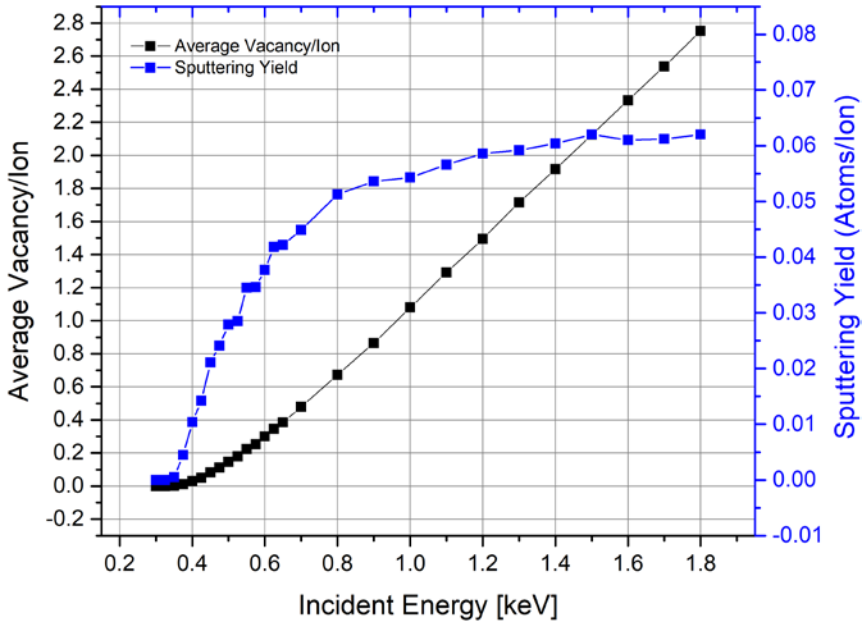

Figure 9. Average vacancy/ion and sputtering yield of deuterons on Pd using SRIM and 10,000 ions

Figure 9 shows that both sputtering yield and vacancy creation increase linearly up to ~500 eV. Then the sputtering yield seems to approach an asymptotic limit of ~0.07 while

the average vacancy/ion continues a linear trend. SRIM also produces lateral and longitudinal ranges in the material, and the longitudinal range increases with incident energy while the lateral range decreases. These results are helpful in estimating the damage characteristics of incident ions. However, it is only quantitative for a single given incident energy, i.e. incident energy distributions are not implemented in the software. Being able to execute incident ion energy distributions would be more realistic in recreating damage profiles resulting from ions traversing a plasma sheath as the ions will not have a discrete incident energy. Depending on the plasma characteristics, they can have a more Maxwellian distribution covering a broad range of energies.

1.3 Hydrogen - Defect Interaction

Every metal has an intrinsic equilibrium concentration of defects that play a significant role in the solubility and diffusivity of interstitial hydrogen. This relationship has been studied for decades and in 1973 Lynch et al. showed the absorption and desorption of interstitial hydrogen increased defect concentrations, i.e. hydrogen both interacts with and contributes to the production of defects [23]. Vacancies, dislocations, grain boundaries, voids, etc. each interact with the host lattice differently, and the resulting localized lattice dilation attracts interstitial hydrogen. This hydrogen affinity to defects (dislocations, vacancies, and voids) increases the material's hydrogen solubility [1], [16], [17], [23]-[25]. These defects have Arrhenius dependent mobilities and can combine to decrease the internal energy of the lattice, e.g. vacancies conglomerating to form vacancy complexes, which further complicates the system dynamics. Their influence alone is often the dominant factor in a material's properties which causes difficulties with deconvolving the effects and dynamics of hydrogen from the hydrogen-defect system. The individual properties of defects have been extensively covered elsewhere in [2], [26], [27]. This section focuses on vacancies, dislocations, and voids as these are the main types of defects that are produced during prolonged exposure to ion radiation and plasma electrolysis. However,

it is important to keep in mind that this section describes the various hydrogen-defect interactions as independent occurrences. It does not take into account the concurrent far from thermodynamic equilibrium effects from bombarding incident ions and how they, in turn, affect the hydrogen-defect interaction.

The vacancy defect is often considered the simplest point defect and is the most abundant after an ion implantation treatment. It is the absence of a single lattice atom as seen for Pd in Figure 10 where the vacancy is in the center of the diagram.

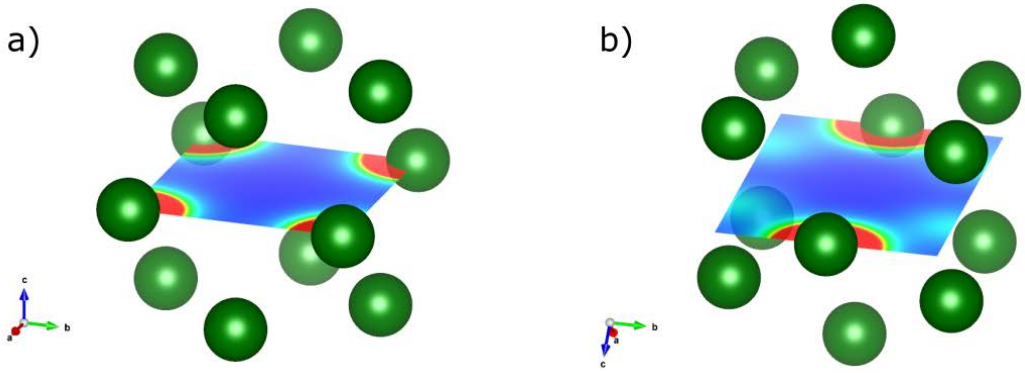

Figure 10. Vacancy in Pd with 12 nearest neighbors. Electron density shown on (a) (001) and (b) (101)

Figure 10 shows the electron density on the (001) and (101) planes, and it is immediately apparent the minimum is located in the center of the vacancy. As previously mentioned about the octahedral bond site, hydrogen is most stable in areas of low electron densities and large volumes. However, this viewpoint can be misleading. While looking at

Figure 10, one would expect the center of the vacancy to be host to the trapped hydrogen, but that is not the case. Ion channeling experiments showed that the hydrogen atom is slightly displaced by ~0.2 Å from the octahedral site [9]. This presents an opportunity to explore a more comprehensive approach that includes kinetic and thermodynamic properties of the system instead of the simple qualitative method of looking at electron densities and geometry.

Besenbacher et al. [24] calculated the energy landscape for an embedded hydrogen atom in Pd using the effective-medium theory. While the approach contained significant approximations, it proved to be a useful, instructive tool for binding enthalpies. The binding enthalpy is defined as the energy difference between a local energy minimum and the energy of H in solution in the crystalline lattice - a purely thermodynamic quantity. The binding enthalpy shows the strength of the trapping albeit not the mechanism of the binding or the activation enthalpy which is from the kinetics perspective representing the required energy for hydrogen to overcome and diffuse from the trap. It was found that the center of the vacancy does indeed contain the lowest electron density. However, it is an unstable energy equilibrium leading to the displacement of the hydrogen atom. The interaction energies for a hydrogen atom in metals were calculated as a sum of various terms

$$\Delta E(\vec{R}) = \Delta E_{hom}^{eff}\left(\bar{n}_0(\vec{R})\right) + \Delta E_c(\vec{R}) + \Delta E_v(\vec{R}) + \Delta E^{hyb}(\vec{R}) \qquad (1.5)$$

Where the dominant term is $\Delta E_{hom}^{eff}\left(\bar{n}_0(\vec{R})\right)$, the hydrogen atom and homogeneous electron gas interaction with $\bar{n}_0(\vec{R})$ being the weighted average of the electron density around the hydrogen atom. The perturbative corrections are the three end terms which respectively represent the inhomogeneity of the real metal lattice, the interaction of hydrogen with the metal core electrons, and the hybridization between the hydrogen H 1s state and the metal d band.

Looking at only the hydrogen atom and electron gas interaction term, $\Delta E_{hom}^{eff}\left(\bar{n}_0(\vec{R})\right)$, gives a qualitative understanding of the energy landscape characteristics. Its calculated form showing dependence on the electron density is shown in Figure 11.

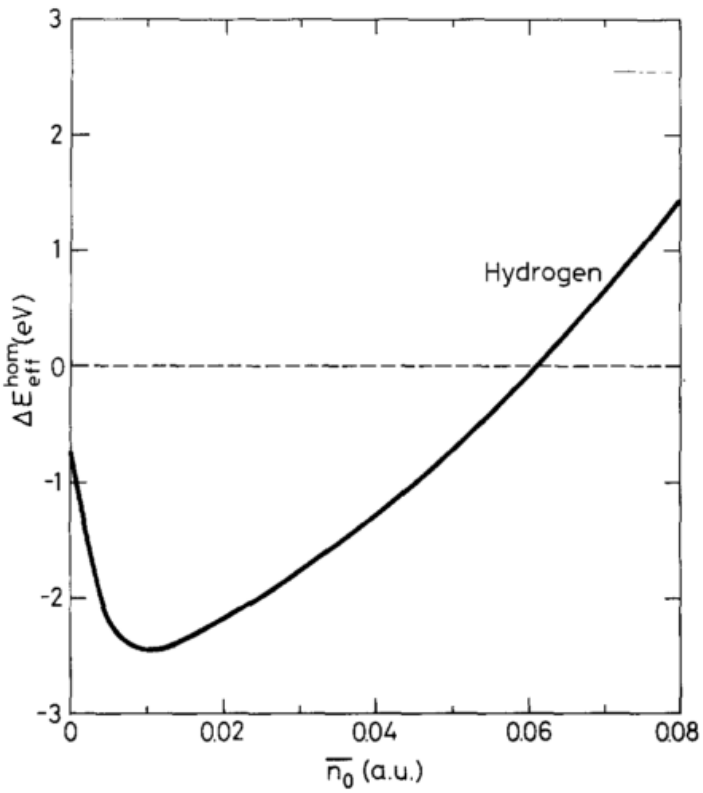

Figure 11. ΔE_{hom}^{eff} as a function of average electron density

This electron density dependent ΔE_{hom}^{eff} function is then used in Figure 12 to show the energy variation as a single hydrogen atom enters a metal lattice and encounters a vacancy. The path of the hydrogen atom is illustrated in Figure 12a, while b) and c) represent the corresponding electron density and interaction energy respectively. Figure 12 is an edited version from [24] that includes numbers for points of interest as the hydrogen traverses the material. The sequence of interaction is as follows

1) Hydrogen atom approaching the surface interacts with an exponentially increasing electron density.
2) Eventually, the optimum electron density is encountered corresponding to a tightly bound chemisorption site.
3) Further into the lattice, the oscillating $\bar{n}$ represents the movement through octahedral sites with minimum electron densities and energies.

4) The hydrogen atom encounters the vacancy and resides on an off-center site due to it being thermodynamically favorable.

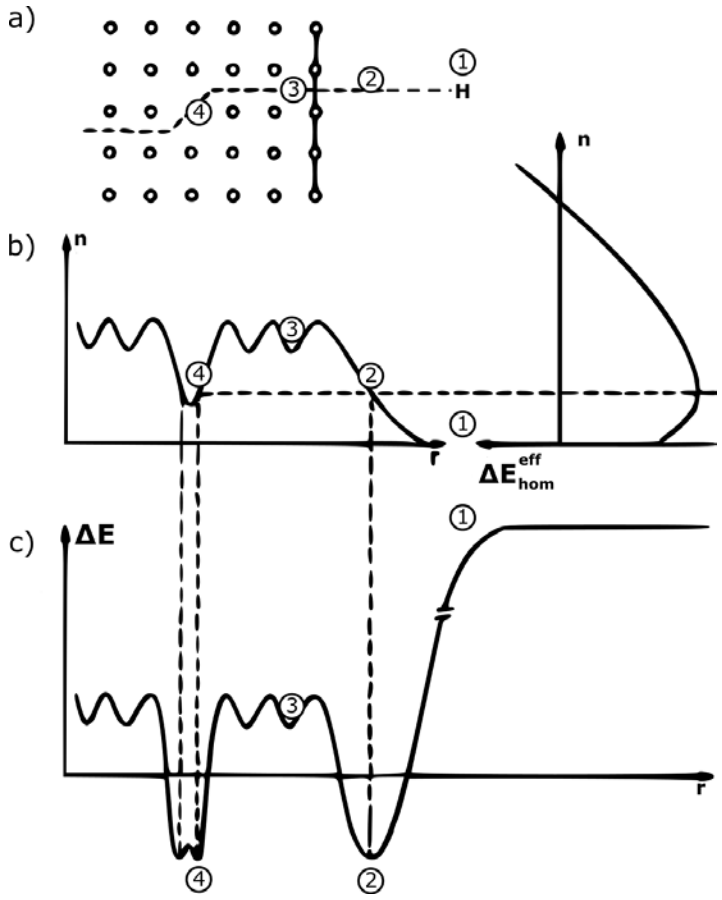

Figure 12. Depiction of the energy variation as a hydrogen atom passes through a metal

From these results, it can be seen that a decrease in electron density leads to an increased binding energy. Therefore, as a defect's volume increases so does the binding (trapping) energy. This results in the trapping energies for defects following: dislocations $\leqslant$ vacancies $\leqslant$ voids, where [24] produced experimental energies of 0.31 eV and 0.23 eV for voids and vacancies respectively. Voids are seen as agglomerations of vacancies to form large volume vacancy complexes. These voids can often behave as internal surfaces and lead to the recombination of hydrogen into its molecular form necessitating a different approach to accurately derive their hydrogen binding energies compared to vacancies [4].

Dislocations are another type of defect where hydrogen often conglomerates. In the FCC palladium lattice, edge dislocations are formed primarily from slips in the [110] direction on the (111) plane. The nature of the dilational strain field about edge dislocations and the fact that hydrogen occupies octahedral sites in the metal leads to strong interactions between the two. This interaction increases the lattice's hydrogen solubility as a Cottrell atmosphere is formed, i.e. interstitial atoms being trapped in and around dislocation cores as shown in Figure 13 [2], [8].

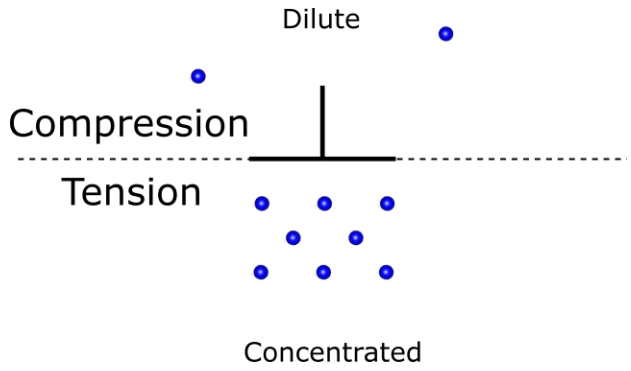

Figure 13. Cottrell atmosphere depiction

Flanagan et al. [25] showed that cold-rolled Pd with large dislocation densities had an increased solubility compared to annealed Pd with a relative ratio between the two reaching 1.8. Their prior studies on hydride formation and decomposition also showed increased hydrogen solubility which was later revealed to be due to the hydrogen segregation to the stress fields around dislocations [8], [23]. They showed no experimental evidence of hydrogen trapped in Pd dislocation cores. Heuser et al. used Small-Angle Neutron Scattering (SANS) also to show that an abundance of dislocations formed from hydrogen cycling (hydride formation and decomposition) and that they were strong traps for interstitial hydrogen [28], [29].

The claim that no hydrogen is trapped in dislocation cores, found in [25], has recently been contradicted by various studies [28], [30]-[33]. The work done in [28], [33] with the SANS measurements showed the deuterium being trapped inside and around the

dislocation core forming long cylindrical hydrides. The local concentration was inversely proportional to the distance from the dislocation core's center. The concentration for the core and surrounding atmosphere was averaged to be 4 to 6 deuterons per Å of dislocation while the bulk material's concentration was PdH_x ($x \sim 10^{-3}$). Binding energies of hydrogen to the dislocation sites were also found. These trapping sites had a binding energy of $\varepsilon_H = 0.2$ eV, while similar SANS studies with lower bulk concentrations of $x \sim 10^{-4}$ had a higher binding of $\varepsilon_H = 0.7$ eV. This study proposed that the lower concentration of hydrogen was tightly bound to deep dislocation cores [31].

1.4 Characteristics of Dense Clusters

While the production of defects and their interactions with hydrogen have been portrayed, it is elucidating on a phenomenological order to investigate the properties of these densely trapped hydrogen sites. The immediate feature that draws attention is the density, and subsequent pressure, of hydrogen inside these trapping locations. The pressure inside a void is relevant as past a certain threshold - ~10s of GPa for metals - the void can suddenly expand anisotropically to allow for more hydrogen absorption and simultaneously creating a dislocation loop [34]. At the nanoscale, typical approximations for solute-solute and solute-solvent interactions breakdown leading to the need for a more complete quantum mechanical method to calculate these internal pressures. These estimates are needed to explain certain emergent peculiarities in material properties with high defect concentrations and trapped hydrogen within.

It was previously noted how defects enhance the solubility of hydrogen for a material with [H]/[Pd] ratios reaching 1.35 after cold-rolling due to increased defect densities [32]. As the super-saturation of the material progresses, the resulting pressure within the defects grows. Common early formulations of the required pressure for void growth and dislocation production were given in [34]:

$$P - \frac{2\gamma}{r} \geq \frac{Gb}{r} \tag{1.6}$$

$$P - \frac{2\gamma}{r} \geq \frac{Gb \log\left(\frac{r}{b}\right)}{2\pi r} \tag{1.7}$$

With P as the pressure, γ the surface tension of the material, r the radius of the void, G the shear modulus of the material, and b the Burgers vector of the resulting dislocation loop. As an example and depending on whether (1.6) or (1.7) is used, the pressure requirement for a 0.3 nm void to expand is 10.4 or 50.2 GPa - both significant pressures.

As loop punching occurs, dislocations are produced and with them come further conditions for calculating the ensuing pressures. Refer to Figure 14 for a 2D visual representation of hydrogen clusters inside dislocation cores. It shows an edge dislocation with an effective diameter on the magnitude of one Burger's vector for the cylindrical hydride. These cylindrical hydrides can be thought of as nanotubes with compressed hydrogen inside. The length of the dislocations can vary, and they can also form closed dislocation loops.

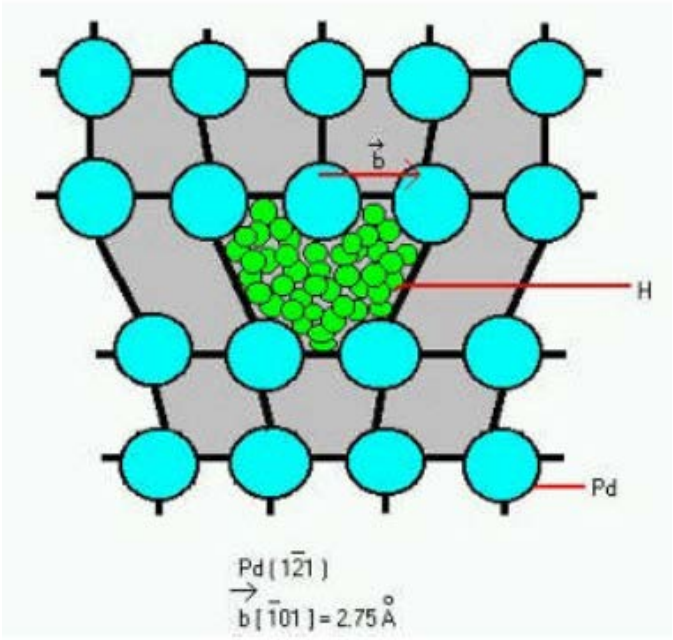

Figure 14. Sketch of high-density hydrogen cluster in a Pd edge dislocation core [35]

It is possible to obtain estimates for the stress fields close to these dislocation cores. These stress fields interact with the strain caused by solute atoms, and this interaction is approximated using linear elasticity theory and continuum mechanics. This interaction is most substantial at edge dislocations due to the hydrostatic stress field. The calculation of the hydrostatic pressure part of the stress field is possible and is done in (1.8) shown below.

$$P = \frac{Gb(1+v)}{3\,\pi(1-v)}\frac{\sin(\theta)}{r} \tag{1.8}$$

Where G is the shear modulus, v Poisson's ratio, b the magnitude of the Burger's vector, and θ and r are cylindrical coordinates. This forms circles of constant hydrostatic stress in relation to an edge dislocation's diameter R. Figure 15 shows this in cylindrical coordinates.

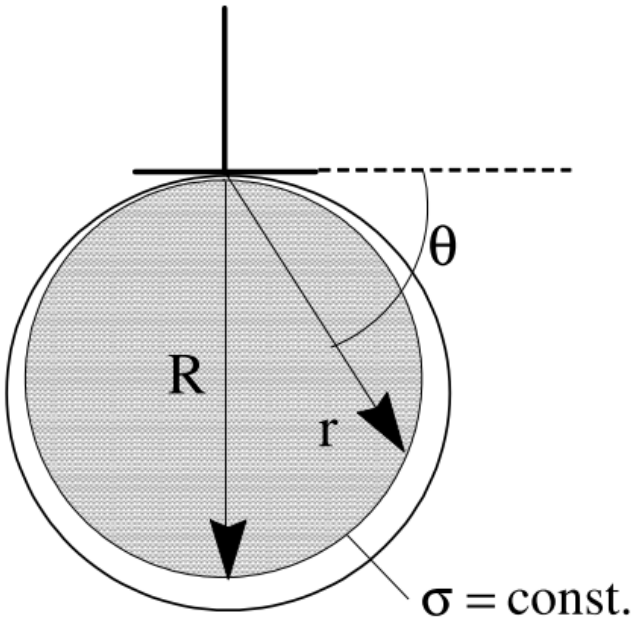

Figure 15. Circles of constant hydrostatic stress at an edge dislocation in cylindrical coordinates [36]

Using (1.8) a graph of the hydrostatic stress relation to the dislocation's diameter can be plotted. Figure 16 shows this where the red boxed area is when the diameter drops below the magnitude of one Burgers vector and this equation is no longer valid. The pressure right before this section is roughly 10 GPa. The boxed section shows how the pressure increases exponentially and approaches infinity as $R \to 0$ which can also be quickly seen from (1.8). As mentioned above, this is where the equation is no longer applicable and is only an indication of the possible magnitude of the pressure found in the dislocation core. This breakdown in the model is from point defects and interstitials dynamically interacting via their own imposed perturbations on the stress field. These many-body interaction effects, exceptionally close and inside of dislocation cores, require atomistic models to fully determine the atmospheres formed [2], [36]. Models have made significant progress recently, but can still produce erroneous atomic mobility results as the actual interaction potentials and correlation functions for the hydrogen clusters are unknown.

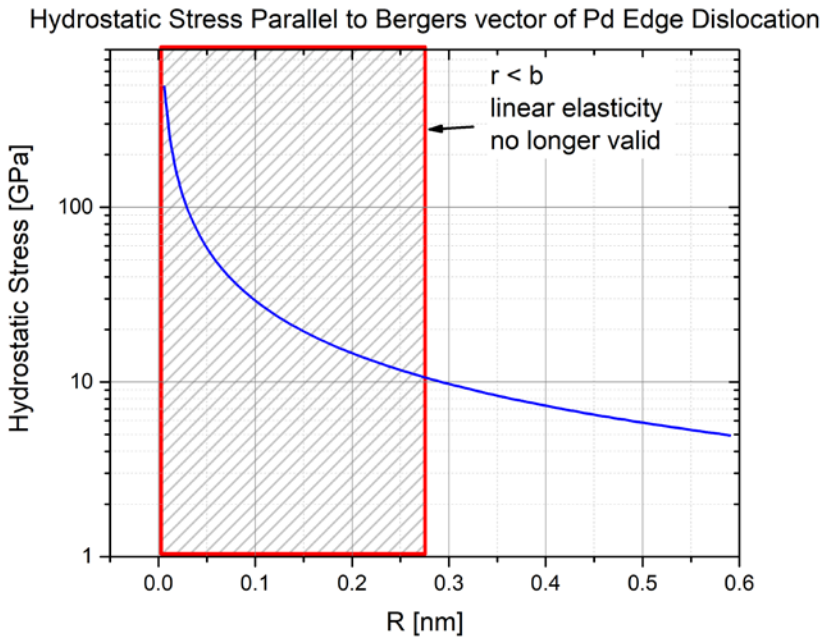

Figure 16. Hydrostatic stress by Pd edge dislocation calculated by using continuum mechanics

These pressures are relevant to the formation of condensed phases of hydrogen. Ashcroft proposed that dense hydrides of the IVa group might be High-Temperature

Superconductors (HTS) under pressures obtainable by diamond anvil cells [37]. He suggested that external pressures imposed on the hydrogen already compressed by the stress field of the lattice would cause the hydrogen to transition to a metallic state. The electrons from the hydrogen and metal lattice would have high band overlap (1.1 Palladium - Hydrogen Properties previously mentioned sd-hybridization) resulting in strong electron-phonon coupling and emergent superconductive properties.

Pure and annealed palladium is an ordinary metal down to 0.1 K, but the hydride system PdH_x ($x > 0.8$) demonstrates superconductivity at higher temperatures. Ion implantation allows one to reach concentrations above $x = 1.0$ and transition temperatures for PdH and PdD were found to be 8.8 K and 10.7 K respectively [38]. An initial speculation for this increase in transition temperature was the formation of metallic-like hydrogen in the metal lattice. However, [38] disproved this and showed the strong coupling of the optical phonons to the electronic system was the cause of the high transition temperatures.

Since the edge dislocations have favorable conditions for condensed phases of hydrogen to form with strong electron-phonon coupling, they should exhibit a superconductivity transition above that of the bulk PdH_x's transition temperature. If the condensed phase of hydrogen was semi-metallic, diamagnetic properties would also be expected at low temperatures. These properties were investigated in [32] for a hydrogen cycled single crystalline palladium sample (hydride formation and decomposition) that had a loading ratio PdH_x ($x \sim 4.0 \times 10^{-4}$). TDS was used to show that only hydrogen trapped in deep dislocation cores with activation energies of 1.6 eV remained after treatment. Magnetic measurements using a 1 Tesla SQUID showed a diamagnetic contribution to the PdH_x system at $T < 30$ K and a superconductivity transition temperature $T_c = 18$K. This transition temperature is significantly higher than those reported for bulk palladium

hydrides with x ~ 1.0, and an effective loading ratio in the dislocation cores was found as $x_{eff} = 1.35$ [32].

There is another method in which local concentrations can have loading ratios of x $\geqslant$ 1.0. It relates to the dynamics of the palladium-hydrogen system and the inherent mobility of dislocations. Dislocations are mobile inside a lattice and can combine with one another or annihilate at grain boundaries. Their movement is affected by their surrounding Cottrell atmospheres which have an active drag force [2]. High local concentrations can occur under two circumstances: the dislocation breaks free of the Cottrell atmosphere leaving it behind or by the combination of two dislocations and surrounding Cottrell atmospheres [39]. As these are transient effects on sub-nanometer scales, directly studying them has not been possible.

These findings all indicate that high-density hydrogen clusters can form inside palladium dislocations and voids. This corresponds to localized regions that have not been previously directly studied. The static parameters around the defects can be approximated with elasticity theories, but the dynamics of the hydrogen-filled voids, dislocations with hydrogen deep inside the core, and surrounding hydrogen atmospheres are significantly more intricate.

1.5 Thermal Desorption Spectroscopy

Thermal Desorption Spectroscopy is a prevalent method for investigating binding energies and concentrations of adsorbed and absorbed species. It consists of heating a sample at a constant temperature rate while under vacuum and monitoring the partial pressures of desired species with mass spectroscopy equipment. In order to obtain quantitative values for a given species, the system must be calibrated with standards of known concentrations and binding energies to take into account pumping or heating inefficiencies in the system. Other problems do arise while studying complex materials with multiple binding locations

that can interact with desorbing species. Hence methods are taken to deconvolve individual binding sites.

Two methods can be used to analyze TDS spectra: computation modeling of the binding mechanisms and experimentally obtaining trends for partial pressure peaks' temperature dependence on ramp rate. Experiments have previously shown that the cycling of palladium-hydride through its α and β phases produces large defect concentrations, primarily dislocations. When palladium nanoparticles are used, the formed dislocations are within grains on the order of 10s of nm which provides little volume for dislocations to be mobile and effectively pins them. This produced high binding-energy sites for hydrogen in [40], and one of their TDS spectra is shown below. It has a desorption peak centered at 825°C and a corresponding activation energy for diffusion of 1.6 ± 0.2 eV.

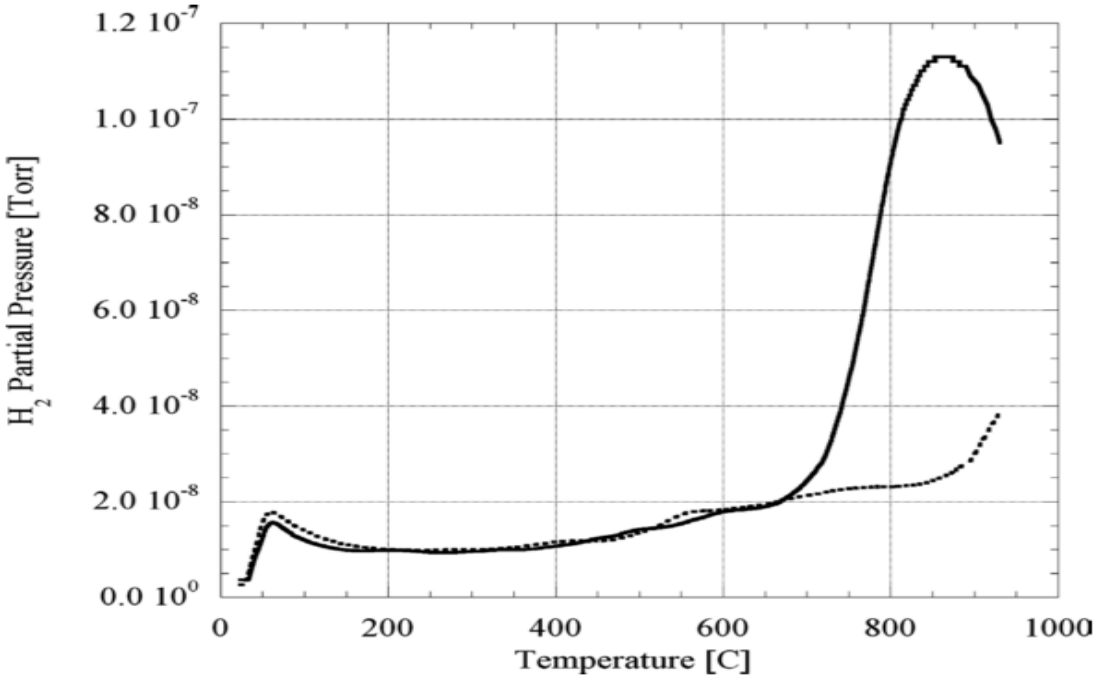

Figure 17. Thermal desorption spectra of single crystal Pd with (solid line) and without (dotted line) hydrogen

1.6 Thesis Overview

This thesis aimed to investigate the role of deuterium ion bombardment on the microstructural evolution of palladium resulting in the retention of deuterium at high binding energy sites. Utilizing a DC glow discharge it was hypothesized that varying plasma parameters and ion fluences would produce different types of defects within the cathode material with corresponding interstitial binding energies. Figure 18 shows a schematic of the proposed effects on the cathode - deuterium ions gain energy as they traverse the potential drop in the plasma sheath and bombard the cathode depositing their energy. Initially, the cathode contains a dilute concentration of deuterium, and a α-PdD_x phase is formed as shown in a). Due to palladium's solubility for hydrogen and the hydrogen's low diffusivity, this concentration increases with fluence to create a scenario similar to that found in b). Here hydrogen coalesces into the higher concentration β-PdD_x phase which puts strain on the surrounding lattice aiding in the defect production from ion damage cascades. Voids, vacancies, and dislocations are then able to act as trapping sites for the interstitial hydrogen.

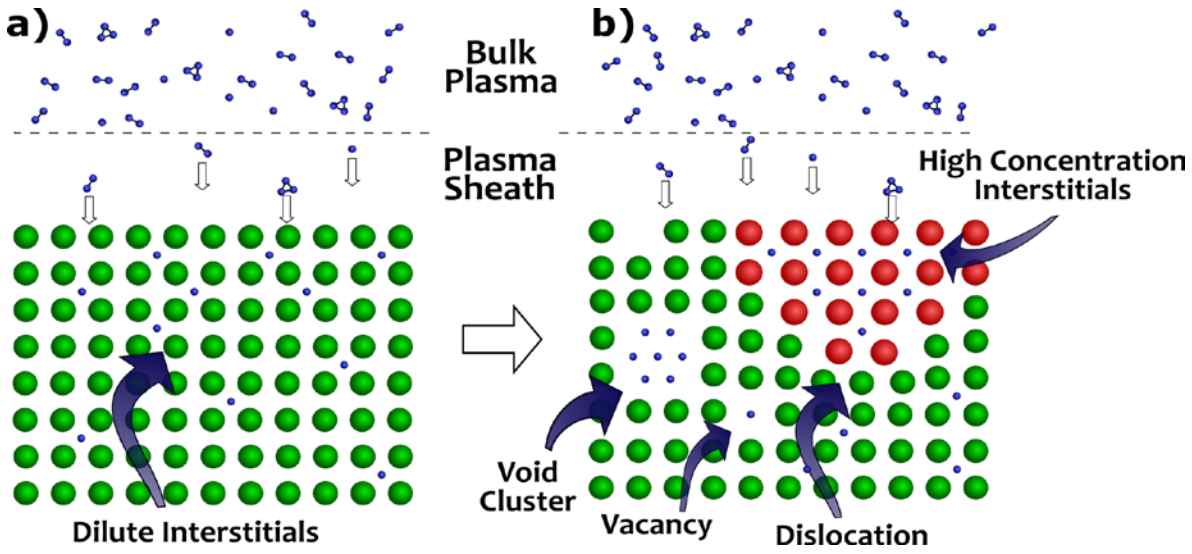

Figure 18. Plasma ion implantation and defect formation. (a) interstitial deuterium forms a dilute phase metal-hydride, e.g. α-PdD_x with x < ~0.025 (b) high concentration phase formed, e.g. β-PdD_x with x > ~0.6, and deuterium trapped at defects, e.g. voids to form clusters, vacancies, and dislocations.

A primary plasma characteristic that is related to the cathode's microstructural evolution is the collisionality of the plasma. If the plasma operates in a collisionless regime, due to the large mean free path the incident ions can gain a significant portion of the potential energy drop in the plasma sheath as kinetic energy. They would then have an energy distribution centered around that value. However, if the plasma is in a collisional regime, the incident ions will have a more Maxwellian distribution with lower most-probable energies and long energy tails extending to the maximum kinetic energy gain through the sheath. This also relates to the cathode's surface temperature as the ion density and average energy are connected to the energy flux at the cathode. It is the magnitude of this energy flux that determines how much power is deposited, and hence the temperature of the cathode. The cathode's temperature then affects diffusion constants for interstitials resulting in different solute-solute, solute-solvent, and solute-defect dynamics.

Another plasma parameter that affects the cathode's microstructure is the cathode's bias. As the bias increases, the maximum kinetic energy of incident ions also increases allowing for deeper penetration into the material and a more extensive damage cascade. In Figure 19 the ion's penetrating trajectories are represented from SRIM to emphasize subsurface damage production. As their energy increases, the ion concentration moves further into the cathode. The figure also shows the resulting surface structure from sputtering - taken from a plasma treated sample using AFM.

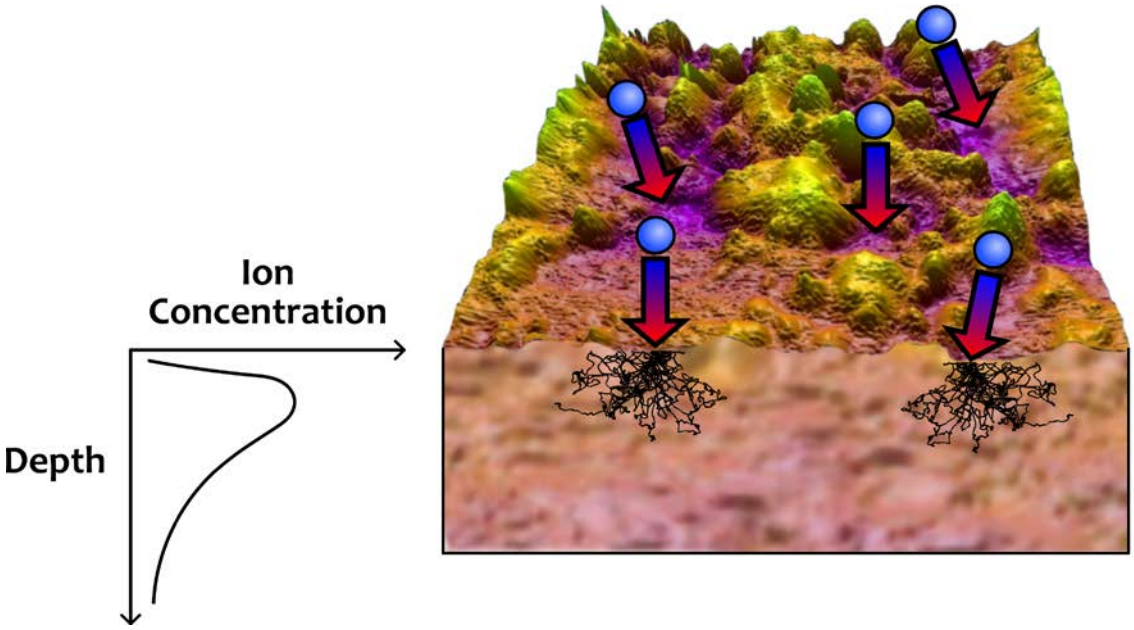

Figure 19. Diagram showing incident ions gaining energy and causing surface morphology changes.

Keeping these critical factors in mind - the collisionality of the plasma and cathode bias - it was intended to produce a relationship between ion energies and fluence to optimize the production of high-density deuterium clusters with high binding energies. For the current results, the ion bombardment was done in the collisional regime to allow fluxes high enough for the desired fluences to be reached in a reasonable timeframe. Figure 20 shows the plasma treatment scheme; it consisted of operating the plasma at two different pressures at three different cathode voltages for three different fluences. Unfortunately, due to difficulties with the TDS apparatus data was not obtained for -0.875 kV and -1.0 kV at 1.0 Torr, nor was a third pressure chosen to get a full pressure relationship. These are considered future work.

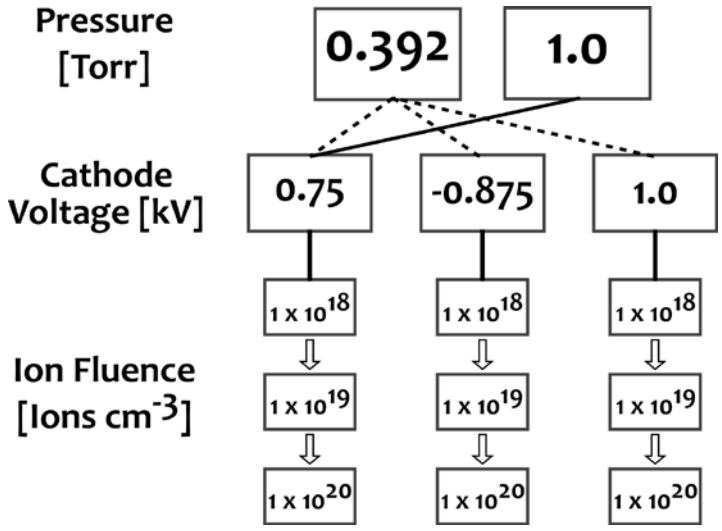

Figure 20. Plasma treatment scheme for the production of defects and high binding energy sites

The thesis begins with a complementary experimental and computational study to gain estimates of incident ion energies. Chapter 2 focuses on Langmuir probe measurements to obtain EEDFs using the Druyvesteyn method. Chapter 3 then simulates the DC discharge plasma and produces EEDFs which are compared to the Langmuir probe results. The experimental and computational model's results are then compared. Subsequently, the model is used to estimate incident ion energies within COMSOL's particle tracing module. An investigation of the surface and subsurface microstructures of some of the cathodes post-bombardment is presented in Chapter 4 encompassing the surface morphology progression. Chapter 5 presents the TDS findings for various fluences and cathode biases. Finally, the thesis concludes with attempted explanations of the TDS data along with a discussion of future work.

Chapter 2: Characterizing Plasma Properties

2.1 Background

Langmuir probe diagnostics are exceedingly common for determining fundamental plasma properties such as the electron temperature and density. They are simple to construct and require little materials making them a cheap and quick tool for gaining a basic understanding of a plasma's environment - plasma potentials and floating potentials. Their operation can be fitted for various types of plasma sources from simple approaches like the DC discharge used in this thesis to more complex sources like RF, magnetron, and microwave plasmas. Given their simplicity, the analysis of Langmuir probe data can be misconstrued as straightforward presenting little difficulties. Often this leads to using incorrect procedures of analysis or implementing probes that influence the plasma to a significant extent [41]. However, given precautions they can be used to obtain the spatial dependence of EEDFs despite the inherently noisy nature of plasmas. These are important to understanding reaction rates as they contain information on elastic and inelastic processes that affect transport kinetics. Ensuring a model has corresponding EEDFs that follow experimental trends helps affirm the accuracy of the model as is the intention here.

An initial step for preparing to use a Langmuir probe is taking into account various characteristic length scales of the system - be it of the probe, the electrons, the neutral particles, etc. It is of utmost importance to limit the probe size as to avoid plasma and sheath perturbations leading to erroneous, and often useless, data [41]. Table 2 lists the length scales and their symbols used.

Table 2. Important characteristic length scales while using Langmuir probes

Characteristic Length Scales	Symbol
Probe-tip radius	r_p
Probe-tip length	l
Probe-holder radius	b
Electron Debye radius	λ_D
Electron mean free path	λ_{mfp}

These scales are taken into effect and determine the regime of the plasma - its collisionality and relative sheath thickness. The plasma sheath is a result of the plasma insulating itself from the electric potential perturbation of an imposed metallic object, be it at the ground or floating potential. This is known as Debye shielding where the Debye length is the scale at which a potential gradient can exist in a plasma and hence determines the sheath thickness. The Debye length is dependent on the electron temperature and density as shown below

$$\lambda_D = \sqrt{\frac{\epsilon_0 T_e}{n_e e^2}} \tag{2.1}$$

The plasma sheath derivation is not shown here, and the reader is directed towards other references [42], but suffice to say the sheath forms as a balance of ion and electron fluxes at the surface and can be considered as a space-charge boundary layer. Without a magnetic field to take into account the ratio r_p/λ_D is what determines the sheath thickness regime. When $r_p/\lambda_D \gg 1$ the sheath is considered thin, when $r_p/\lambda_D \geq 1$ it is in a transition regime, and when $r_p/\lambda_D < 1$ the sheath is thick. Collisionality is taken into account through the electron's mean free path: $\lambda_D \ll \lambda_{mfp}$ is known as collisionless and often times

the requirements of $r_p, b < \lambda_{mfp}$ are included [43]. The table below condenses these relations.

Table 3. Characteristic length scale conditions and corresponding regime

Conditions	Regime
$\lambda_D \ll r_p < \lambda_{mfp}$	*collisionless thin sheath*
$r_p < \lambda_D < \lambda_{mfp}$	*collisionless thick sheath*
$\lambda_{mfp} < \lambda_D \ll r_p$	*collisional thin sheath*
$\lambda_{mfp} < r_p < \lambda_D$	*collisional thick sheath*
$r_p < \lambda_{mfp} < \lambda_D$	*transitional thick sheath*

There are various methods used to analyze Langmuir probe characteristic curves for each specific region. The theories for the collisionless regimes are the most common techniques and usually confine experiment parameters to withhold these conditions. The classic Langmuir probe procedure where the electron density and temperature are inferred from the electron portion of the I-V characteristic was compared to the Druyvesteyn formulation along with other methods by Godyak and Alexandrovich in [43]. They concluded that the EEDF measurement using the Druyvesteyn method was the single reliable probe diagnostic for non-equilibrium collisionless plasmas. The classic Langmuir probe is fraught with inaccuracies due to the assumption of Maxwellian EEDFs - Lieberman and Lichtenberg note the distributions tend to be non-Maxwellian in the positive column [42] - and the arbitrariness of the ion current approximation. As such, the work herein uses the Druyvesteyn method, and the procedure is outlined.

2.2 Druyvesteyn Method

Electrons within a plasma can be described based on a canonical distribution of the particle's time-dependent spatial and velocity vectors - $f(t, \vec{r}, \vec{v})$ where $\vec{r}$ is the space-coordinate vector and $\vec{v}$ is the velocity vector. The electron-distribution gives the number

of electrons within a given volume having velocities within a given range. This function is used to kinetically describe the plasma electron reactions from electron induced excitations to electron transport. Similar to this formulation is finding the electron energy distribution function which allows obtaining values of electrons within a given energy window - $f(t,\vec{r},\epsilon)$, where ϵ is the electron kinetic energy typically in eV. With this distribution, the electron density and temperature can be easily calculated:

$$n_e = \int_0^\infty f(t,\vec{r},\epsilon)\, d\epsilon \tag{2.2}$$

$$T_e = \frac{2}{3}\langle\epsilon\rangle = \frac{2}{3}\int_0^\infty \epsilon f(t,\vec{r},\epsilon)\, d\epsilon \tag{2.3}$$

The distribution functions can be analytically solved by using the Boltzmann transport equation assuming no magnetic fields:

$$\frac{df(\epsilon)}{dt} + \vec{v}\cdot\nabla_x f(\epsilon) + \frac{q\vec{E}}{m_e}\cdot\nabla_v f(\epsilon) = \left(\frac{df(\epsilon)}{dt}\right)_{collisions} \tag{2.4}$$

However, solving this equation is extremely computationally intensive due to (2.4) describing the evolution of the distribution in a six-dimensional phase space - configuration space and velocity space both in three dimensions. Typically, approximations are made to expand the distribution in spherical harmonics, and the reader can find these in [42]. For isotropic electrons in thermodynamic equilibrium (2.4) is solved assuming a constant collision frequency and the resulting distribution is known as Maxwellian, given below in its normalized form

$$f_M(\epsilon) = \frac{2}{(kT_e)^{\frac{3}{2}}}\sqrt{\frac{\epsilon}{\pi}}\exp\left(-\frac{\epsilon}{kT_e}\right) \tag{2.5}$$

The Maxwellian distribution along with its inherent assumptions on collision frequency and isotropic thermal equilibrium for the electrons is what is used for classic Langmuir probe theories. However, as previously noted this distribution does not always accurately describe the kinetics. An alternative given here is the Druyvesteyn distribution - derived explicitly by Druyvesteyn for non-equilibrium discharges with energy dominant electrons with constant interaction cross sections, low ionization fractions, and elastic collisions being the dominant energy loss mechanism [44]. Lieberman and Lichtenberg go through the derivation of the distribution resulting in

$$f_D(\epsilon) = \frac{0.5648}{(kT_e)^{\frac{3}{2}}}\sqrt{\epsilon}\exp\left(-0.243\left(\frac{\epsilon}{kT_e}\right)^2\right) \tag{2.6}$$

Physically this Druyvesteyn distribution results in a shift of the most probable energies to higher energy along with a decrease in the high energy tail. A comparison between Maxwellian and Druyvesteyn EEDFs at different electron temperatures is shown in Figure 21.

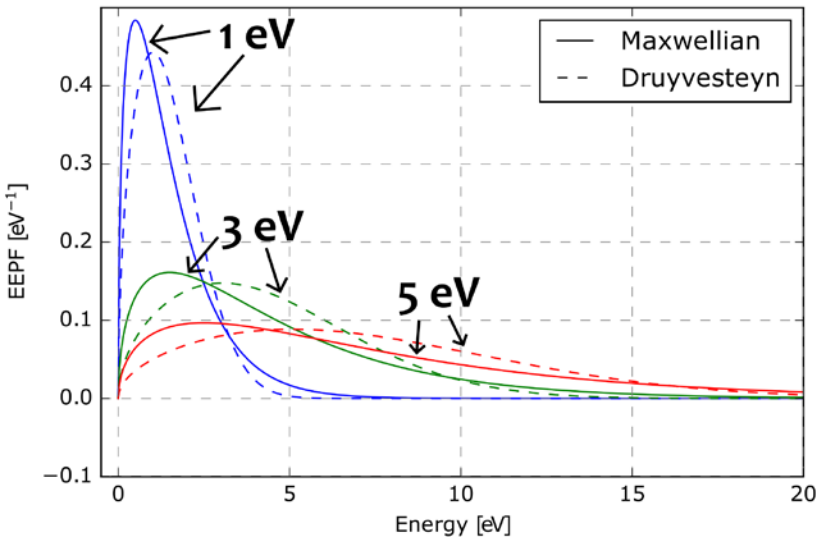

Figure 21. Maxwellian and Druyvesteyn EEDFs for 1, 3, and 5 eV electron temperatures

If plotted on a logarithmic scale and divided by $\sqrt{\epsilon}$, Maxwellian distributions can be easily identified - this format is known as the Electron Energy Probability Function (EEPF). Maxwellian distributions appear linear in this formulation due to the linear dependence of electron temperature in the exponent in (2.5). Figure 22 displays this characteristic compared to the nonlinear Druyvesteyn EEPF.

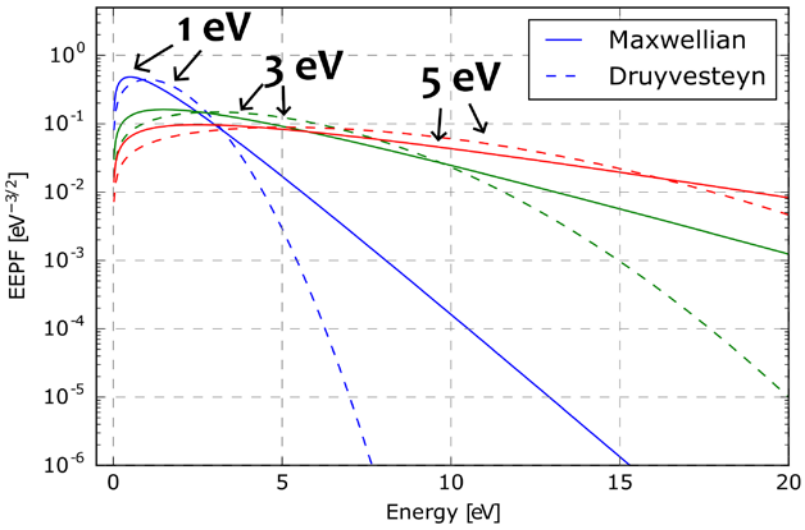

Figure 22. Maxwellian and Druyvesteyn EEDFs on a log scale for 1, 3, and 5 eV electron temperatures

In order to obtain the experimental EEDFs Godyak and Alexandrovich [43] provide a detailed explanation of the Druyvesteyn method which shares its name with the distribution, but analysis of the data is irrespective of distribution type. Similar to the classical Langmuir probe analysis techniques, the procedure begins with obtaining I-V characteristic curves from a metallic probe placed within the plasma where the current collected is due to a potential bias on the probe. Druyvesteyn [44] showed that the EEDFs are proportional to the second derivative of these I-V curves. The actual derivation of the resulting second derivative dependence can be found in [42], but (2.7) shows its final form

$$f(\epsilon) = \frac{4}{e^2 A_p}\sqrt{\frac{m_e V}{2e}}\frac{d^2 I}{dV^2}\ , V = \phi_p - V_p \tag{2.7}$$

Where A_p is the probe's surface area, m_e is the electron mass, e is the elementary charge, and V is the potential difference between the plasma and the probe with ϕ_p as the plasma potential and V_p as the probe applied bias. (2.7) is relegated to low gas pressures where the plasma is in the collisionless regime. It has been expanded for high-pressure applications, but in its current form, it does not adequately take into effect electron collisions with other particles (neutrals, ions, other electrons) in the plasma sheath [41].

Besides considering the pressure and collisionality of the plasma, another characteristic length is often overlooked: the size of the probe. It has been stated that the probe needs to be small enough to avoid perturbing the plasma and its parameters, but what is often forgotten is including the effects from the probe's holder. Godyak and Demidov [41] provide relations that determine whether the probe and probe holders dimensions satisfy the small-probe assumption:

$$r_p \ln\left(\frac{\pi l}{4r_p}\right), b \ll \lambda_{mfp} \tag{2.8}$$

Often for this relationship to be accurate, a telescopic probe design is employed which allows for a thin probe tip and holder while still being sturdy enough to extend far into chambers. An example taken from [41] is shown below

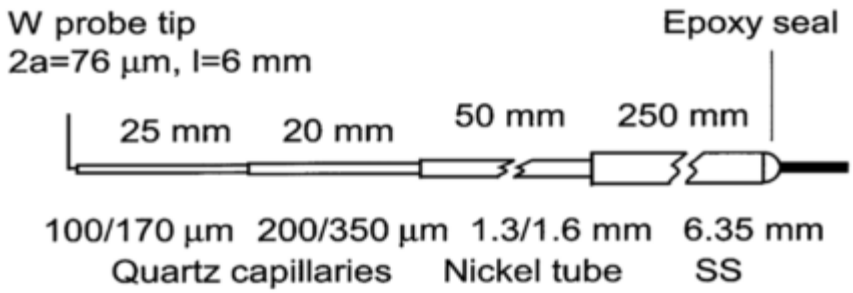

Figure 23. Telescopic probe design

A variety of groups have used the method. Magnus and Gudmundsson [45] used it in their HiPIMS apparatus, Popov et al. [46] in their microwave discharge, and others have used it in ICPs and CCPs with satisfactory results [47]. An important topic that appears is the influence of noise on the probe signal and it augmenting the resulting EEDFs. Any fluctuation that arrises on an I-V curve will be drastically amplified through taking the second derivative. Methods to suppress the noise can be from using hardware, e.g. using a differentiation amplified circuit, or using numerical methods for post-processing the data. The smoothing methods employed can distort the EEDFs significantly, but the benefit of using software is that the original data will still be present for comparison - any missing features can be qualitatively assessed.

2.2.1 Savitzky-Golay Method

Since smoothing techniques present the possibility of obscuring features, their implementation must be done with fidelity. This can be difficult as there are numerous methods for numerical smoothing of data sets each with their caveats - Hayden method with a Gaussian filter, polynomial fitting, Blackman window, general sine-cosine windows, etc. In [45] Magnus and Gudmundsson did a systematic comparison of various approaches for smoothing I-V data for EEDFs. They concluded that the Blackman window provided the best fitting and resulting EEDFs with the Savitzky-Golay method behind by a narrow margin. Despite the Blackman window producing the cleanest and full-featured EEDFs, the Savitzky-Golay method seems to be the most widely used.

The central aspect of the Savitzky-Golay method is applying a polynomial fit to a few consecutive data points with polynomial degree 2 or higher opposed to having a moving average. For a given window of size $n = n_L + n_R + 1$ centered at x_i covering points from $-n_L$ to $+n_R$, the polynomial fit $p_i(x)$ of degree M at value x_i is chosen as the fitted value for that window. This is then applied to each subsequent point in the data set. The polynomial using a least squares method is written as

$$p_i(x) = \sum_{k=0}^{M} b_k \left(\frac{x - x_i}{\Delta x}\right)^k \tag{2.9}$$

This method was initially intended for points of uniform spacing; however current implementations can account for non-uniform data. An added benefit of Savitzky-Golay filters is the ease of determining derivatives, and more information can be found in [48]

The method has two parameters: n - the window size - and M - the polynomial degree. It can be difficult to properly optimize these values and typically fine-tuning is needed based on visually determining whether features are lost. A wider window allows for more smoothing but loses high-frequency features, while an increasing M accounts for higher frequency modulations but loses low-frequency features. As an example, Magnus and Gudmundsson [45] varied these parameters for a dataset of ~1000 points with $n = 81, 101, 151, 191, 251$ and $M = 2, 4, 6$ while logging the correlation coefficient R. Expectedly they found that for smaller windows a lower polynomial degree was needed and vice-versa for increasing windows with an optimal R value of 0.9993 for $n = 191$ and $M = 6$. This window corresponds to roughly 18% of the dataset. In the analysis presented here, it was attempted to follow this relative window size to dataset ratio.

2.3 Experimental Setup

2.3.1 Vacuum System

The experiments were all performed within a vacuum chamber that was capable of reaching 10^{-8} Torr. The active chamber is an 8-inch diameter cross, and Figure 24 shows the system schematic. The system is equipped with a Residual Gas Analyzer (RGA) to ensure adsorbed species desorb entirely during bake-outs.

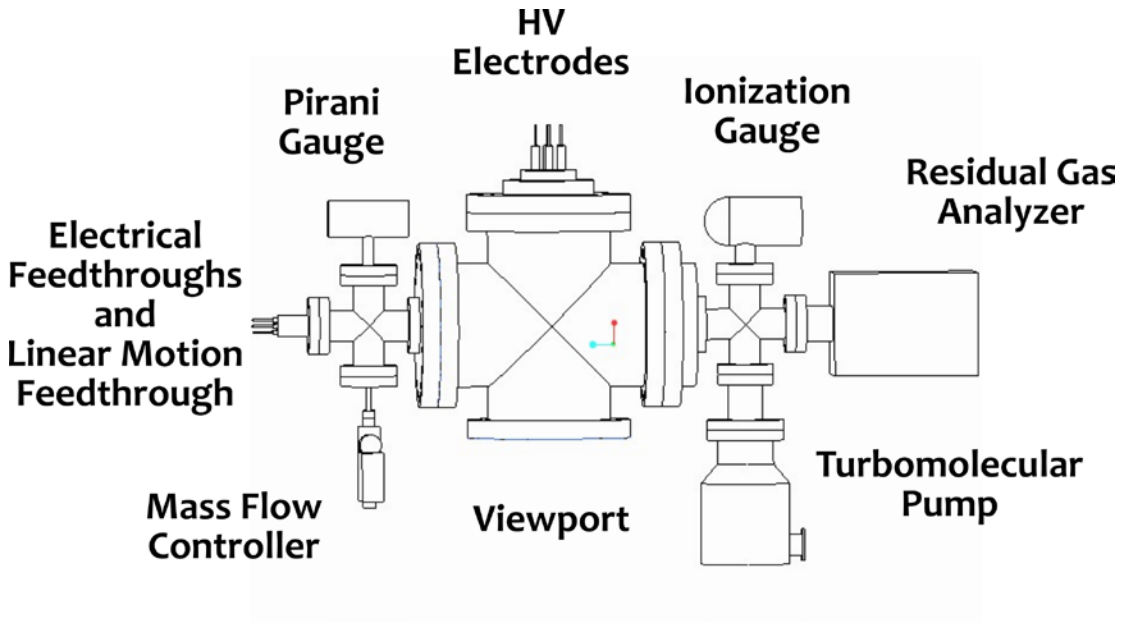

Figure 24. Schematic of vacuum system

The system was outfitted with argon, helium, and deuterium gas inlets which were controlled by a mass-flow controller that had integrated calibrations for each. A high-voltage electrode connected to samples intended for ion bombardment and was driven by a Glassman High Voltage EK series 600W DC power supply that was outfitted with a USB module for data acquisition. The power supply was provided with a LabVIEW program for logging power data. This was modified to also produce a log of voltage and current along with a continuously updated value of the ion fluence on the samples. This assumes the plasma is localized on the cathode which was visually verified as seen in Figure 25 with an early iteration Langmuir probe. The LabVIEW interface is shown in Figure 26. The inset zooms in on the section that takes a user input of the total area being treated and continuously updates the cumulative fluence based on the current data.

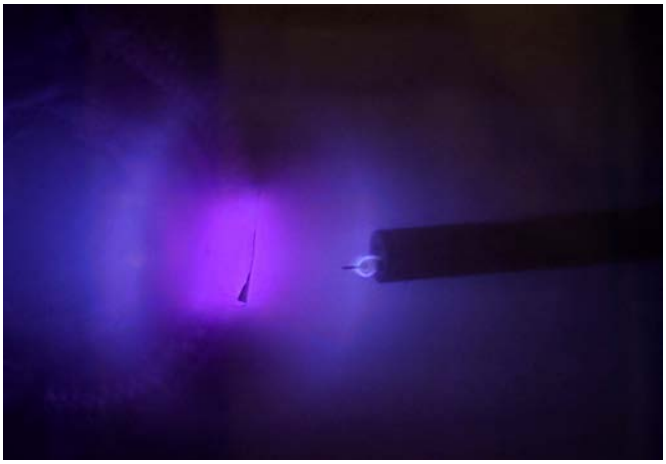

Figure 25. Plasma localized on cathode sample

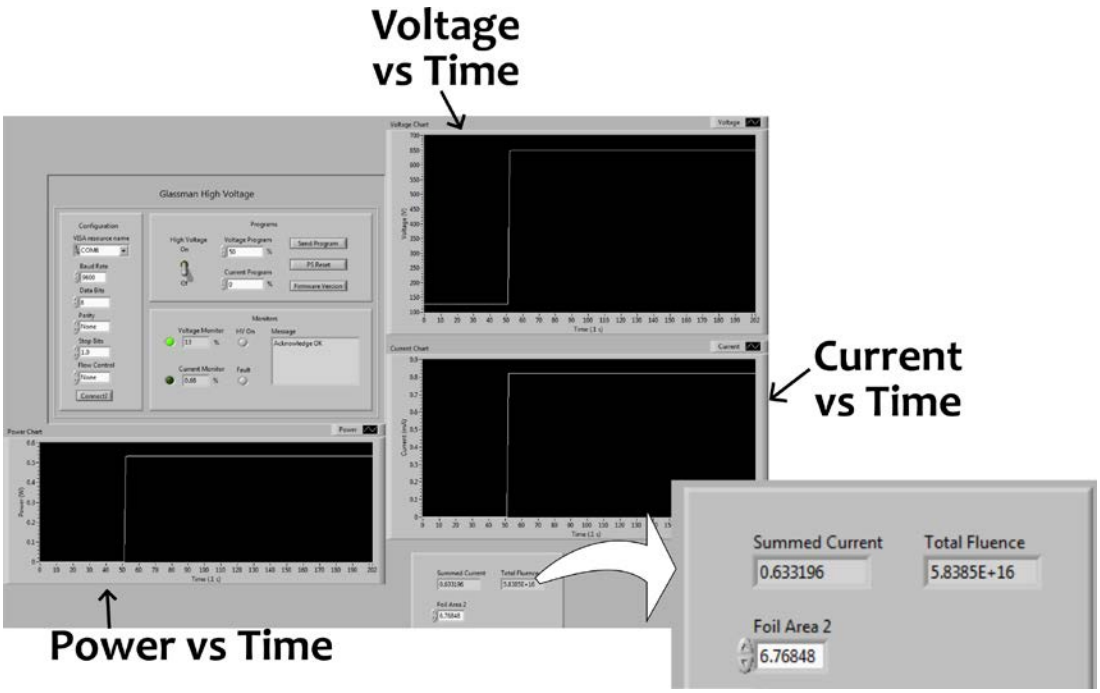

Figure 26. Labview program with inset displaying the cumulative fluence

The sample holder was custom made to integrate a resistive heating coil in direct contact with multiple samples. Difficulties were found in implementing a heating coil that was able to withstand high vacuum without fracturing with large temperature cycles. Tantalum wire was eventually used due to its low vapor pressure. The Ta wire was wrapped around an alumina cylindrical shell and the high voltage feedthrough that would connect to samples, covered with a MgO paste, cured with a heat gun, and then

subsequently wrapped again for another layer. A K-type thermocouple was also implemented beneath the heating coil's MgO layer. Figure 27 shows the heated sample holder without the inclusion of the high voltage feedthrough and its set lugs that would connect up to three samples if desired. The heating coil could achieve $450℃$ while under vacuum without issue.

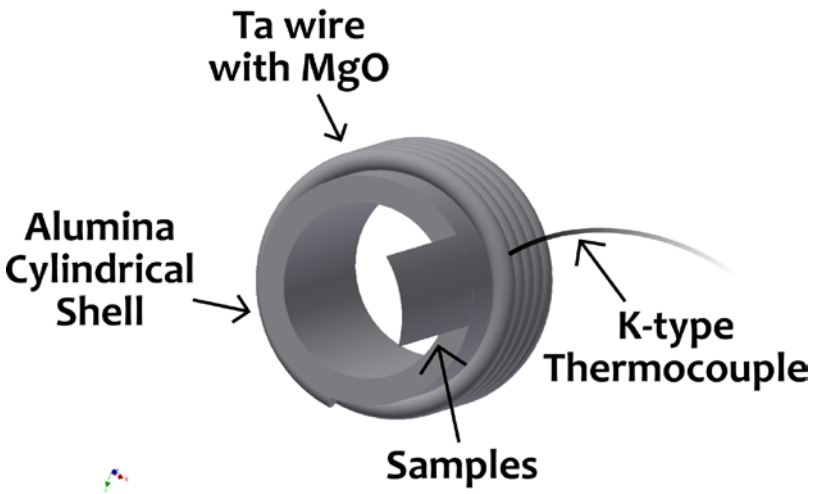

Figure 27. Diagram of heated sample holder

The RGA in tandem with the heated sample holder was used for in-situ TDS. The heating apparatus inside of the plasma chamber has a maximum temperature of $500 - 600℃$, and so the TDS in the system is limited to adsorbed species with weak binding energies. To produce figures similar to those obtained previously with higher maximum temperatures, such as below, a separate heating furnace unit was used. This means the sample is removed from the chamber and implemented into the other system which exposes it to possible contaminants. However, these are primarily H_2O and CO_2 and do not inhibit the desorption process of hydrogen as they desorb at lower temperatures than the binding sites of interest. The in-situ TDS will also be used to ensure H_2O and CO_2 are desorbed from the surface of the foils and to check if any of the excess heat being measured

correlates to water production. H_2O and CO_2 adsorbed on the surface of materials inhibit the absorption of hydrogen as they block adsorption sites [49]-[51].

2.3.2 Langmuir Probe

The Langmuir probe was made of a 0.1 mm (0.004 in.) diameter Tungsten wire. 2.2 mm (0.087 in.) in length, surrounded by a thin alumina sheath with a 1.6 mm (0.063 in.) outer diameter which extends from a 9.5 mm (0.374 in.) outer diameter alumina sheath. The end of the probe was sealed with TorrSeal to the thin alumina sheath to provide added insulation. Figure 28 is a model of the Langmuir probe as it approaches the cathode sample.

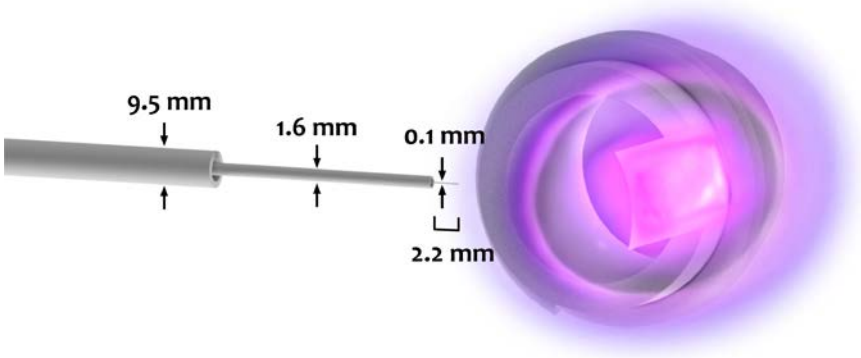

Figure 28. Diagram of Langmuir probe

Figure 29 shows a schematic of the apparatus depicting the discharge breakdown gap distance, probe's direction of motion, and the probe to cathode distance. The discharge gap distance was measured between the cathode and the chamber wall parallel to it within the large four-way cross-chamber seen in Figure 24. Depending on the gas type and cathode bias, the sample holder could be repositioned for a different discharge gap distance. For the tests being reported, the distance was held at 6.5 cm. The probe was initially set into contact with the cathode roughly 1 cm from the foil-heater interface and as the probe was withdrawn the position along the linear motion feedthrough was recorded

with digital calipers to a precision of ± 0.005 mm. It was essential to keep the Langmuir probe out of the plasma sheath as the potential bias on the probe in addition to the potential drop within the sheath created discharges around the probe tip which obfuscate the plasma parameters formed by the cathode. Another consideration to take into account was sputtered material from the cathode coating the Langmuir probe and substantially increasing the probe's area. This was combatted after large treatment fluences by biasing the probe itself with high voltage ~ −1 kV in argon and sputtering the thin layer.

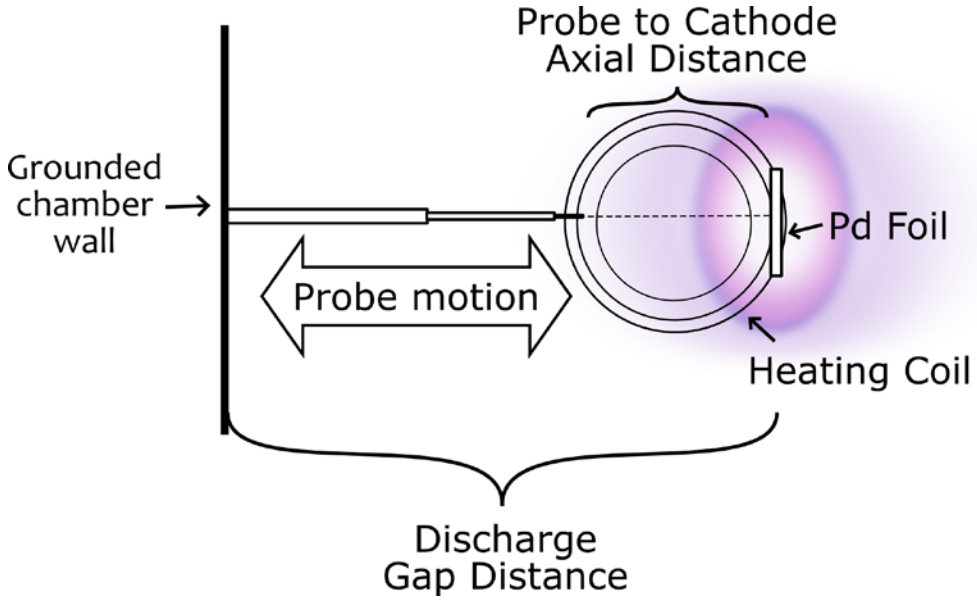

Figure 29. Schematic of Langmuir probe showing probe motion direction, discharge gap distance, and distance between the probe and cathode

The circuit powering the Langmuir probe consists of an Agilent 33220A Waveform Generator connected to a Kepco Bipolar Operational Power Supply/Amplifier Model BOP 1000M with a Tektronix TDS 3012B oscilloscope acquiring the probe's I-V curve. This is shown in Figure 30.

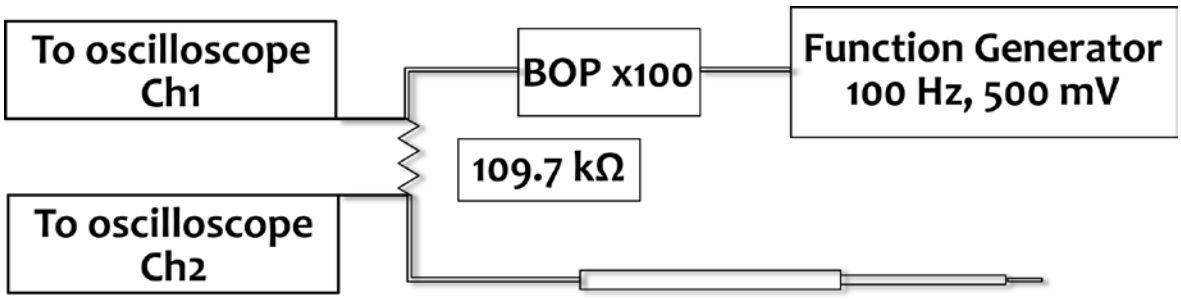

Figure 30. Langmuir probe circuit

The function applied to the probe was a 100 Hz sawtooth wave with an amplitude of 500mV. A fast probe scan rate is desirable to keep the probe in thermal equilibrium and to prevent it from melting in high electron density environments.

2.4 Experimental Results

2.4.1 Langmuir Probe Analysis

It was found that using an averaging of two sweeps on the oscilloscope of the I-V curve was the quickest way to obtain multiple measurements with relatively little noise. A fast scan setting was also used on the oscilloscope reducing the data points per sweep from 10,000 to 500, but this typically was reduced even further to 200-300 as duplicate values were removed. Once the probe data was acquired, it was sent through a python script that implements the Druyvesteyn method using Savitzky-Golay filters.

The code has multiple steps and outputs, as such an example dataset is presented for argon at 100 mTorr with a cathode bias of -0.45 kV, a discharge current of ~3.5 mA, and the Langmuir probe 32.5 mm away from the cathode. Figure 31 shows a typical raw I-V curve where the peak probe current is 0.4 mA.

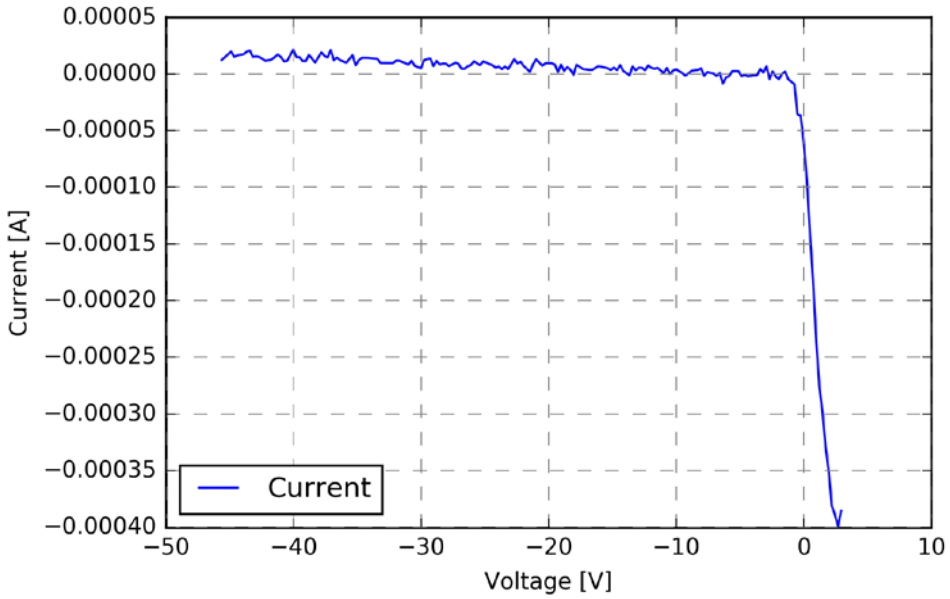

Figure 31. I-V curve for 100mTorr argon, -0.45 kV bias, current of 3.5 mA, and 37.5 mm Langmuir probe distance from cathode

The second derivative of the I-V curve needs to be taken, and it can be seen that the data has a fair amount of noise in it. A small window of 9-15 data points with a polynomial degree of 1-2 was chosen for Savitzky-Golay parameters, and the smoothing and subsequent numerical differentiation were performed. The Savitzky-Golay method is run twice - smoothing the data before each numerical differentiation is done. The relative window size to the total number of data points was between 4 - 7% which compares well with Magnus and Gudmundsson's relative window size to data set of 8% for their 81-point window with second order polynomial fitting. Figure 32 shows (a) the original data, (b) smoothed data, (c) dI/dV, and (d) the final measured EEDF.

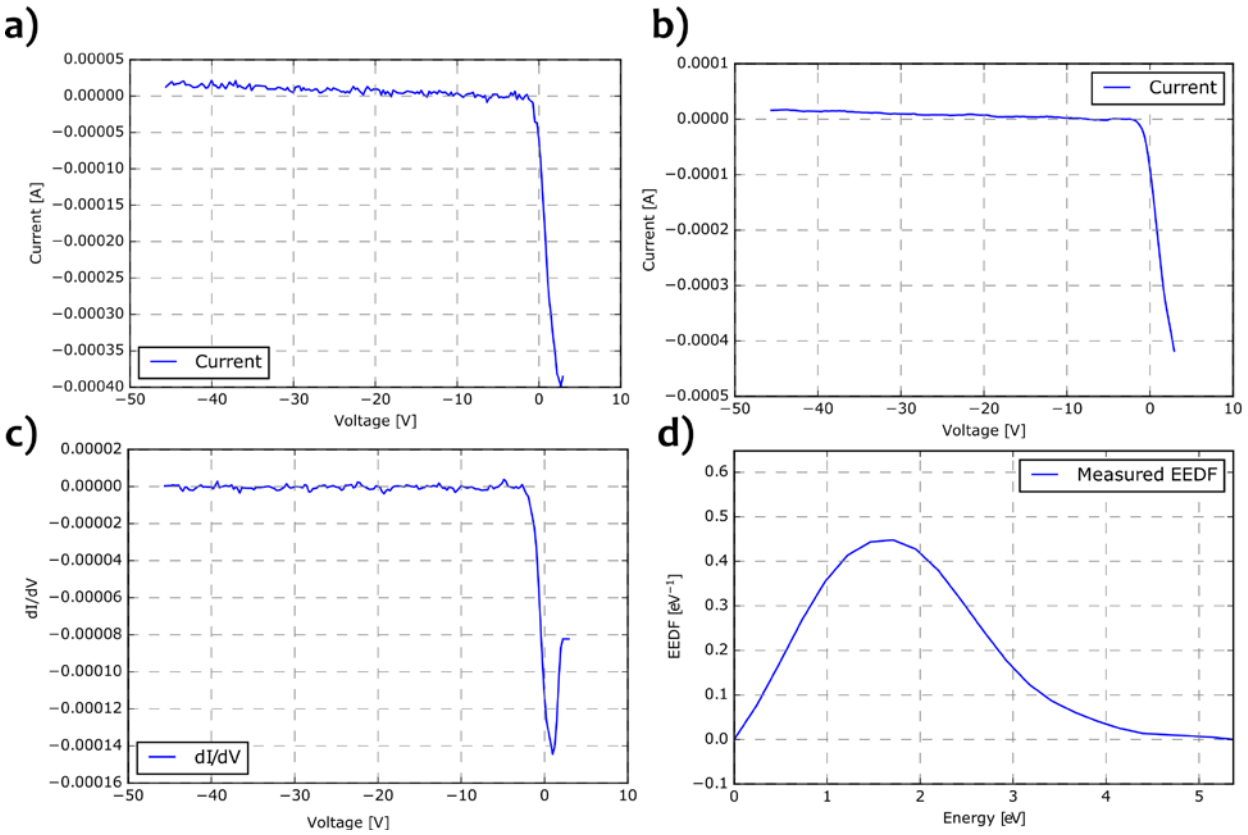

Figure 32. I-V curve smoothing and differentiation for 100 mTorr argon, -0.45 kV bias, 3.5 mA discharge current, and the probe 32.5 mm from cathode

It is useful to recognize in (c) the potential at the minimum current value corresponds to the plasma potential. This is the value that is stored as an energy reference point, i.e. at this probe bias, the electrons require no kinetic energy as there is no potential gradient between the plasma and the probe. It is eventually used in (2.7) for determining the EEDF in (d). The low energy electrons in d) are collected when there is a small potential gradient between the plasma potential and the probe bias, as the probe bias magnitude is increased (more negative) only higher energy electrons can overcome the probe's potential barrier and be collected. The electron temperature and density are then determined from (2.2) and (2.3). For this particular dataset $T_e = 1.15$ eV, $n_e = 1.77\,x\,10^{15}$ m^{-3}, and $\lambda_D = 1.75\,x\,10^{-4}$ m which corresponds to a regime between collisionless and collisional if

following Table 3. This means the Druyvesteyn method is bordering no longer being applicable and larger errors being present.

The procedure is performed for multiple I-V curves at the same position which are then averaged in order to reduce any remaining noise or erroneous characteristics from sudden micro discharges forming in the plasma. As the multiple scans are taken, the pressure was recorded in order to get an average pressure of the discharge. The standard deviation is found for all parameters - pressure, electron temperature, electron current - using (A2.1) in the appendix. Figure 33 shows the group of EEDFs for this probe position along with the averaged EEDF with a pressure of 98.6 ± 0.34 mTorr ≈100 mTorr.

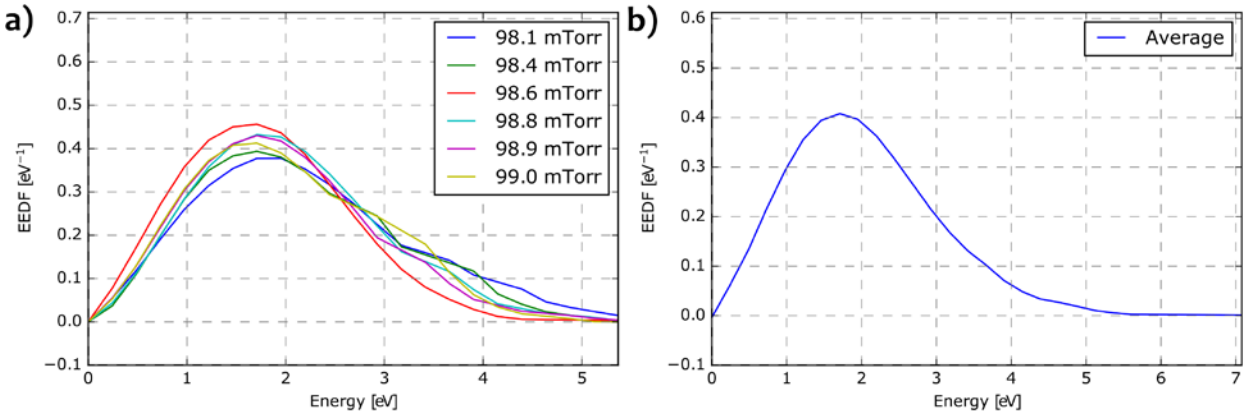

Figure 33. (a) EEDFs taken at 32.5 mm for 100 mTorr argon with a -0.45 kV cathode bias and 3.5 mA discharge current (b) Averaged EEDF

To check the distribution type, it was then plotted on a logarithmic scale for the EEPF. A distribution that is more linear on this scale is closer towards a Maxwellian distribution. As seen in Figure 34 the EEDF is nonlinear and therefore non-Maxwellian. The higher energy tail above ~ 7 eV is assumed to be from higher order oscillations that the smoothing did not correctly remediate and are disregarded when taking the integrals of the electron temperature and density.

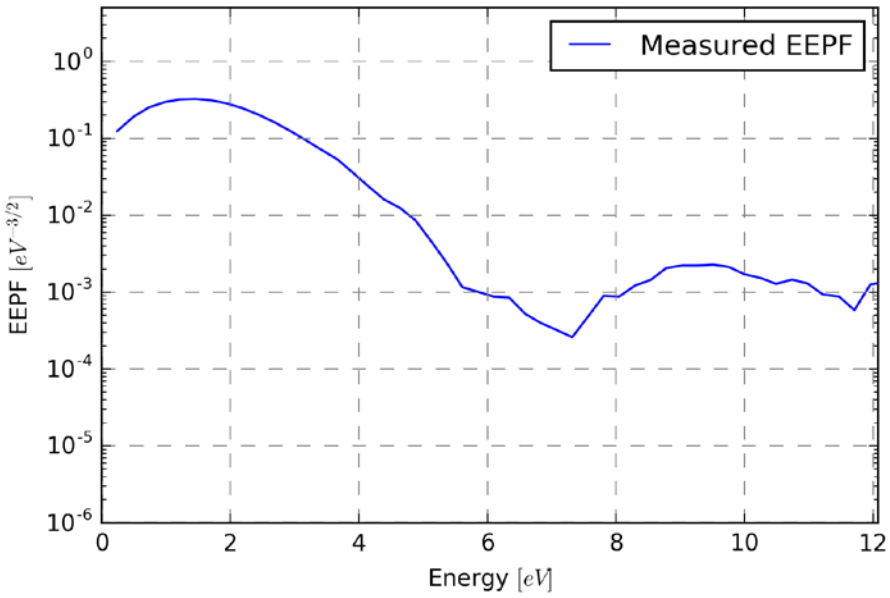

Figure 34. EEDF on a logarithmic scale

To see if this attribute is an artifact of the smoothing or inherent in the actual EEDF, the smoothing procedure's effects on ideal I-V curves was investigated. Too much smoothing tends to lower the distributions peak magnitude while simultaneously moving the peak to higher energies while creating a triangular type curve. Ideal currents for Maxwellian and Druyvesteyn distributions were simulated with random noise at 10% of the signal and put through the same Savitzky-Golay smoothing procedure. The ideal currents were derived and are in the appendix sections A2 and A3. For a 1.2 eV electron temperature, an ideal Maxwellian I-V curve along with the same curve with randomly generated noise superimposed are shown in Figure 35 a). The resulting EEDFs for an ideal Maxwellian distribution, an ideal I-V curve processed by the Savitzky-Golay method, and the noise influenced I-V curve processed by the Savitzky-Golay method are in b). Lastly, c) shows these EEPFs and it can be seen that smoothing does not affect the characteristic straight line feature of the Maxwellian distribution EEDF.

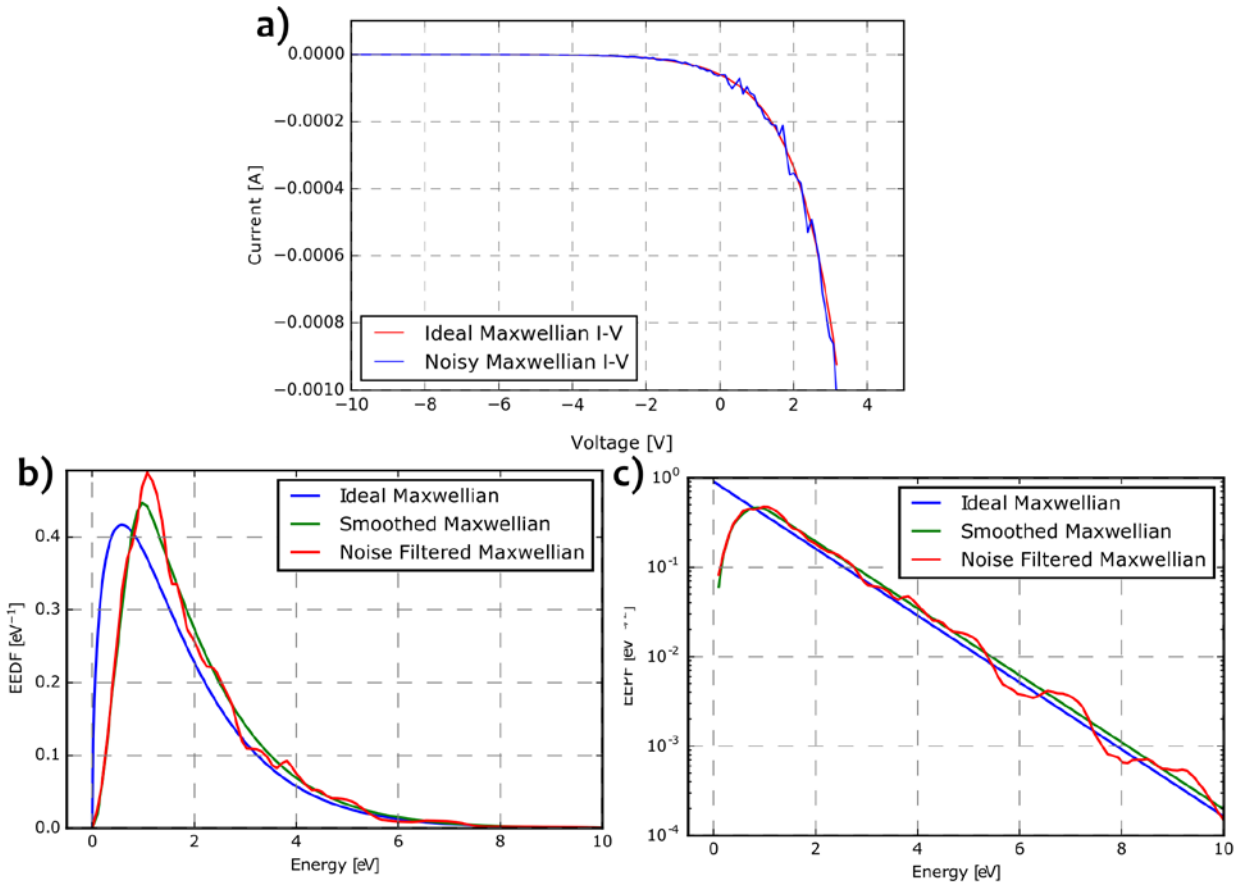

Figure 35. (a) Ideal Maxwellian I-V curve with noise influenced curve (b) Ideal Maxwellian EEDF, EEDF from smoothed ideal I-V curve, and EEDF from noise added I-V curve (c) EEPFs

The smoothed Maxwellian curve does match well with the noise filtered Maxwellian; however both are shifted from the ideal distribution. This leads to an increase in electron temperature; shown in the smoothed ideal Maxwellian distribution generated $T_e = 1.35$ eV while the noise filtered Maxwellian produced $T_e = 1.32$ eV - a 2% difference. Both are higher than the input electron temperature of $T_e = 1.2$ eV by ~10% - shown in Table 4. The electron densities are unaffected by the smoothing.

Table 4. Electron temperature from a smoothed ideal Maxwellian I-V curve and from a noise influenced Maxwellian I-V curve

EEDF	T_e [eV]	Percent Difference from Ideal T_e
Smoothed Maxwellian	1.35	12 %
Noise Filtered Maxwellian	1.32	10 %

The ideal Druyvesteyn I-V curve along with its noisy counterpart and calculated EEDFs are shown in Figure 36.

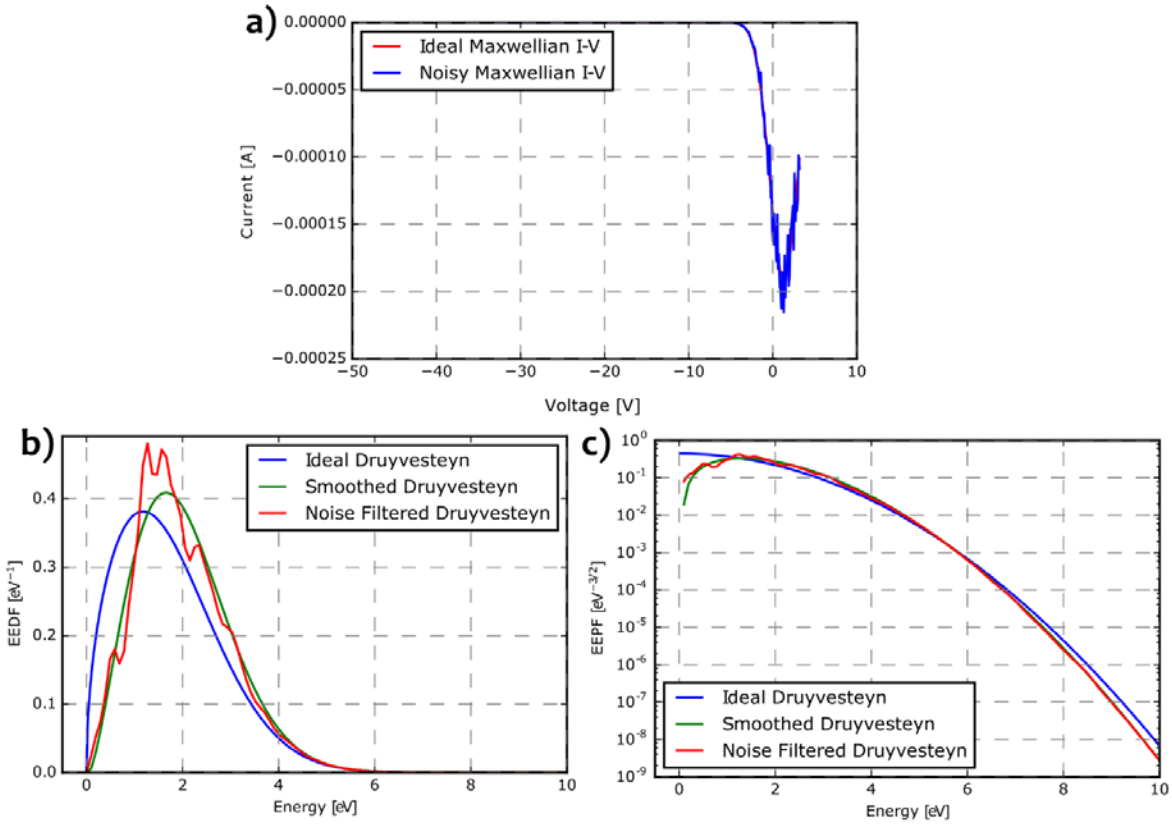

Figure 36. (a) Ideal Druyvesteyn I-V curve with noise influenced curve (b) Ideal Druyvesteyn EEDF, EEDF from smoothed ideal I-V curve, and EEDF from noise added I-V curve (c) EEDFs

Again, the ideal smoothed EEDF matches well with the noise filtered one, but both are shifted towards slightly higher energies than the Maxwellian distributions - summarized in Table 5.

Table 5. Electron temperature from a smoothed ideal Druyvesteyn I-V curve and a noise influenced Druyvesteyn I-V curve

EEDF	T_e [eV]	Percent Difference from Ideal T_e
Smoothed Druyvesteyn	1.36	13 %
Noise Filtered Druyvesteyn	1.33	11 %

In light of the filter producing electron temperatures roughly 10% higher than those expected, an approach was employed to reverse the effects. This centered around iterating a function that would take an initial estimate of the ideal electron temperature and slowly increase it until the resulting smoothed EEDF produced an electron temperature that converged with the measured value. This allows for better estimating the actual electron temperature in the plasma and counteracts at least some of the inherent errors in smoothing data. The final result of the averaged EEDF with its corresponding ideal Maxwellian and Druyvesteyn distributions that went through the same smoothing procedure are shown in Figure 37. This makes it clear that for a 100 mTorr argon plasma with a -0.45 kV bias at 32.5 mm from the cathode the measured EEDF is Druyvesteyn. The electron temperature was 1.4 ± 0.17 eV and the electron density was $1.8 \pm 0.4\, x\, 10^{15}$ m^{-3}.

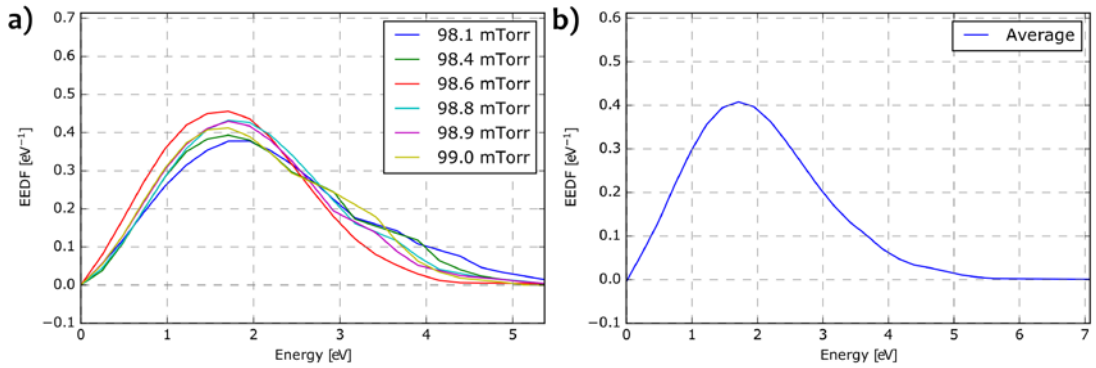

Figure 37. (a) Measured average EEDF with corresponding smoothed Maxwellian and Druyvesteyn distributions of the same electron temperature (b) EEPF

Despite being able to reduce the noise in the I-V curves and counteract the energy shift in the resulting EEDFs, it is difficult to say the accuracy of the electron temperature and density. Sources of systematic error abound - convolutions of instruments' effects, subsequent smoothing and differentiation of the data, and probe contamination and sputtering. Despite these influences, Godyak consistently stated errors of less than 10% for T_e and n_e while using the Druyvesteyn method within the appropriate pressure regimes (and even higher pressures) and errors up to an order of magnitude from other theories [41]. Taking this into account, the associated error for these measurements was considered as the standard deviation found while iterating multiple datasets for the same probe position coupled to an added flat 10% error.

2.4.2 Langmuir Probe EEDFs

The Savitzky-Golay procedure was done for ten probe positions relative to the cathode. Each location had 5-7 I-V scans which were smoothed and averaged to produce the EEDFs, electron temperature, and electron density. The following results are for a 100 mTorr argon plasma operating with a -0.45 kV bias at 3.5 mA discharge current. Figure 38 and Figure 39 display the electron density and temperature respectively.

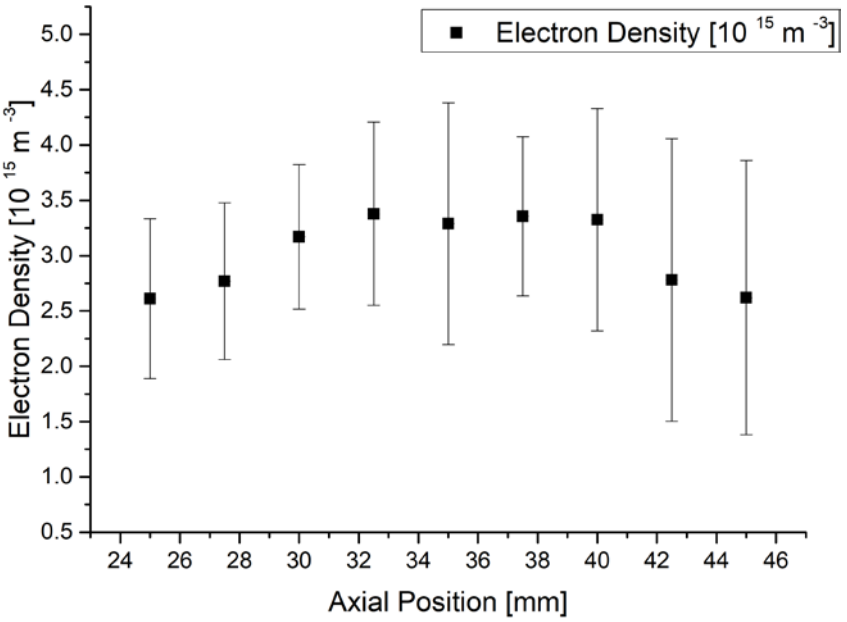

Figure 38. Electron density versus axial position from the cathode

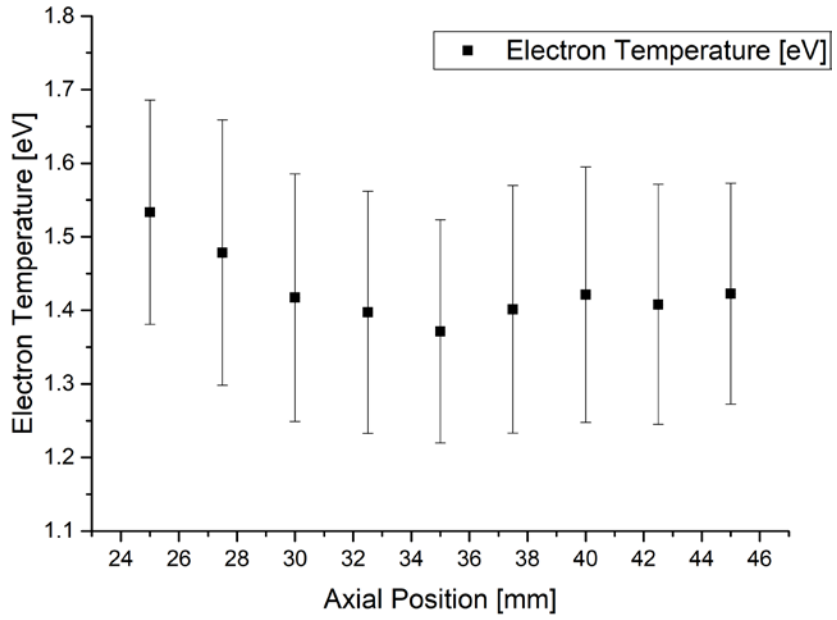

Figure 39. Electron temperature versus axial position from the cathode

It is seen that the electron density increases as the probe approaches the cathode and decreases. This is expected due to the probe nearing the plasma sheath and its reduction in electrons. The electron temperature showed the inverse trend decreasing to a minimum and then increasing towards the plasma sheath. This accurately correlates with the

electron density, i.e. as the plasma becomes denser the electrons have higher interaction probabilities and can thermalize to lower temperatures.

The resulting energy distributions versus axial positions are best visualized in their non-normalized EEPF form as 3D waterfall plots. Figure 40 and Figure 41 show two perspectives of the EEPFs, the first is intended to emphasize the change in relative peak heights which correspond to electron densities and the second is to show the gradual extension of the higher energy tails. Figure 41 also displays how the EEPFs transition from Maxwellian type distributions at low densities toward a more Druyvesteyn like distribution in the middle of probe path at higher densities and then back to a straight Maxwellian type.

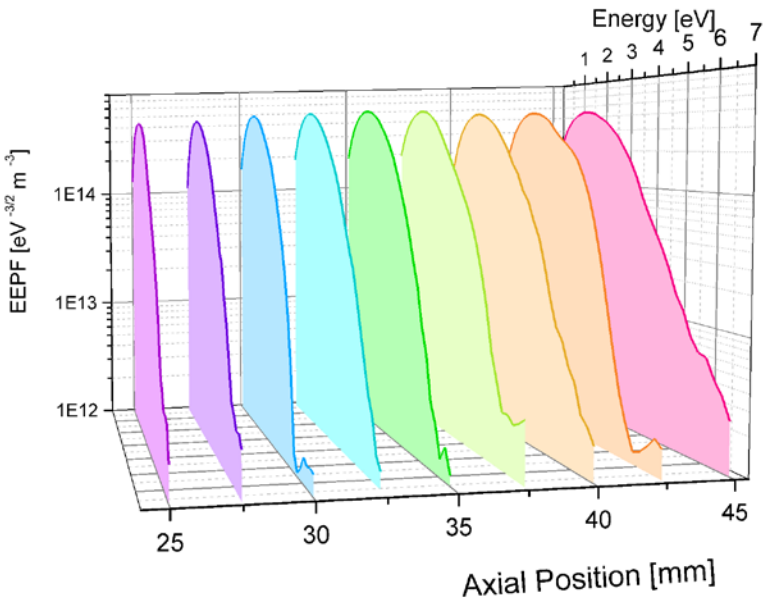

Figure 40. Langmuir probe EEPFs - view was chosen to emphasize peak heights

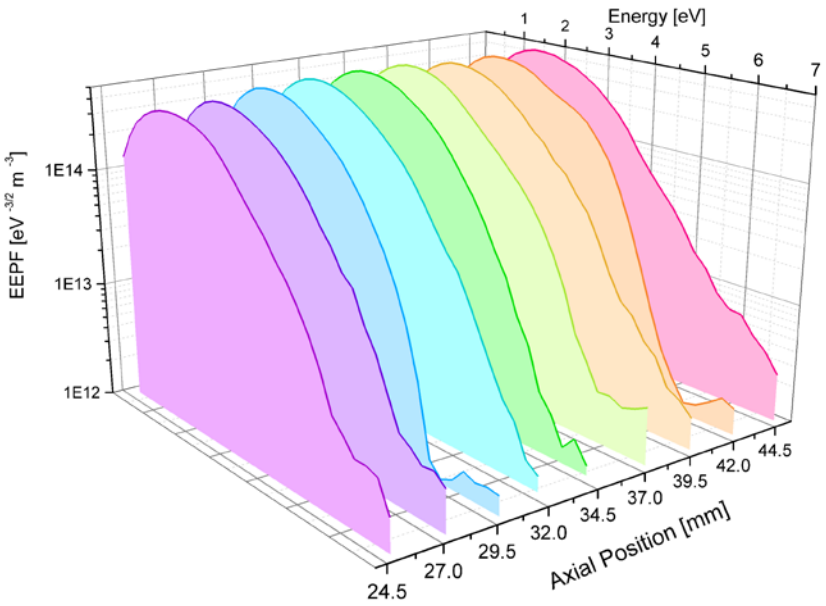

Figure 41. Langmuir probe EEPFs - view was chosen to emphasize distribution tails

2.4.3 Discussion

The resulting electron temperatures and densities fit well with expectations, and the EEPFs illustrated the distribution's transition from Maxwellian to Druyvesteyn. Unfortunately, EEDFs were only found for argon while under conditions to remain close to the collisionless regime. The deuterium discharges would consistently produce electron energies and temperatures leading to Debye lengths that were 3-4 times the mean free path and probe radius putting it well out of the Druyvesteyn method's applicability. Even so, these EEDFs can be compared to those produced through computational methods which are outlined in Chapter 3.

CHAPTER 3: DC Discharge COMSOL Simulation

3.1 Simulation Overview

Being able to accurately simulate the discharge allows estimating electron temperatures and densities in regimes where using the Langmuir probe is no longer applicable. Accordingly, modeling the system also allows for additional information to be extracted. In particular, with accurate kinetic reaction rates, it would allow for the approximation of incident ion energies on the cathode material. This is beneficial in understanding damage schema and can be input parameters for a SRIM study. The model was initially run as a 1D simulation, but this is not presented here as it would be redundant to explain both it and the 2D model while the 2D model is more encompassing of the system's features. Hence, the 2D model is covered. Since only the argon EEDFs were found, argon is the source species for the model for validation purposes.

The final working model incorporated a coupling of the plasma module with the Boltzmann equation, two-term approximation module. Since parameters like the electron mobility and ionization degree are not known a priori for the computation of the Boltzmann equation, an iterative approach is used. It first computes the electron transport properties and EEDFs. This better represents the kinetics of discharges with low ionization fractions and electron mobility being highly dependent on the electric field as is the case with DC plasmas. The resulting Townsend coefficients and reduced transport properties are then used for the reaction coefficients in the plasma module. Once the plasma module finishes, evaluations of the required input parameters for the Boltzmann module are found. These are used in the subsequent cycle of the alternating process between the Boltzmann equation module and plasma module until a convergence criterion

is met - typically 0.01 percent deviation in values between iterations. The EEDFs with spatial dependence can then be studied.

3.2 Fundamental Equations

The modeling begins with implementing the COMSOL plasma module for DC discharges. This module is best suited for pressures above 1 mTorr where the discharge is weakly ionized. A constraint in the model is that the plasma is assumed to be collisional in order to use approximations for the diffusion of particles. The electron and mean electron energy are found by solving the drift-diffusion equations while neglecting convection motion of electrons. A full derivation of the drift-diffusion equations can be seen in [52], but the final form is

$$\begin{gathered}\frac{\partial}{\partial t}(n_e) + \nabla \cdot [-\mathrm{n_e}(\boldsymbol{\mu}_e \cdot \boldsymbol{E}) - \boldsymbol{D}_e \cdot \nabla n_e] = R_e \\ \frac{\partial}{\partial t}(n_\epsilon) + \nabla \cdot [-\mathrm{n_\epsilon}(\boldsymbol{\mu}_\epsilon \cdot \boldsymbol{E}) - \boldsymbol{D}_\epsilon \cdot \nabla n_\epsilon] + \boldsymbol{E} \cdot \boldsymbol{\Gamma}_\mathrm{e} = R_\epsilon \\ where, \quad \boldsymbol{\Gamma}_e = -(\boldsymbol{\mu}_e \cdot \boldsymbol{E}) n_e - \boldsymbol{D}_e \cdot \nabla n_e \\ \boldsymbol{D}_e = \boldsymbol{\mu}_e \boldsymbol{T}_e, \quad \boldsymbol{\mu}_\epsilon = \left(\frac{5}{3}\right)\boldsymbol{\mu}_e, \quad \boldsymbol{D}_\epsilon = \boldsymbol{\mu}_\epsilon T_e\end{gathered} \tag{3.1}$$

Where $\boldsymbol{\mu}_e$ is the electron mobility, $\boldsymbol{E}$ is the electric field, $\boldsymbol{D}_e$ is the electron diffusivity, and $\boldsymbol{\Gamma}_\mathrm{e}$ is the electron flux. R_e is the electron source, and R_ϵ is the energy loss due to inelastic collisions. The source terms are determined from the plasma chemistry using rate coefficients. The electron source term rate coefficient for M reactions is

$$R_e = \sum_{j=1}^{M} x_j k_j N_n n_e \tag{3.2}$$

Where x_j is the mole fraction of target species for reaction j, k_j is the rate coefficient for reaction j, and N_n is the neutral number density. It is important here to note that for DC discharges the reaction rates are more accurately represented by using Townsend coefficients instead of rate coefficients. The Townsend coefficients are derived by the ratio between rate coefficients and drift velocity; this produces a relationship between reaction rate and electric field which is useful for when the electron flux is electric field driven as is the case with DC discharges. When using Townsend coefficients, the electron source is:

$$\begin{gathered} R_e = \sum_{j=1}^{M} x_j \alpha_j N_n |\boldsymbol{\Gamma}_e| \\ where, \qquad \alpha_j = \frac{k_k}{w} \\ w = -\left(\frac{\gamma}{3}\right)\left|\left(\frac{E}{N_n}\right)\right| \int_0^{\infty} \frac{\epsilon}{\sigma_m}\left(\frac{\partial f}{\partial \epsilon}\right) d\epsilon \\ k_k = \gamma \int_0^{\infty} \epsilon \sigma_k(\epsilon) f(\epsilon) d\epsilon \end{gathered} \tag{3.3}$$

Here α_j is the Townsend coefficient, k_k is the rate coefficients calculated from energy-dependent electron reaction cross sections $\sigma_k(\epsilon)$ with an assumed energy distribution $f(\epsilon)$, w is the drift velocity, and $\gamma = \left(\frac{2q}{m_e}\right)^{\frac{1}{2}}$. An essential relation in (3.3) is how the rate coefficients are dependent on an energy distribution. The COMSOL plasma module allows you to assume a Maxwellian, Druyvesteyn, or generalized distribution. The electron

collisional energy losses are summed over all inelastic reactions, P, to get the electron energy loss term:

$$R_\epsilon = \sum_{j=1}^{P} x_j k_j N_n n_e \Delta\epsilon_j$$
$$using\ Townsend\ coefficients: R_\epsilon = \sum_{j=1}^{P} x_j \alpha_j N_n |\Gamma_e| \Delta\epsilon_j \tag{3.4}$$

where $\Delta\epsilon_j$ is the energy loss from the reaction j. The mass fractions for heavy non-electron species are computed using

$$\frac{\rho\partial}{\partial t}(w_k) + \rho(u \cdot \nabla)w_k = \nabla \cdot j_k + R_k \tag{3.5}$$

Poisson's equation for electrostatics is used for calculating the electrostatic field:

$$-\nabla \cdot \epsilon_0 \epsilon_r \nabla V = \rho \tag{3.6}$$

where ϵ_0 and ϵ_r are the vacuum and relative permittivity and the space charge density is found based on plasma chemistry using

$$\rho = q\left(\sum_{k=1}^{N} Z_k n_k - n_e\right) \tag{3.7}$$

where Z_k is the charge of species k. For simulating a DC discharge, the boundary conditions are important as the emission of secondary electrons sustains the discharge. The electron flux and energy flux are given by:

$$-n \cdot \Gamma_e = \left(\frac{1}{2} v_{e,th} n_e\right) - \sum_p \gamma_p (\Gamma_p \cdot n)$$
$$-n \cdot \Gamma_\epsilon = \left(\frac{5}{6} v_{e,th} n_\epsilon\right) - \sum_p \epsilon_p \gamma_p (\Gamma_p \cdot n) \tag{3.8}$$

The term γ_p represents the secondary emission coefficient which is specific to the cathode material and also the incident ion species. Typically, Nastasi [21] was used as a reference for these values either from Table 9.1 or equation (9.3.4) which is shown below where ϵ_{iz} is the ionization energy of the incident ion and ϵ_ϕ is the work function of the cathode material.

$$\gamma_p \approx 0.016\left(\epsilon_{\text{iz}} - 2\epsilon_\phi\right) \tag{3.9}$$

Lastly, ions are lost to the walls and cathode via

$$-n \cdot j_k = M_w R_k + M_w c_k Z \mu_k (E \cdot n)[Z_k \mu_k (E \cdot n) > 0] \tag{3.10}$$

where M_w is the molecular weight of the species.

In order to circumvent the limitation of assuming a specific EEDF in (3.3), the plasma module was coupled to the Boltzmann equation, two-term approximation model. Solving the two-term approximation Boltzmann equation allows for a more consistent representation of the kinetic and fluid properties of electron dynamics. The entire derivation can be found in [52] or [42], but the computationally intensive Boltzmann equation which describes the evolution of a six-dimensional phase space distribution f is

$$\frac{\partial f}{\partial t} + \boldsymbol{v} \cdot \nabla f - \frac{e}{m}(\boldsymbol{E} \cdot \nabla_{\boldsymbol{v}} f) = C[f] \tag{3.11}$$

where $\boldsymbol{v} \cdot \nabla f$ is the diffusion term, $\frac{e}{m}(\boldsymbol{E} \cdot \nabla_v f)$ is the electric force term, and $C[f]$ is the collision term that incorporates inelastic reactions. This is simplified to

$$\frac{\partial}{\partial \epsilon}\left(Wf - \frac{D\partial f}{\partial \epsilon}\right) = S$$
$$where, \qquad W = -\gamma \epsilon^2 \sigma_\epsilon - 3a\left(\frac{n_e}{N_n}\right)A_1 \tag{3.12}$$
$$D = \frac{\gamma}{3}\left(\frac{E}{N_n}\right)^2\left(\frac{\epsilon}{\sigma_m}\right) + \frac{\gamma k_b T}{q}\epsilon^2\sigma_\epsilon + 2a\left(\frac{n_e}{N_n}\right)\left(A_2 + \epsilon^{\frac{3}{2}}A_3\right)$$

With the following required expressions

$$a = \frac{q^2\gamma}{24\pi\epsilon_0^2} ln\Lambda$$
$$\Lambda = \frac{12\pi\left(\frac{2\epsilon_0 q\bar{\epsilon}}{3}\right)^{\frac{3}{2}}}{q^3 n_e^{\frac{1}{2}}}$$
$$\sigma_m = \sum_{k=all} x_k\sigma_k$$
$$\sigma_\epsilon = \sum_{k=elastic} 2\left(\frac{m_e}{M}\right)x_k\sigma_k \tag{3.13}$$
$$A_1 = \int_0^\epsilon u^{\frac{1}{2}} f(u)du$$
$$A_2 = \int_0^\epsilon u^{\frac{3}{2}} f(u)du$$
$$A_3 = \int_0^\infty f(u)du$$

Where σ_m is the total collision-cross section, σ_ϵ is the total elastic collision cross section, Λ is the Coulomb logarithm, and M is the mass of the target species. The full form of the S term is not shown here, but it represents the summation of energy lost due to all inelastic collisions

$$S = \sum S_{inelastic} \tag{3.14}$$

3.3 Simulation Geometry and Mesh

The plasma model was run in a two-dimensional geometry. It is shown along with the mesh in Figure 42 where the active walls in the geometry are highlighted blue. The model is intended to be only one-fourth of the system's cross-section to reduce computation runtime. The discharge gap was held at 6.5 cm while the distance from the tip of the cathode to the dielectric wall (approximating the Kodial window) was 7 cm.

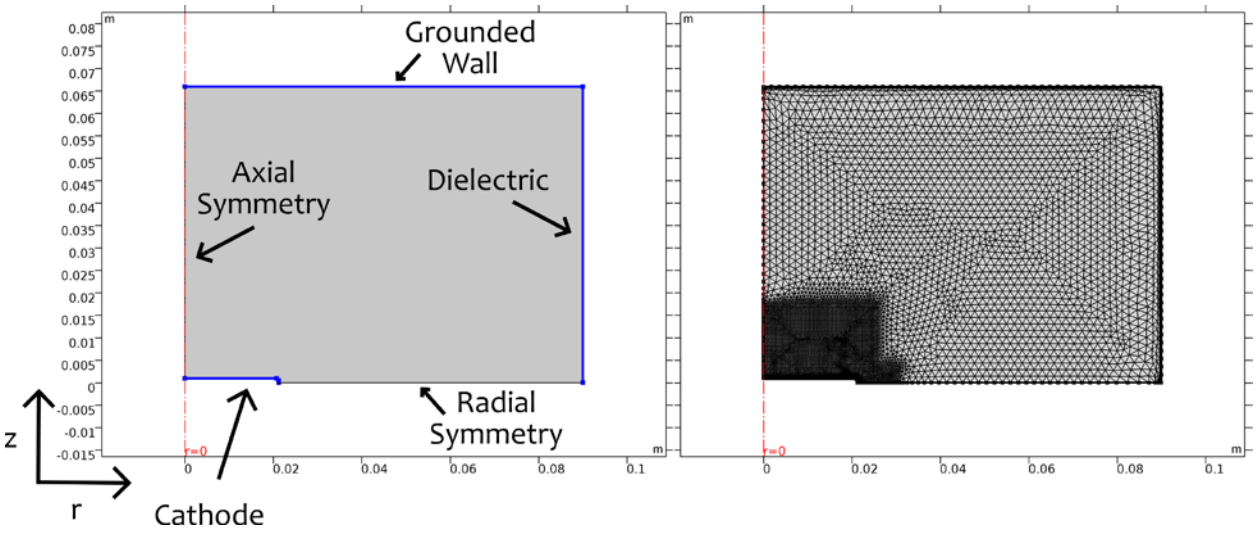

Figure 42. COMSOL plasma module geometry and mesh

A quantitative mesh study was not done. However, it was found that the mesh needed a significant refinement closer to the cathode to account for plasma sheath kinetics. A close-up view near the cathode is in Figure 43.

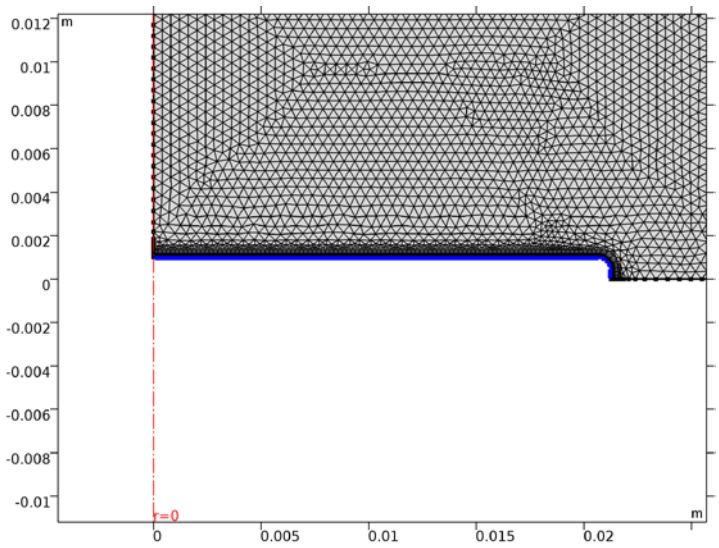

Figure 43. Mesh density at the cathode

3.4 Argon Reaction Scheme

The reaction scheme for argon was used from the COMSOL reference [53]. The plasma reactions are shown in Table 6 along with their type, designated as elastic, excitation, superelastic, etc., and the reaction's electron energy loss $\Delta\epsilon$. Table 7 shows the surface reactions on the cathode and walls, there are six types of reactions relevant in the argon discharge: elastic, excitation, superelastic (de-excitation), ionization, penning ionization, and metastable quenching.

Table 6. Reactions, type, and corresponding electron energy difference

Reaction	Formula	Type	$\Delta\epsilon\ [eV]$
1	$e + Ar \rightarrow e + Ar$	Elastic	0
2	$e + Ar \rightarrow e + Ars$	Excitation	11.5
3	$e + Ars \rightarrow e + Ar$	Superelastic	-11.5
4	$e + Ar \rightarrow 2e + Ar^+$	Ionization	15.8
5	$e + Ars \rightarrow 2e + Ar^+$	Ionization	4.24
6	$Ars + Ars \rightarrow e + Ar + Ar^+$	Penning ionization	
7	$Ars + Ar \rightarrow Ar + Ar$	Metastable quenching	

Table 7. Surface reactions

Reaction	Formula	Sticking Coefficient	γ_p
1	$Ars \rightarrow Ar$	1	0
2	$Ar^+ \rightarrow Ar$	1	0.25

The mean energy of the secondary electrons was always taken to be equal to $\epsilon_{iz} - 2\epsilon_{\phi}$ where the work function for the palladium electrode was 5 eV. The secondary electron emission coefficient chosen was $\gamma_{se} = 0.2$.

3.5 Argon Simulation Results

The quantities relevant to the measured EEDF results are the electron temperature and density. These are produced as 2D plots and are shown below

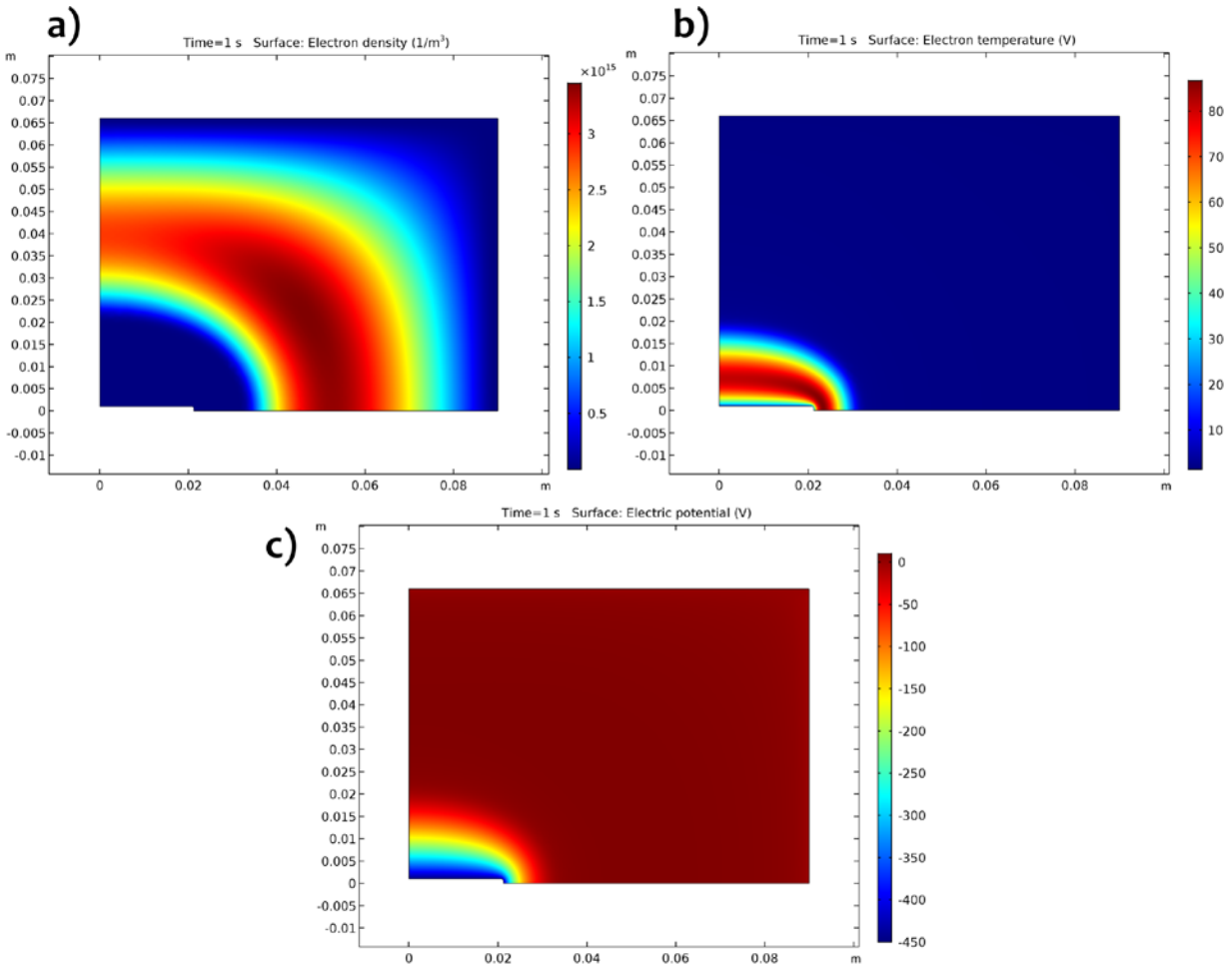

Figure 44. Results for 100 mTorr argon plasma with -0.45 kV cathode (a) Electron density (b) Electron temperature (c) Electric potential

The electron density has a maximum value of $3.5\,x\,10^{15}\ \mathrm{m}^{-3}$ and a maximum electron temperature of 84 eV near the corner of the cathode due to the increased electric potential gradient. However, these values are not directly comparable to the Langmuir probe data, consequently, a 1D line sample was taken at $r = 1\ \mathrm{cm}$ which roughly corresponds to the Langmuir probe's position. Figure 45 shows maximums of $n_e = 3\,x\,10^{15}\ \mathrm{m}^{-3}$ at $\mathrm{z} = 3.75\mathrm{cm}$

and $T_e = 82$ eV at z = 0.6 cm. Plots similar to Figure 38 and Figure 39 for the measured electron density and temperature, respectively, versus distance from the cathode were then made. Constant error estimates of 20% and 10% were used for the electron density and temperature respectively to express the uncertainty in the Langmuir probe radial position. The electron temperature was chosen to have a low uncertainty due to it varying less in the region of interest. These are shown in Figure 46 and Figure 47.

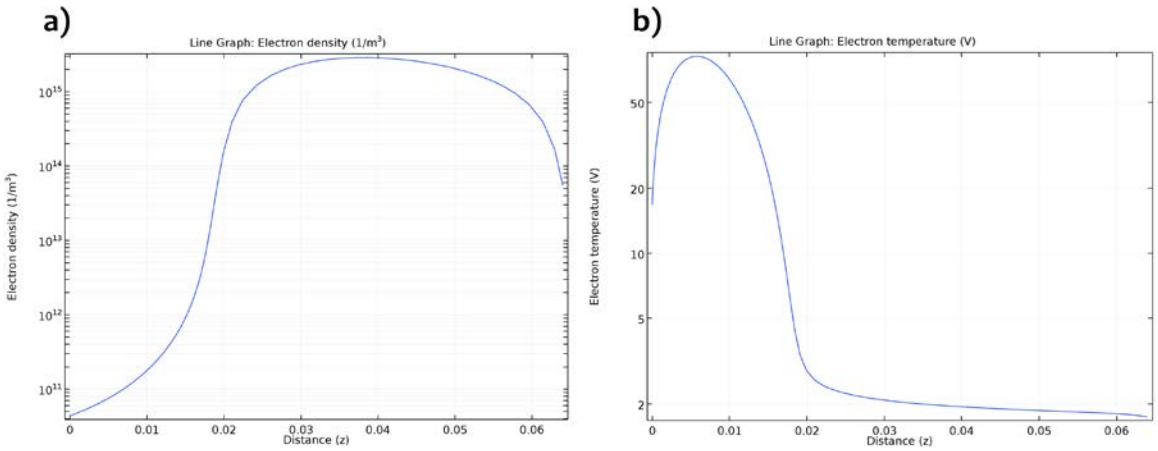

Figure 45. Electron density and temperature along r = 1 cm

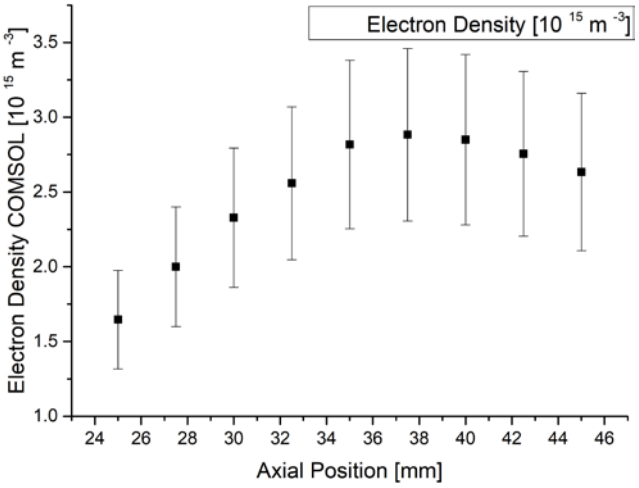

Figure 46. Electron density versus axial position from cathode - COMSOL

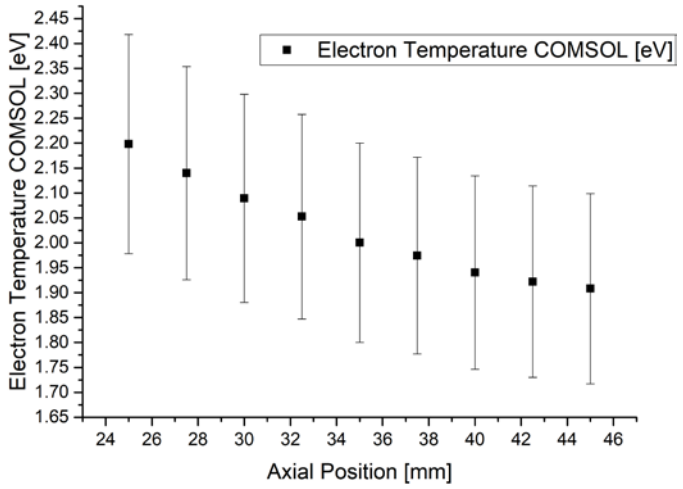

Figure 47. Electron temperature versus axial position from the cathode - COMSOL

As was seen with the Langmuir probe data, the electron density increases as the position approaches the cathode and then decreases once inside the plasma sheath and the electron temperature has a steady increase. Lastly, the EEDFs dependence on position is shown below:

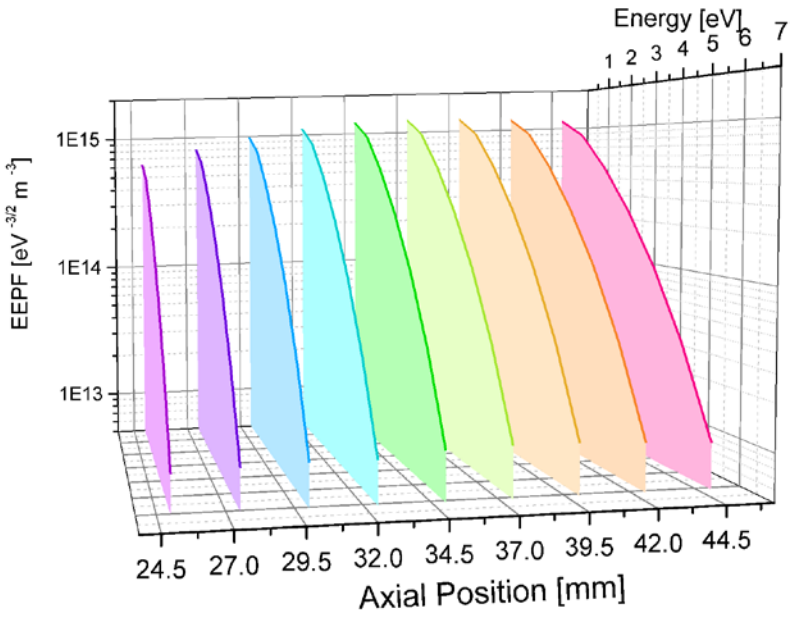

Figure 48. COMSOL EEPFs - view is chosen to emphasize peak heights

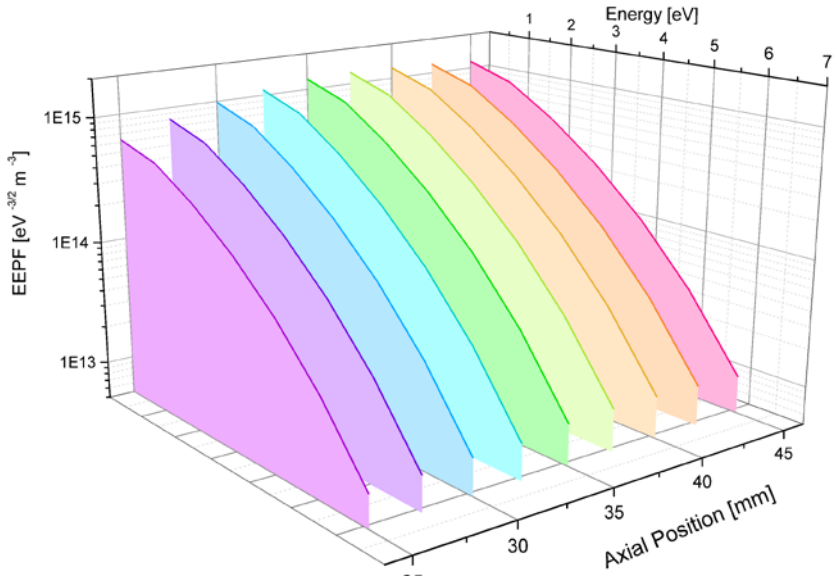

Figure 49. COMSOL EEPFs - view was chosen to emphasize distribution tails

3.6 Comparison of Experimental and Simulation Results

It is useful to compare the Langmuir probe and COMSOL data side by side to get a better understanding of any differences. For this section, it was also decided to do a more classical Langmuir probe analysis - refined Orbital Motion Theory also known as the Laframboise method. This method is detailed in [54] and [55] and was implemented in an automated python script which analyzed the same data used for the Druvesteyn method. The electron densities and temperatures are then shown on the same plots.

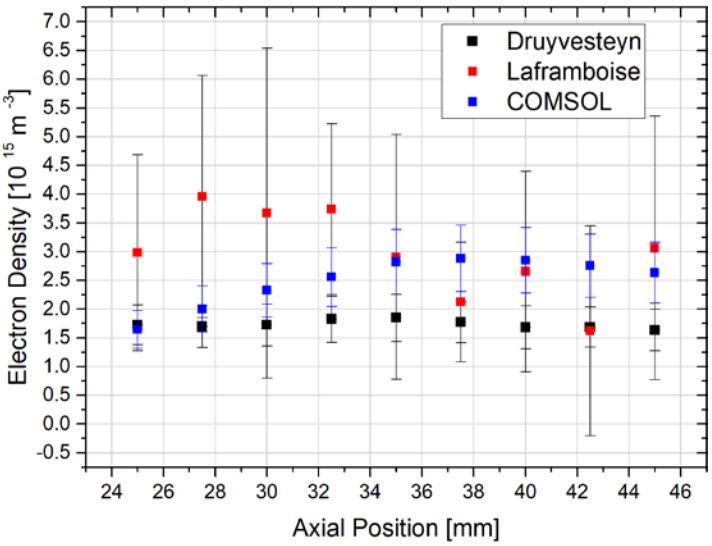

Figure 50. Electron density from the Druyvesteyn, Laframboise, and COMSOL methods

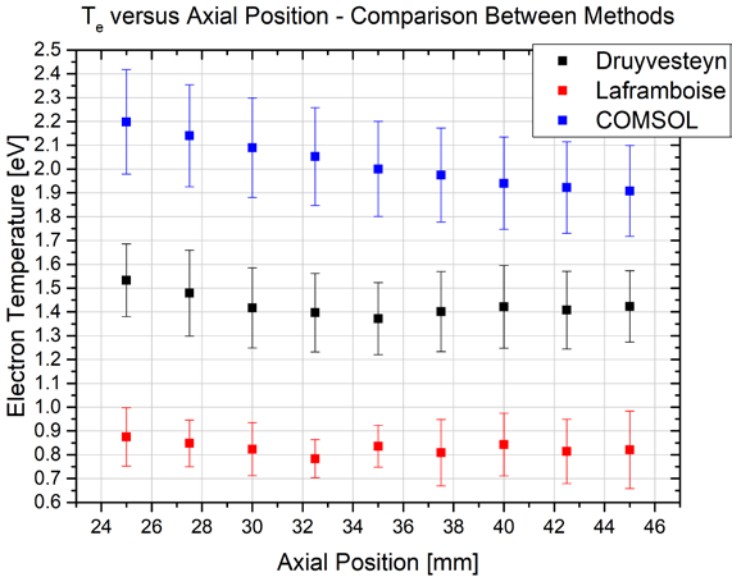

Figure 51. Electron temperature from the Druyvesteyn, Laframboise, and COMSOL methods

These demonstrate that for all methods as the probe approaches the cathode the general trends are followed: the electron density slowly increases to a maximum and then decreases, and the electron temperature steadily increases. The differences are in the position of the general features, e.g. density maximum, and magnitudes. For the electron current, it seemed that at positions further away from the cathode the COMSOL method matched closely with the Laframboise method opposed to the Druyvesteyn method. The

Laframboise method is either able to better account for the increased electron densities, or the discrepancy could be due to the COMSOL simulation results using a probe path that varied from the actual path. The electron temperature plot in Figure 51 shows that the COMSOL results consistently had the highest energies followed by the Druyvesteyn and Laframboise methods respectively. A possibility for why the Laframboise method produces the lowest electron temperatures is most likely due to the assumption that the EEDFs are Maxwellian which neglects the increased probability of higher energy electrons. Also, it is important to note that the standard deviation in the Laframboise method was significantly higher than that of the Druyvesteyn method, particularly for the electron density estimates - sometimes approaching 80% of the measured value compared to 20% from the Druyvesteyn analysis.

The non-normalized EEPFs were found to be the best for comparison of the features from the COMSOL and Druyvesteyn methods. The same vantage points are shown as before where one is meant to emphasize the electron density, Figure 52, and the other the electron temperature, Figure 53.

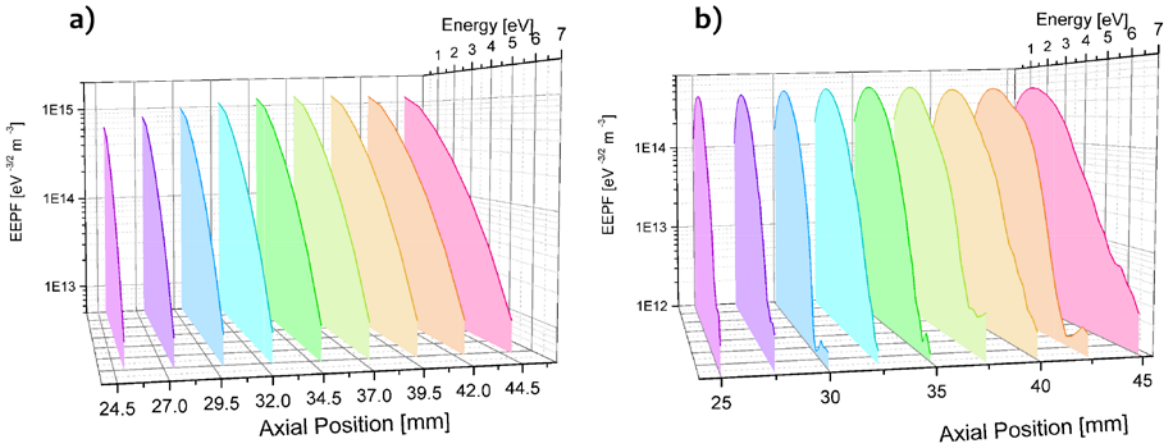

Figure 52. COMSOL (a) and Langmuir probe (b) EEPFs - view chosen to emphasize peak heights

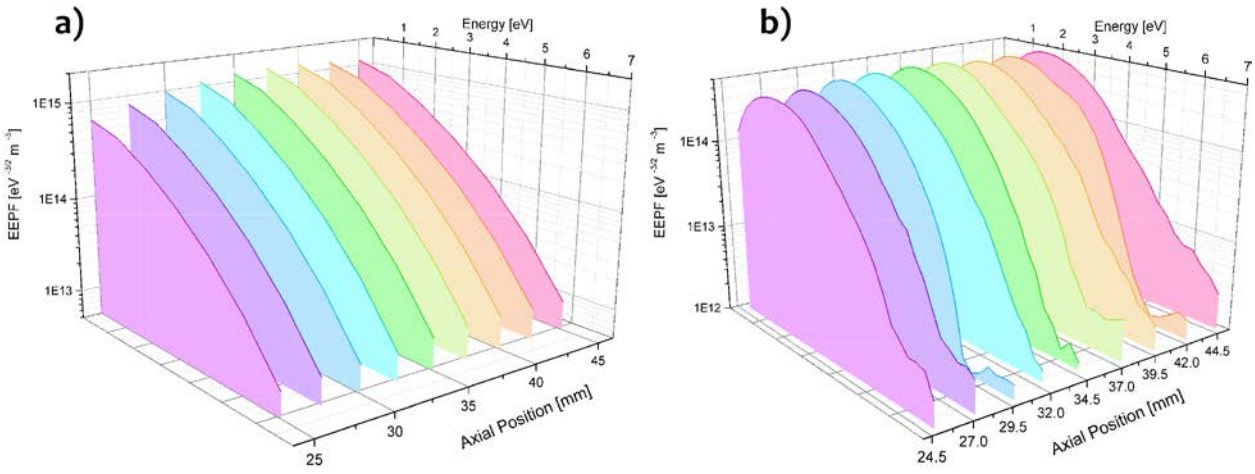

Figure 53. COMSOL (a) and Langmuir probe (b) EEPFs - view chosen to emphasize distribution tails

Over the same energy scale bounds, the COMSOL trends for the electron density are far more noticeable while the distribution's tail characteristic is more apparent in the Langmuir probe's EEPFs. Another vantage point was chosen to attempt to visualize better the EEPFs' features shown in Figure 54 and Figure 55 where color-coded arrows are intended to represent the features going from high values (red) to low (blue) or vice-versa.

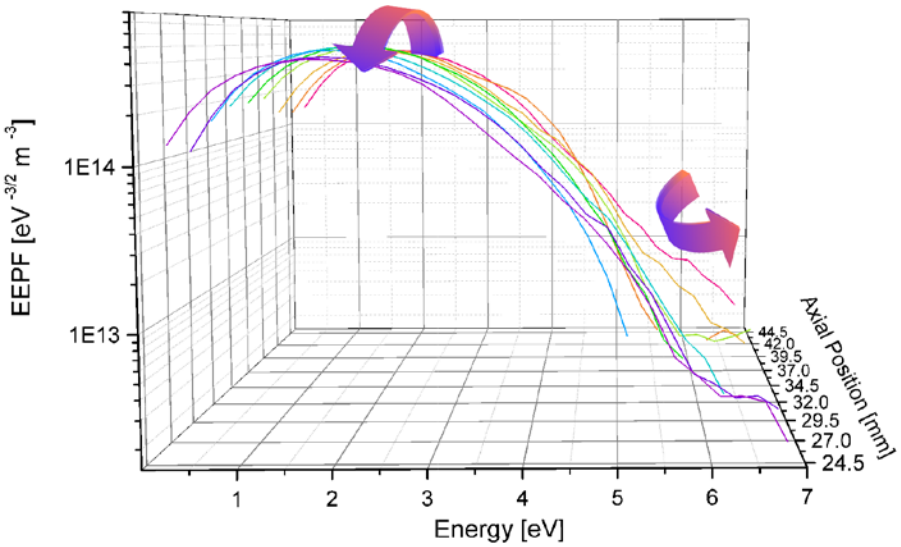

Figure 54. EEPF for Langmuir probe - color-coded arrows show trends going from higher values (red) to lower values (blue) or vice-versa

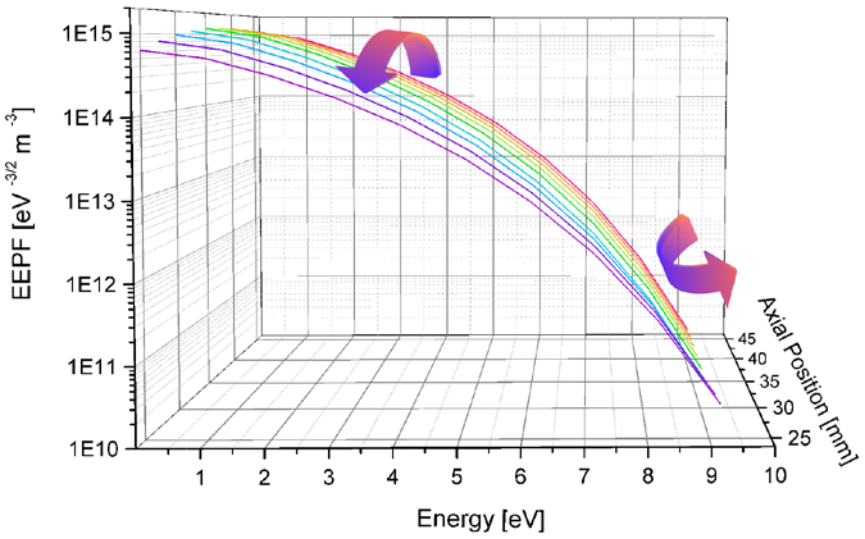

Figure 55. EEPF for COMSOL - color-coded arrows show trends going from higher values (red) to lower values (blue) or vice-versa

With the EEPFs showing similar trends for both methods, a conclusion can be made on the effectiveness of the Druyvesteyn method and COMSOL simulation. It was decided that the this presented a reasonable estimation of the EEPFs. Therefore, the COMSOL model accurately captured the dynamics of the system - validating the model and its use for higher pressures and for probing the kinetics of incident ions.

3.7 Model Extensions

3.7.1 Ion Angular Energy Distribution Functions

COMSOL's particle tracing module was then implemented in order to obtain the incident ion energies. The reader is referred to the COMSOL plasma module manual for specifics on how the particle tracing is performed [52]. The model uses the converged solution of the electric potential from the coupled Plasma-Boltzmann modules as mentioned earlier for the specifying the electric force acting on the ions. Ions were then released from a grid, and their trajectories and kinetic energies were stored - only the ion values for those incident on the cathode were stored. 100 ions per velocity space direction were released. The release grid was chosen to be slightly above the interface of the plasma sheath

potential drop. An example of the grid and the particles' trajectories are shown in Figure 56. Analytical functions were then used to approximate the ion's energy-dependent elastic collision cross sections and resonant charge transfer with neutral species.

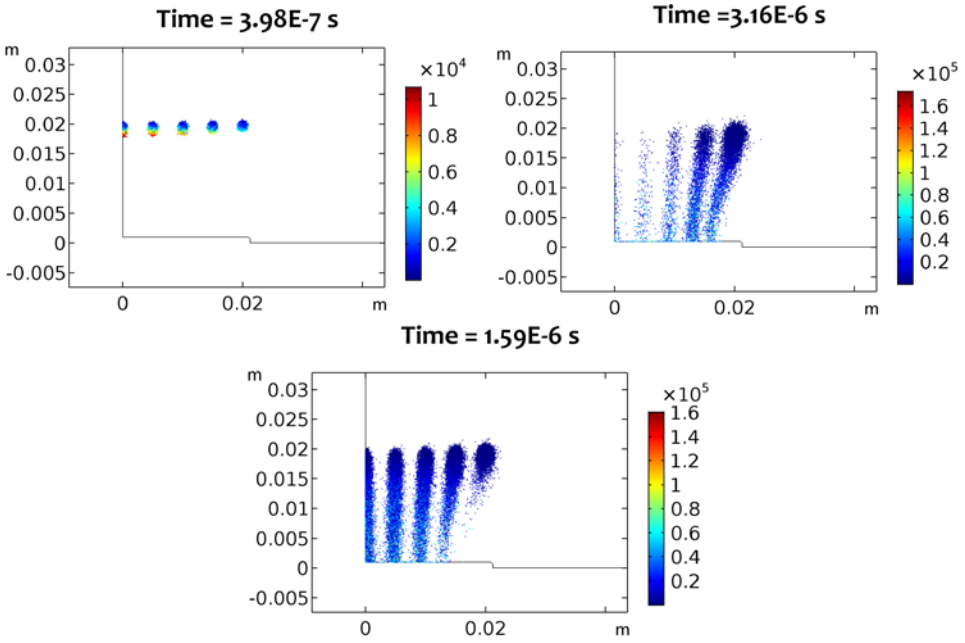

Figure 56. COMSOL particle trajectories at increasing times

The impact angle and incident energy are then combined to create a 2D histogram plot of the Ion Angular Energy Distribution Function (IAEDF) - Figure 57.

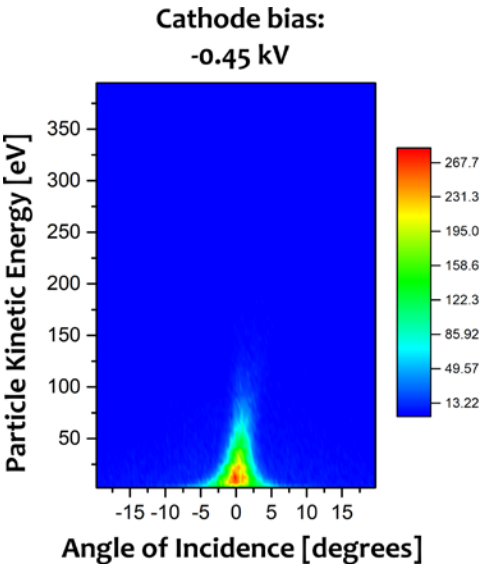

Figure 57. 2D IAEDF for 100 mTorr argon with a -0.45 kV cathode bias

There is a slight anisotropic trend in the angle of incidence which can be expected from looking at the particle trajectories in Figure 56 which correspond to following the largest gradient in electric potential, i.e. highest electric field. This distribution was then plotted as a 3D surface histogram for a different representation of the data - Figure 58.

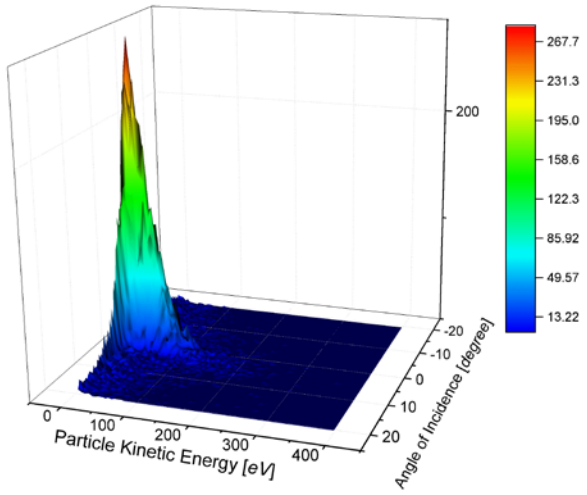

Figure 58. 3D IAEDF for 100 mTorr argon with a -0.45 kV cathode bias

Table 8 shows relevant quantities of the total number of particles that are incident on the cathode, the average particle kinetic energy, and the maximum particle kinetic energy.

Table 8. Total number of particles incident on cathode, average particle kinetic energy, maximum particle kinetic energy

Cathode bias [keV]	Total number of particles incident on cathode	Average Particle Kinetic Energy [eV]	Maximum Particle Kinetic Energy [eV]
−0.45	50,000	29.8	359

The Ion Energy Probability Function (IEPF) was then plotted on a logarithmic scale to investigate if the distribution was Maxwellian. This is shown in Figure 59, and it appeared to have two straight features corresponding to a bi-Maxwellian distribution. These were

then fitted with a linear function resulting in ion temperatures of 10 ± 0.9 eV and 51.9 ± 3.4 eV.

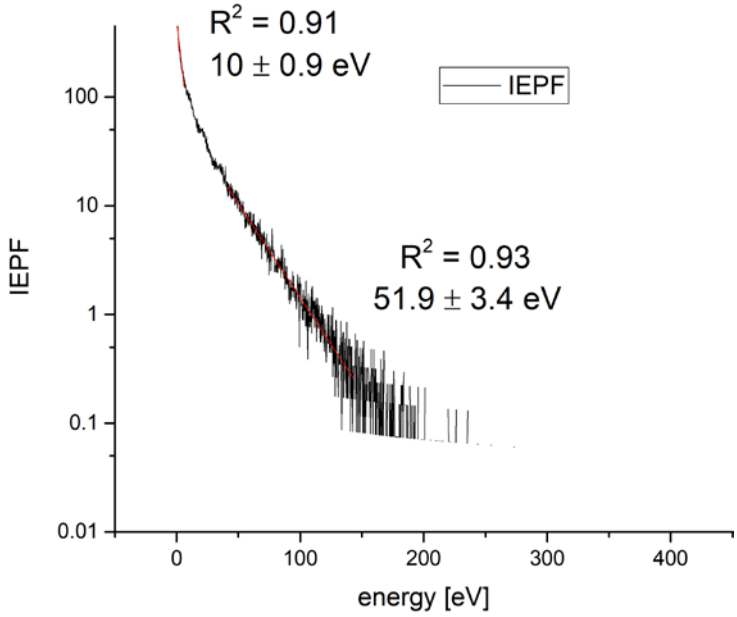

Figure 59. IEPF for 100 mTorr argon at -0.45 kV cathode bias

Given the model's reliability in lower pressures, it was then used to estimate the ion energies at higher cathode voltages and pressures. The pressure was increased to 392 mTorr, the same pressure as the deuterium ion bombardment conditions, and the biases of $-0.75\,\mathrm{kV}, -0.875\,\mathrm{kV},$ and $-1.0\,\mathrm{kV}$ were chosen. The same process of first finding the 2D IAEDF was done - Figure 60.

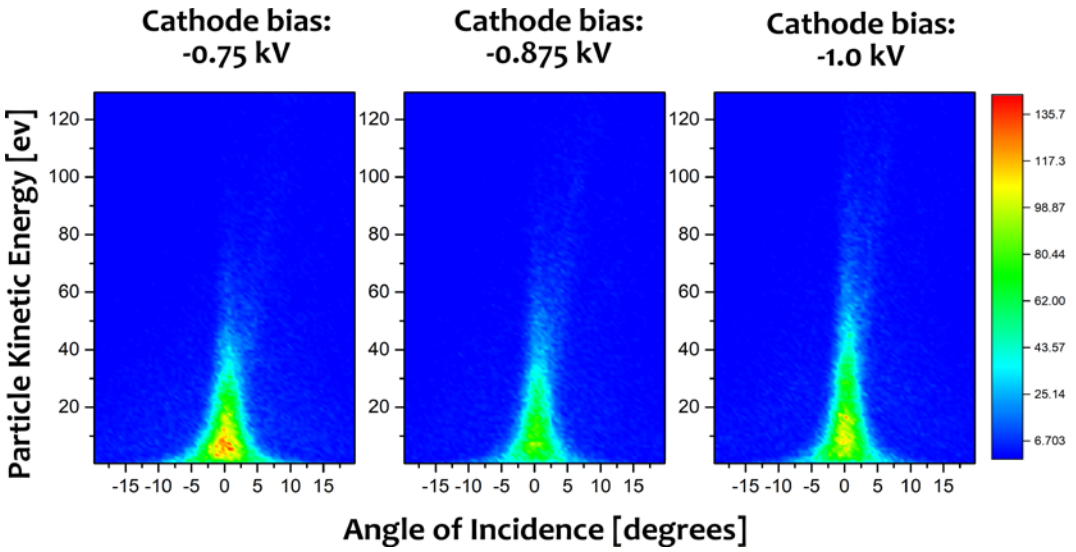

Figure 60. 2D IAEDF for 392 mTorr argon with varying cathode biases: -0.75 kV, -0.875 kV, and -1.0 kV

Followed by plotting the 3D IAEDF for the different perspective - Figure 61. However, a peculiarity was quickly apparent as seen in b) - large localized spikes in the IAEDF at high energies. The other cathode biases did not present such features at any energy levels.

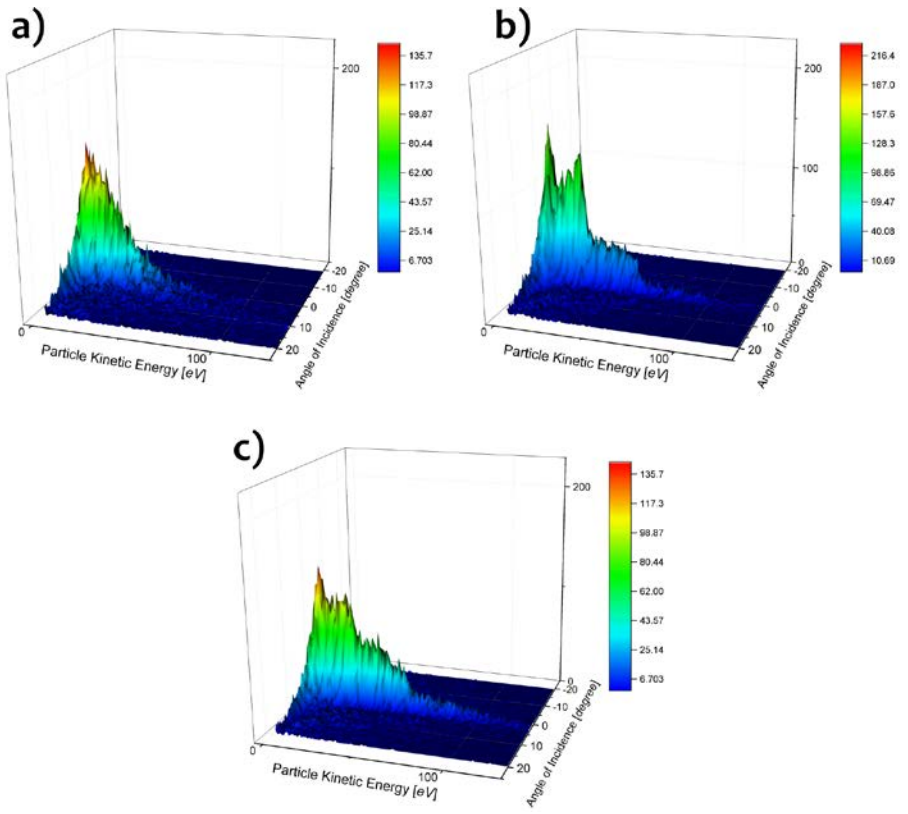

Figure 61. 3D IAEDF for 392 mTorr argon with cathode biases of (a) -0.75 kV (b) -0.875 kV and (c) -1.0 kV

The same statistics were found as for the −0.45 kV cathode bias - shown in Table 9.

Table 9. For 392 mTorr argon - total number of particles incident on the cathode, average kinetic energy, and maximum particle kinetic energy for multiple cathode voltages

Cathode bias [keV]	Total number of particles incident on cathode	Average Particle Kinetic Energy [eV]	Maximum Particle Kinetic Energy [eV]
−0.75	50000	24.4	736
−0.875	50000	21.3	951.1
−1.0	50000	25.2	921

This shows that for each voltage the average particle kinetic energy does not change significantly. The maximum particle kinetic energy does seem to be affected but seems to have an upper limit. A peculiarity is that the maximum particle kinetic energy for the -

0.875 kV cathode case has an energy that is higher in magnitude than the cathode voltage. It was assumed that the release gird for this case was placed in such a way that some of the particles' trajectories were affected by the high electric field at the cathode corner. The IEPFs were also found to gain estimates of the ion temperatures as a function of cathode bias. It was decided that the prior analysis assuming linear slopes could produce erroneous conclusions on determining that the distribution is bi-Maxwellian. However, it does present quantitative values for how the low energy and high energy ions are affected by the cathode bias. The lower energy ion linear fit window was kept between 0 to 5 eV while the high energy ion linear fit window was maintained between 50 to 150 eV. The results are shown on the next page in Figure 62.

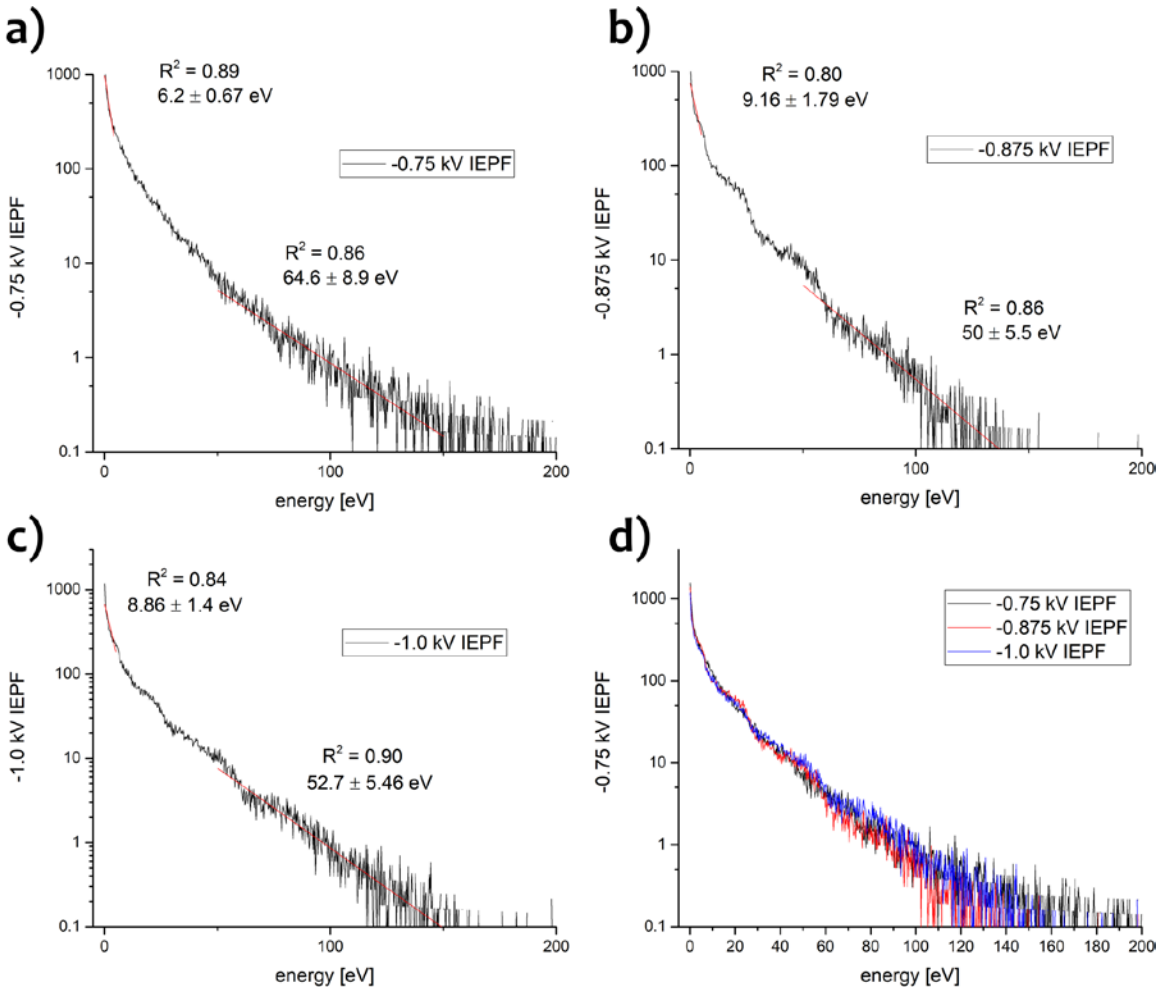

Figure 62. IEPF for 392 mTorr argon with cathode biases of (a) -0.75 kV (b) -0.875 kV and (c) -1.0 kV (d) superimposed plots

Table 10. Ion temperatures from linear fits on low and high energy windows for 392 mTorr argon with increasing cathode bias

Cathode bias [keV]	Low Energy Temperature from Linear Fit [eV]	High Energy Temperature from Linear Fit [eV]
-0.75	6.2 ± 0.67	64.6 ± 8.9
-0.875	9.16 ± 1.79	50 ± 5.5
-1.0	8.86 ± 1.4	52.7 ± 5.46

The 2D and 3D IAEDFs revealed how the electric potential affects the angle of incidence with a slight anisotropy resulting. An increased bias voltage was shown to increase the particle's maximum kinetic energy, albeit slightly as shown in Table 9, and also to decrease the angle of incidence. The majority of the particles have insufficient energy to cause sputtering or vacancy production. The IEPFs linear fit data showed little change with increasing cathode bias.

3.7.2 Deuterium COMSOL Simulation - Ion Angular Energy Distribution Functions

Since the COMSOL model for argon matched the Druyvesteyn method Langmuir probe results so well, it was believed that the fundamental procedure of the simulation was sound and that it was worthy to investigate using deuterium for incident ion energy estimates. To accurately model hydrogen discharges, it is essential to use proper reaction schemes that take into account the various ion and excited species being created. This quickly gets drastically more complex than the argon simulation as argon only has a single excited and ionic species relevant to discharges at these parameters. On the other hand, hydrogen has excited species for H, H_2, and H_3^+. An analysis of the minimum reaction set that plays the dominant role in the simulation was not enacted and instead studies on simulating hydrogen DC discharges were consulted and slightly expanded: Liu and Zhang's [56] and Kimura and Kasugai's [57].

There were five types of reactions relevant to the simulations: elastic, excitation, superelastic (de-excitation), ionization, and attachment. Kimura and Kasugai present the used rate coefficients for the reaction set, but it is significant to take note that they were simulating a hydrogen discharge opposed to a deuterium discharge. Hydrogen and its isotopes while having identical potential energy curves present different dynamics and thermodynamic properties resulting from the different vibrational and rotational energy levels. This emerges as altered dissociation energy for the molecules and their excited

states. In order to account for this, the comprehensive study done by Yoon et al. [58] was consulted which compiled electron-impact cross-section data for HD and D_2 molecules according to a strict set of criteria for well-validated data. Lastly, production rates for D_3^+ and cross-section data for ion-ion and ion-neutral were found in Janev et al.'s report on collision processes in low-temperature hydrogen plasmas [59]. Error! Reference source not found. in Appendix section A4 lists the relevant reactions used and their corresponding electron energy loss. It is noted that the table does not show the de-excitation reactions to conserve space and that the excitation to de-excitation cross sections were calculated using the ratio of statistical weights of the form

$$g_k = 2\,n_k^2 \tag{1.15}$$

where g is the statistical weight for the for the species k and n is the corresponding principal quantum number. It was assumed that the secondary electron emission coefficient was similar to that of helium on nickel which for 100 eV ions produced a $\gamma_{se} = 0.17$.

The model procedure was followed, first computing the coupled Plasma-Boltzmann modules which produced electron densities, temperatures, EEDFs, etc. However, for this section, only the final electric potential was of interest as an input parameter for the Particle Tracing Module. Interpolated particle-particle interaction functions were used for this section coming from [59] for $D_2^+ + D_2$ elastic, inelastic, and resonant charge transfer cross sections. The resulting 2D IAEDF are plotted below:

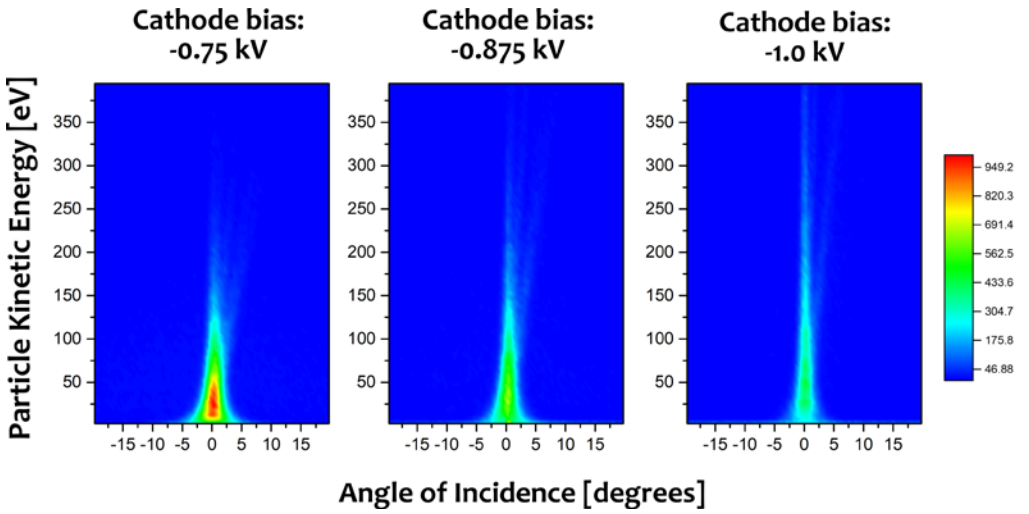

Figure 63. 2D IAEDF for 392 mTorr deuterium with varying biases: -0.75 kV, -0.875 kV, and -1.0 kV

These show an IAEDF that is significantly more affected by the cathode bias resulting in higher energies and a narrowing of the angle of incidence window. The 3D IAEDF are also plotted along with analyses for the particle statistics in Figure 64 and Table 11. The particle average kinetic energy and maximum kinetic energy shows a clear and direct dependence on the cathode voltage.

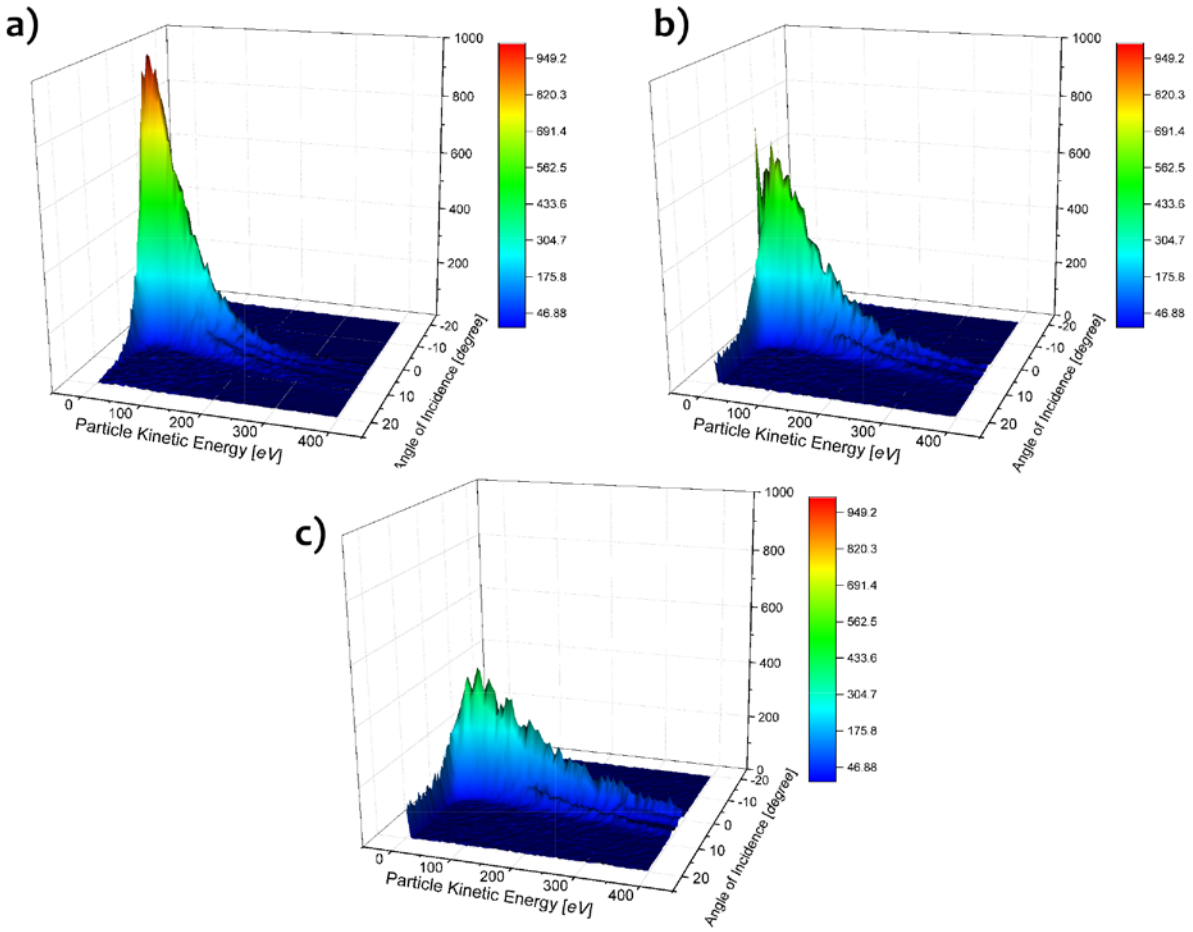

Figure 64. 3D IAEDF for 392 mTorr deuterium with cathode biases of (a) -0.75 kV (b) -0.875 kV and (c) -1.0 kV

Table 11. For 392 mTorr deuterium - total number of particles incident on the cathode, average kinetic energy, and maximum particle kinetic energy for multiple cathode voltages

Cathode bias [keV]	Total number of particles incident on cathode	Average Particle Kinetic Energy [eV]	Maximum Particle Kinetic Energy [eV]
−0.75	50000	72.3	734.8
−0.875	48682	104.5	841.1
−1.0	50000	160.3	988.2

These show a more direct relationship between particle kinetic energy and cathode bias than the results from the argon simulations with both the average and maximum kinetic

energies increasing with voltage. The 3D IAEDF show distributions that at least appear to be more Maxwellian than those obtained for the argon simulations. The IEPFs were plotted again to prove this - Figure 65. The windows of analyses were the same as the argon study: 0-5 eV and 50-150 eV. Table 12 shows the results. For deuterium, this IEPF analysis resulted in a strong direct relationship to the cathode voltage for the low and high energy linear fits. Figure 65 d) is particularly useful in visualizing the decreasing slopes which correspond to the increased ion temperatures.

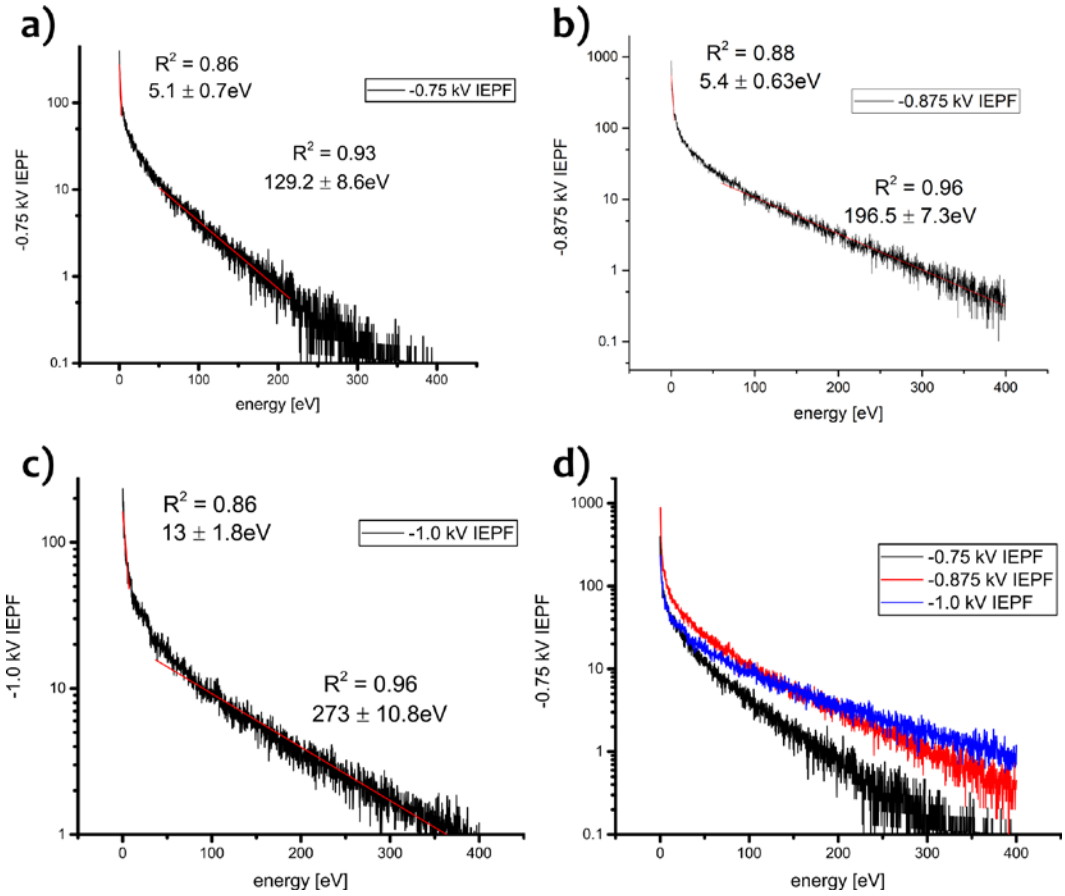

Figure 65. IEPF for 392 mTorr deuterium with cathode biases of (a) -0.75 kV (b) -0.875 kV (c) -1.0 kV (d) superimposed plots

Table 12. Ion temperatures from linear fits on low and high energy windows for 392 mTorr deuterium with increasing cathode bias

Cathode bias [keV]	Low Energy Temperature from Linear Fit [eV]	High Energy Temperature from Linear Fit [eV]
-0.75	5.1 ± 0.7	129.2 ± 8.6
-0.875	5.4 ± 0.6	196.5 ± 7.3
-1.0	13 ± 1.8	273 ± 10.8

The same model was then used at lower pressures in an attempt to increase the incident ion energies. The 2D and 3D IAEDFs - Figure 66 and Figure 67 respectively - compared to those of the 392 mTorr D_2 simulation show a slight increase in the angle of incidence with higher energy ions having a larger spread in angle. They also show how the distribution contains an increased concentration of high energy ions.

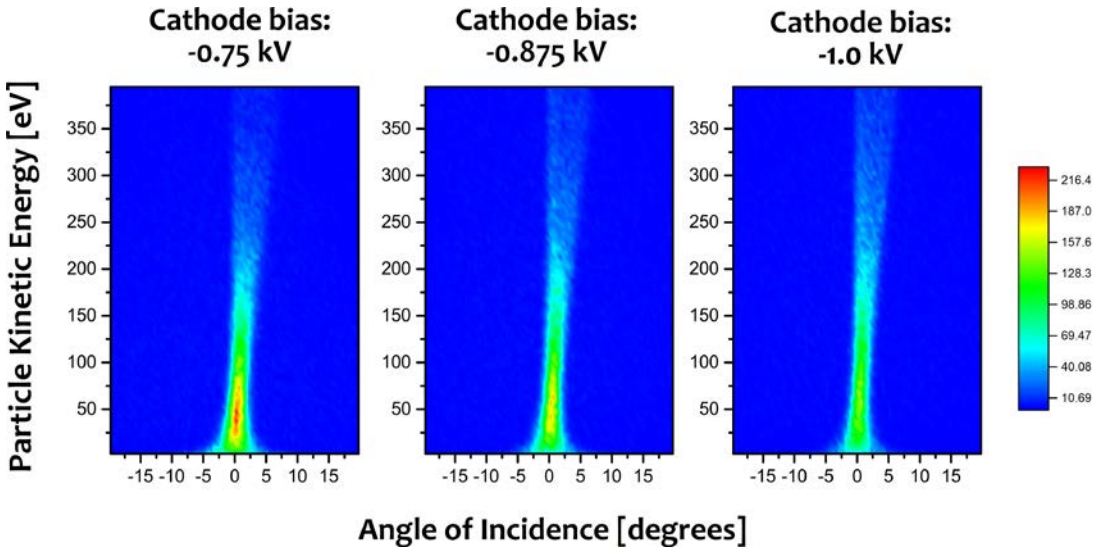

Figure 66. 2D IAEDF for 85 mTorr deuterium with varying cathode biases: -0.75 kV, -0.875 kV, and -1.0 kV

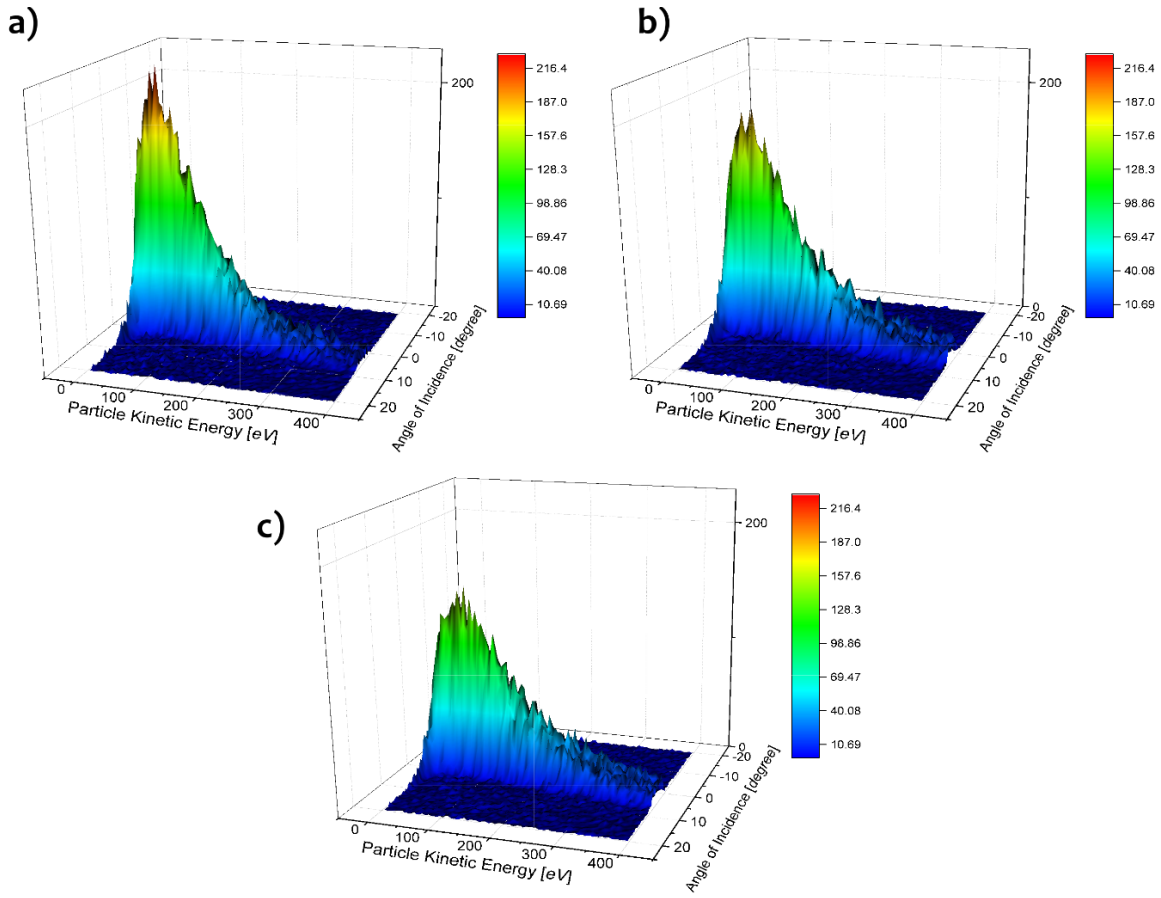

Figure 67. 3D IAEDF for 85 mTorr deuterium with cathode biases of (a) -0.75 kV (b) -0.875 kV and (c) -1.0 kV

The statistics for the particles was also found, shown in Table 13. The average particle kinetic energy and maximum particle kinetic energies again show a linear relationship with cathode voltage, but they have increased magnitudes than the 392 mTorr study. Which is expected since the ions have a larger mean free path.

Table 13. For 85 mTorr deuterium - total number of particles incident on the cathode, average kinetic energy, and maximum particle kinetic energy for multiple cathode voltages

Cathode bias [keV]	Total number of particles incident on cathode	Average Particle Kinetic Energy [eV]	Maximum Particle Kinetic Energy [eV]
−0.75	50000	139.3	718.9
−0.875	50000	179.42	862.1
−1.0	50000	288.42	1005.2

The IEPFs were finally investigated, and they also showed the two linear sections - Figure 68. These were analyzed with the same window settings as before, and the results are in Table 14. It again shows the direct relationship to the cathode voltage for the low and high energy ion temperatures.

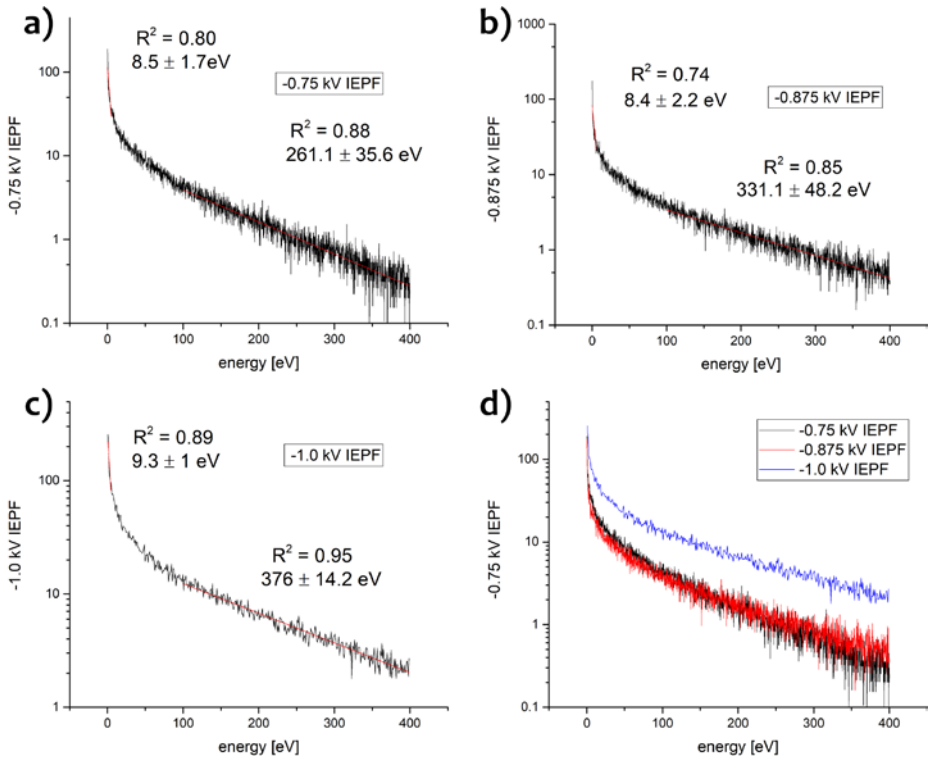

Figure 68. IEPF for 85 mTorr deuterium with cathode biases of (a) -0.75 kV (b) -0.875 kV (c) -1.0 kV and (d) superimposed plots

Table 14. Ion temperatures from linear fits on low and high energy windows for 85 mTorr deuterium with increasing cathode bias

Cathode bias [keV]	Low Energy Temperature from Linear Fit [eV]	High Energy Temperature from Linear Fit [eV]
-0.75	8.5 ± 1.7	261.1 ± 35.6
-0.875	8.4 ± 2.2	331.1 ± 48.2
-1.0	9.3 ± 1	376 ± 14.2

Chapter 4: Ion Bombardment and Thermal Desorption Spectroscopy

4.1 Background

The thermal desorption spectroscopy method was used to investigate any binding sites for deuterium after plasma ion bombardment. Since the temperatures required to desorb the high binding energy sites are outside of the operational parameters for the vacuum heater, the samples were brought to a different vacuum furnace for TDS. The apparatus diagram is below in Figure 69. It consists of a quartz tube that is surrounded by an insulated furnace. The system is capable of obtaining vacuums on the $10^{-7} - 10^{-8}$ Torr range which generally would not be low enough for hydrogen mass spectroscopy, but the background signal for deuterium partial pressure is on the scale of 10^{-10}. The high mass two signal (H_2) limits the system to only producing spectra for mass 4 (D_2) which neglects the desorption contribution from monatomic D.

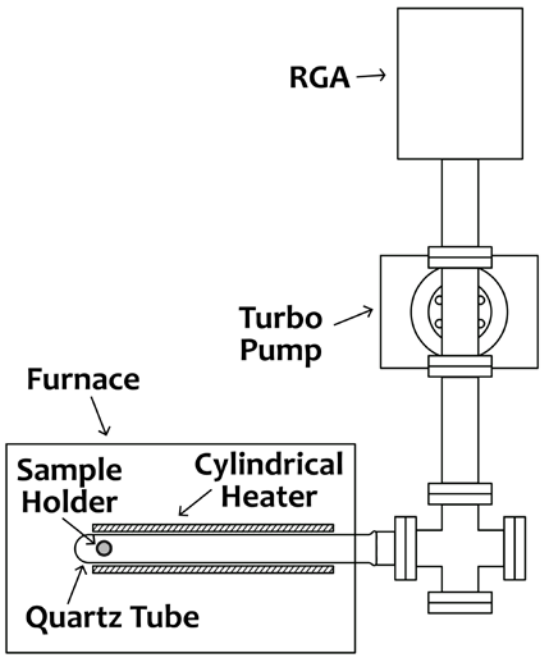

Figure 69. TDS apparatus diagram

The radial temperature profile for the TDS system was checked as it went through constant ramp rates to 1000℃. An internal thermocouple inside of the quartz tube at the point where the sample would rest along with a thermocouple on the outside of the quartz tube at the position of the sample holder measured the temperature as the ramp proceeded. This was done to have direct temperature measurements of the sample for reference as it went through various ramp rates. The internal thermocouple that was in contact with the sample was prohibitive for the system to reach its ultimate vacuum readings and instead stabilized at 10^{-6} Torr which is too high of a background pressure to do accurate TDS. The differences in pressures were deemed to have insignificant effects on the sample temperature. The thermocouple on the outside of the quartz tube always remained and acted as the temperature control point for the PID system. For every TDS test, the outside thermocouple's temperature profile was compared to the reference profiles to ensure the sample temperature was consistent; an example is shown

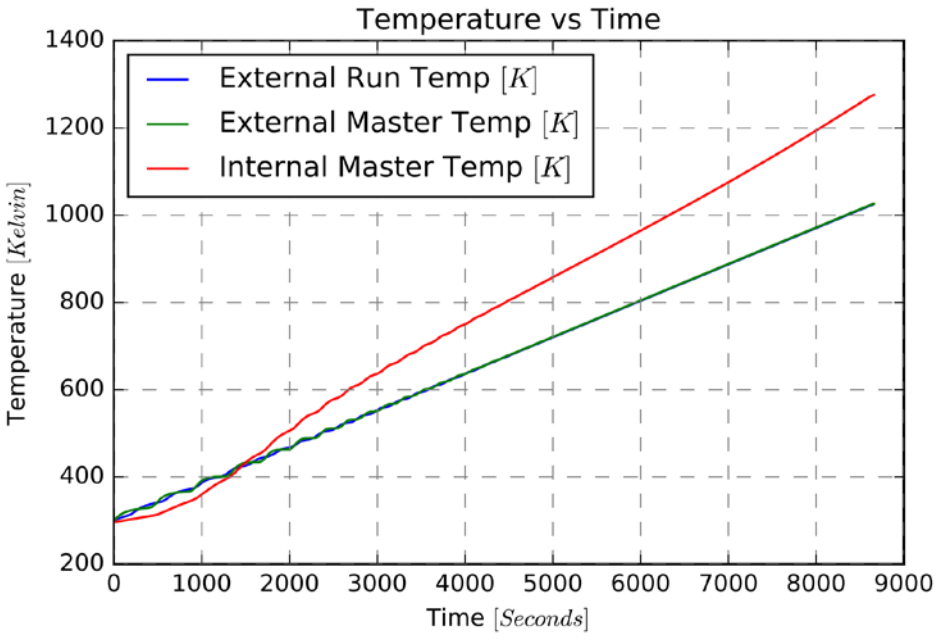

Figure 70. TDS comparison between a given test's external temperature on the quartz tube to that of a reference to ensure the ramp rates are consistent

4.2 Plasma Treatment Conditions

The pressure for the plasma bombardment was 392 mTorr as it allowed to quickly get to the desired fluences without having to consider appreciable leak concentrations. The conditions tested were previously shown in Figure 20. The studies consisted of three ion fluences - $1\,x\,10^{18}\text{ions/cm}^3$, $1\,\text{x}\,10^{19}\text{ions/cm}^3$, and $1\,\text{x}\,10^{20}\text{ions/cm}^3$ - with three cathode voltages - $-0.75\,\text{kV}$, $-0.875\,\text{kV}$, and $-1.0\,\text{kV}$ - at two pressures - 392 mTorr and 1 Torr. The plasma chamber is capable of treating three samples at a time, which is vital to keep the conditions as constant as possible for each as the fluence is increased. It was unfortunate that a third pressure could not be tested due to the TDS apparatus having operational difficulties due to leaks, PID controller issues, and utilizing the system for other projects. The Pd foils were purchased from Lebow Company, and all had thicknesses of $8\,\mu\text{m}$.

4.3 TDS Results

After plasma treating the Pd foils at varying fluences at a given voltage and pressure, they were brought to the TDS apparatus. The sites of interest have binding energies that are not overcome until high temperatures $> 325℃$, hence the trapped deuterium will not desorb at atmospheric conditions. There will be surface adsorbates, but these are desorbed from baking the samples in the TDS system at $200℃$ for 2-3 hours before each TDS test. For each sample dataset, the partial pressures of the species in Table 15 were recorded and compared to a background dataset of an empty TDS quartz tube to ensure conditions. An example of the background comparison for a sample treated at $-1.0\,\text{kV}$ and 392 mTorr for a fluence of $1\,\text{x}\,10^{18}\text{ions/cm}^2$ is shown Figure 71 and Figure 72 for argon and deuterium respectively. The argon background pressure stays between

6×10^{-10} and 1×10^{-9} Torr while the deuterium background pressure is between 5×10^{-10} to 7×10^{-10} Torr.

Table 15. RGA gas species

Gas Species	Species Mass [amu]
H	1
H_2, D	2
HD	3
D_2	4
H_2O	18
N_2	28
O_2	32
Ar	40

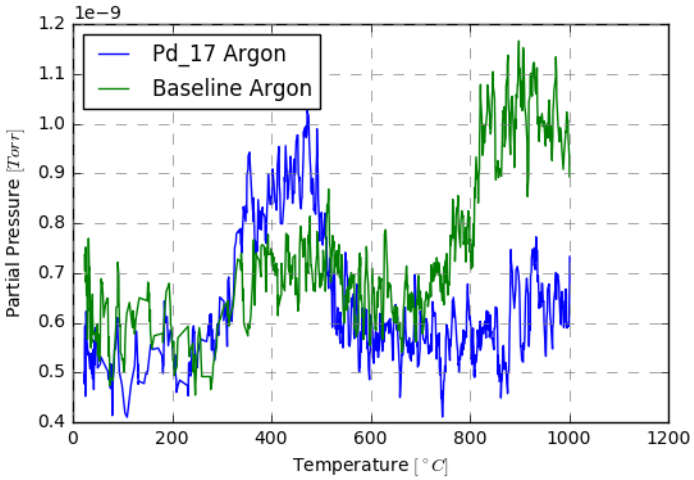

Figure 71. Argon partial pressure for a plasma treated Pd sample compared to the baseline argon pressure - -1.0 kV and 392 mTorr for a fluence of 1×10^{18} ions/cm^2

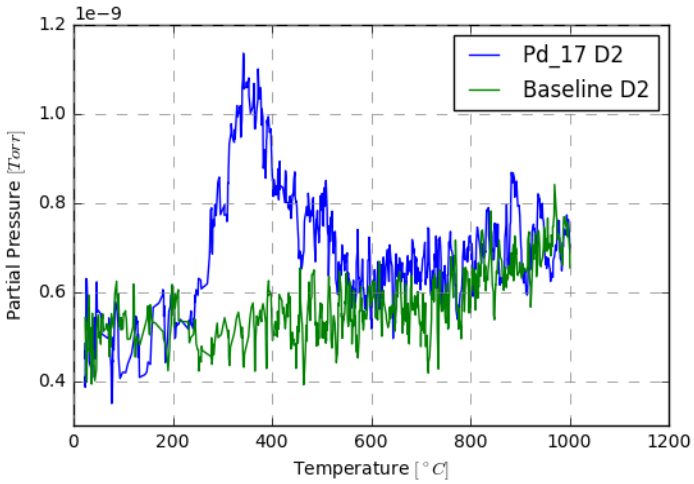

Figure 72. Deuterium partial pressure for a plasma treated Pd sample compared to the baseline deuterium pressure - -1.0 kV and 392 mTorr for a fluence of 1×10^{18} ions/cm^2

The resulting data is shown in groups of constant fluence varying voltage and constant voltage varying fluence. The data for the 0.392 Torr and 1.0 Torr conditions are plotted together for the constant fluence figures and plotted separately for the constant voltage figures. The results for the constant fluences with the varying cathode voltages plotted are shown in Figure 73, Figure 74, and Figure 75 for 1×10^{18} ions/cm^2, 1×10^{19} ions/cm^2, and 1×10^{20} ions/cm^2 respectively. Each dataset produced desorption curves in the $600 - 800\ K$ range.

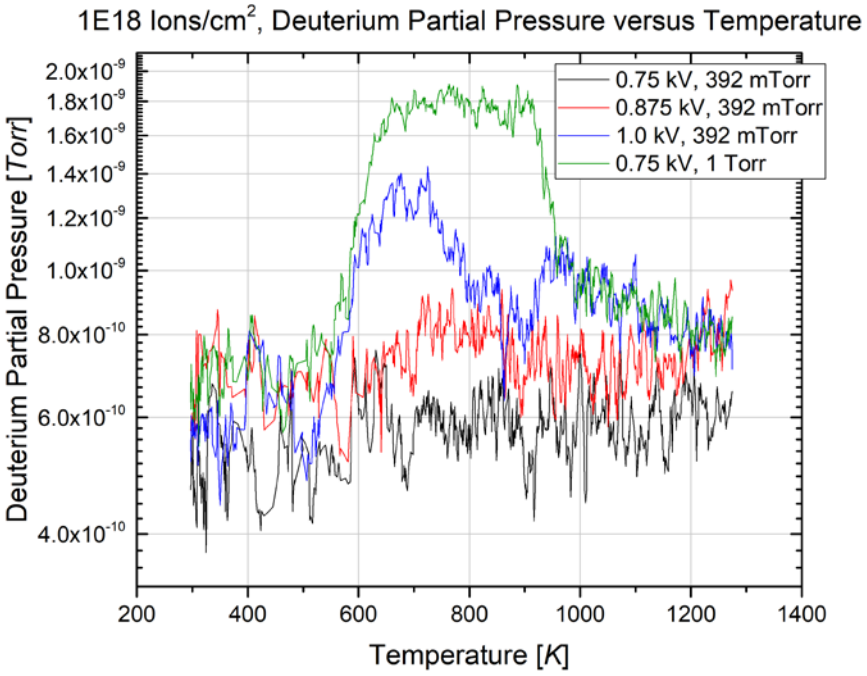

Figure 73. TDS for 1×10^{18} ions/cm^2 fluence

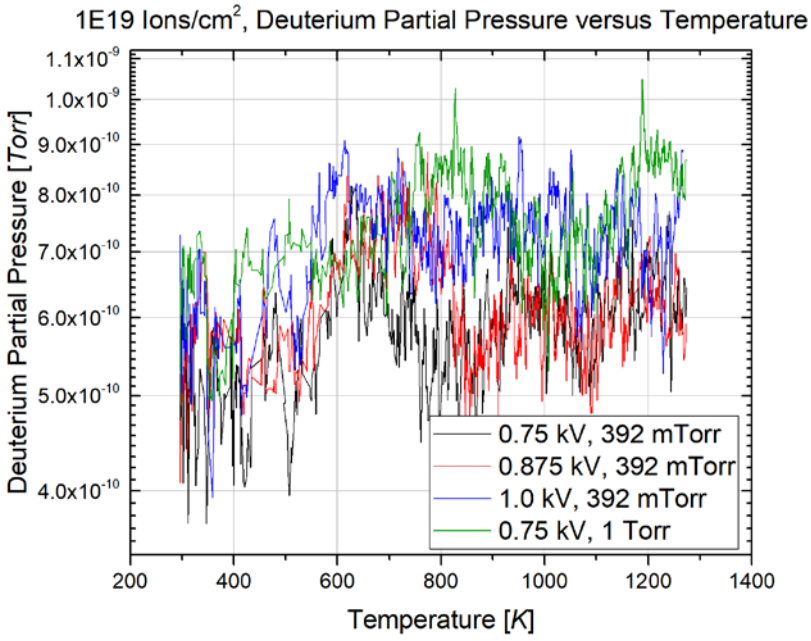

Figure 74. TDS for 1×10^{19} ions/cm^2 fluence

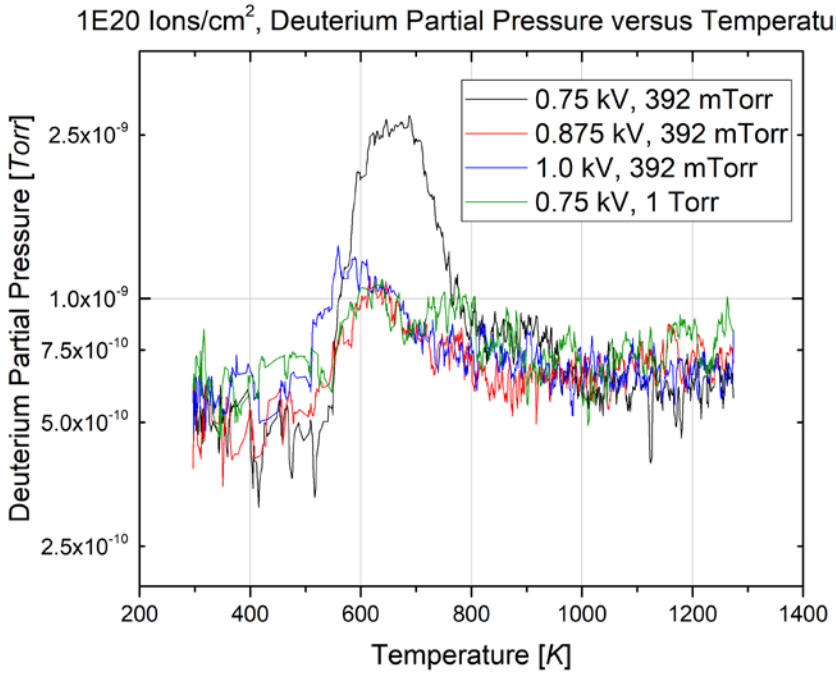

Figure 75. TDS for 1×10^{20} ions/cm^2 fluence

For 1×10^{18}ions/cm^2, and to a lesser extent 1×10^{19}ions/cm^2 fluences, increasing the cathode voltage led to an increase in trapped deuterium with similar desorption temperatures. The higher pressure conditions led to the maximum trapped deuterium. Figure 74 is obfuscated from each data peak not having a significant amount of trapped deuterium above background. The 1×10^{20}ions/cm^2 fluence shows a reversed trend: increasing cathode voltage led to a decrease in trapping conditions and the 1 Torr dataset no longer contains the most trapped deuterium. The results portraying constant cathode voltages and varying fluences are shown in Figure 76, Figure 77, Figure 78, and Figure 79 below.

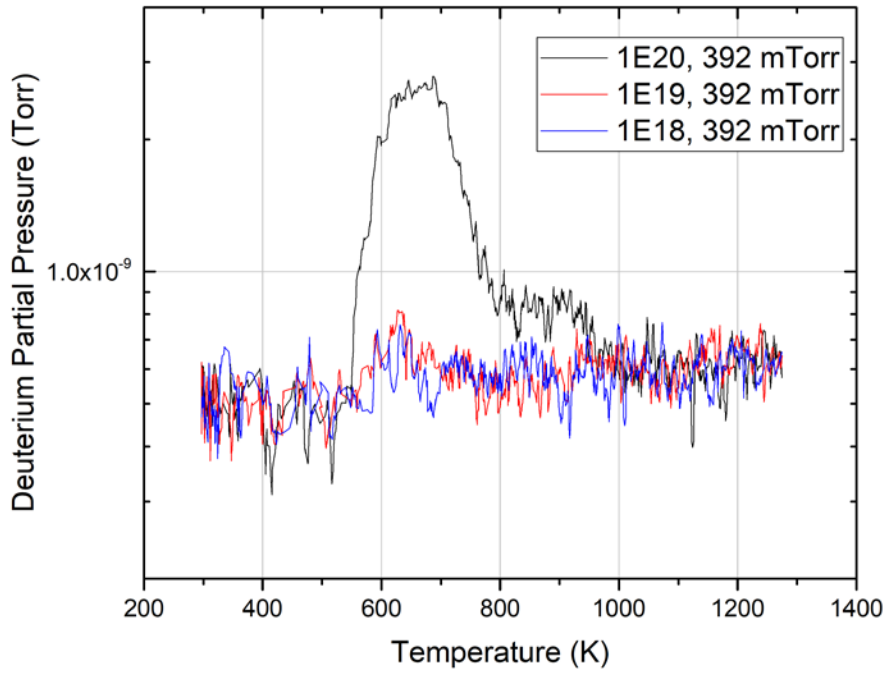

Figure 76. TDS for -0.75 kV cathode bias for 392 mTorr deuterium

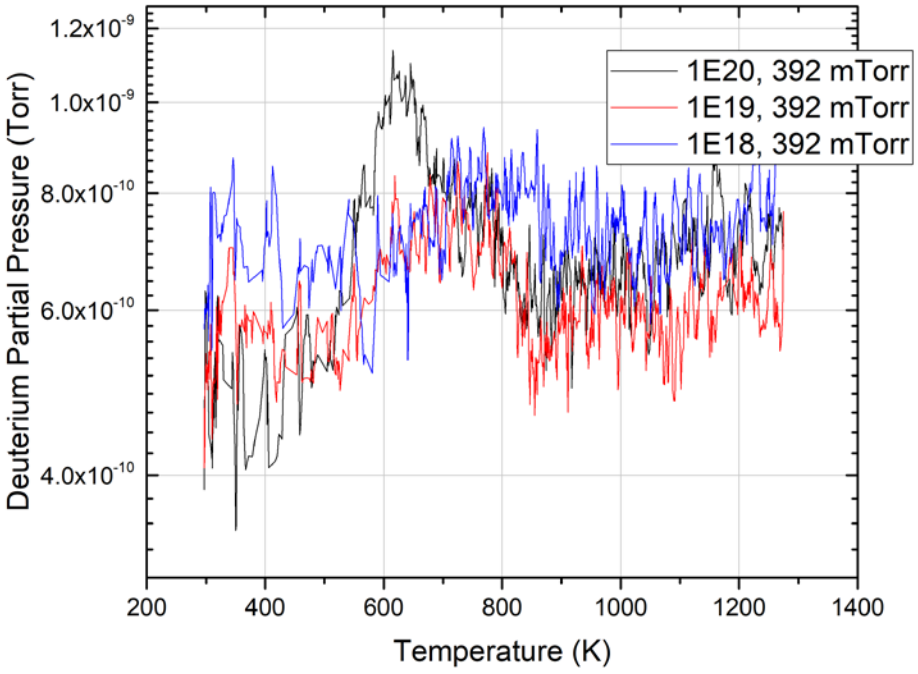

Figure 77. TDS for -0.875 kV cathode bias for 392 mTorr deuterium

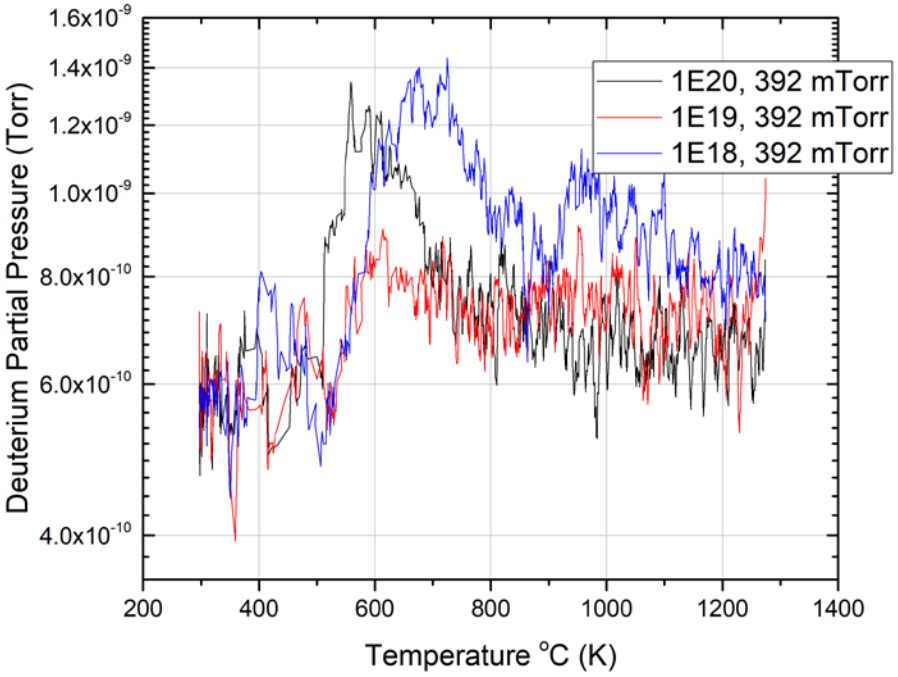

Figure 78. TDS for -1.0 kV cathode bias for 392 mTorr deuterium

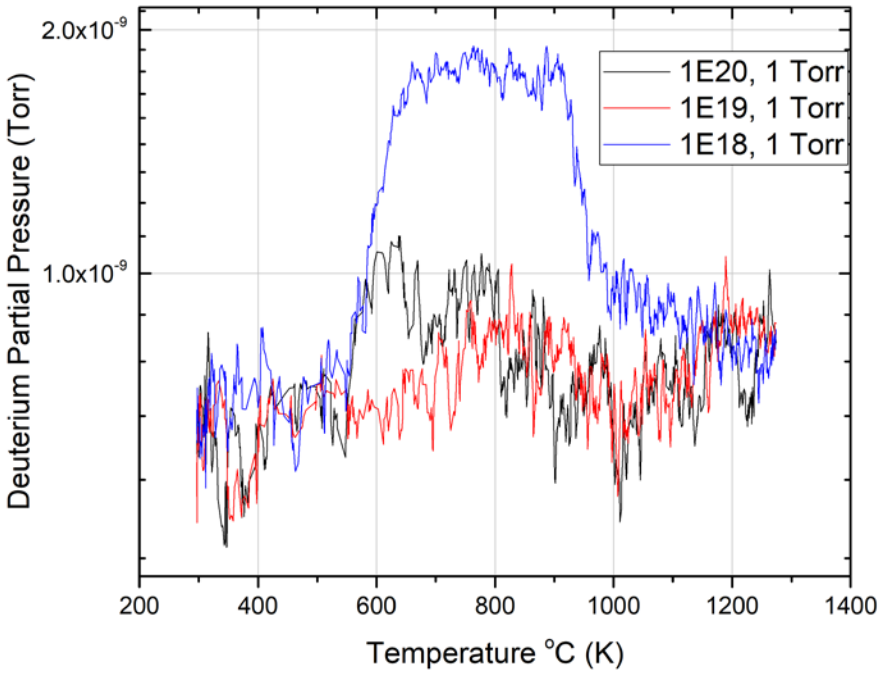

Figure 79. TDS for -1.0 kV cathode bias for 1.0 Torr deuterium

At 392 mTorr and for −0.75 kV, Figure 76, there is a strong direct relationship between fluence and trapped deuterium, i.e. as more ions interact with the sample more deuterium

is trapped. For $-0.875\,\text{kV}$, Figure 77, there is still a direct relationship between fluence and trapped deuterium, but it is significantly less pronounced. As the voltage is increased to $-1.0\,\text{kV}$, Figure 78, there seems to be a weakly inverse relationship with increasing fluence leading to less or roughly constant trapped deuterium. Lastly at $1.0\,\text{Torr}$ and $-0.75\,\text{kV}$, Figure 79, there is a strong inverse relationship between fluence and trapped deuterium.

4.4 Surface Morphology Progression

To investigate the possible morphological causes of these results some of the samples were observed under SEM and TEM with cross sections being performed using FIB. The as-received palladium foil images are in Figure 80 with (a) showing the surface at 3,500 magnification (3.5 kx) and (b) a cross-section at 25,000 (25 kx) magnification. The as-received surface shows no drastic features other than parallel lines running across it from the fabrication method, and the cross-section showed grain structures, but no signs of larger defects such as voids.

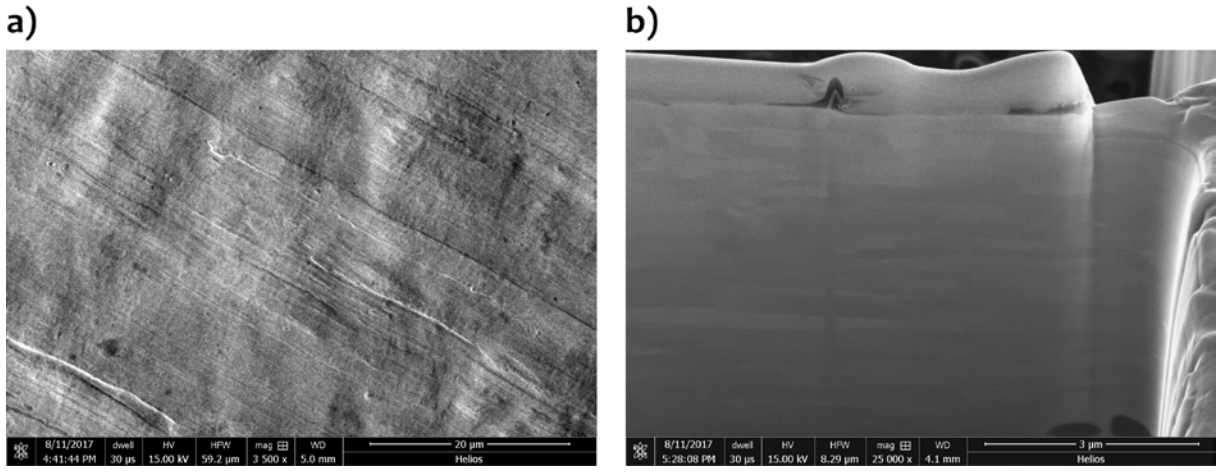

Figure 80. As received $8\,\mu\text{m}$ Pd foil from Lebow Company - (a) surface (3.5 kx) (b) cross section (25 kx)

Figure 81 and Figure 82 respectively show the surface morphology for $1\,\text{x}\,10^{19}\text{ions/cm}^3$ and $1\,\text{x}\,10^{20}\text{ions/cm}^3$ at $-1.0\,\text{kV}$ and $392\,\text{mTorr}$ for varying magnifications. With

increasing fluence there appeared to be more circular surface defects while the short tendril-like growths in Figure 80 (c) were not present.

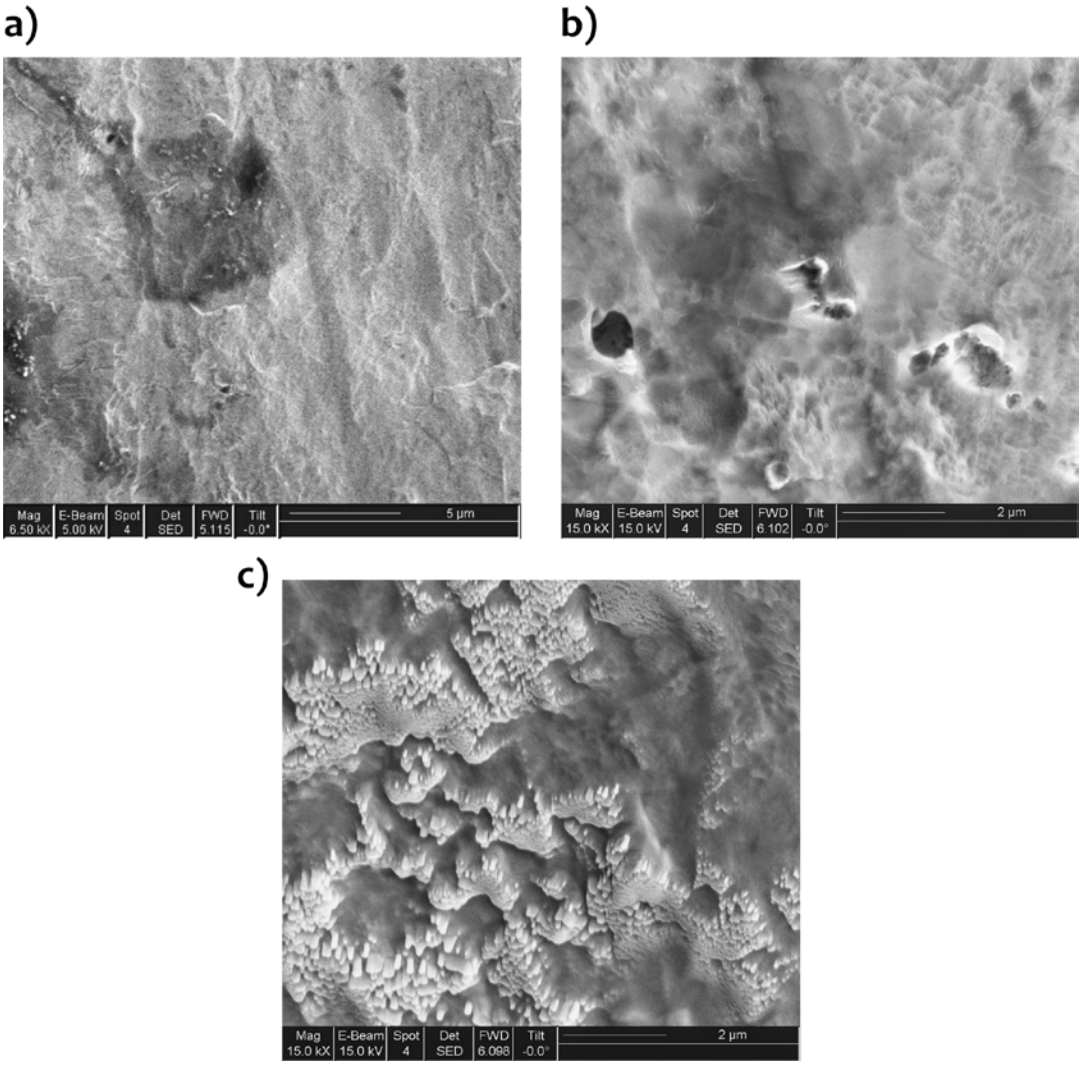

Figure 81. Surface morphology for $1 \times 10^{19} \text{ions/cm}^3$ at -1.0 kV and 392 mTorr - (a) 6.5 kx (b) 15 kx (c) 15 kx

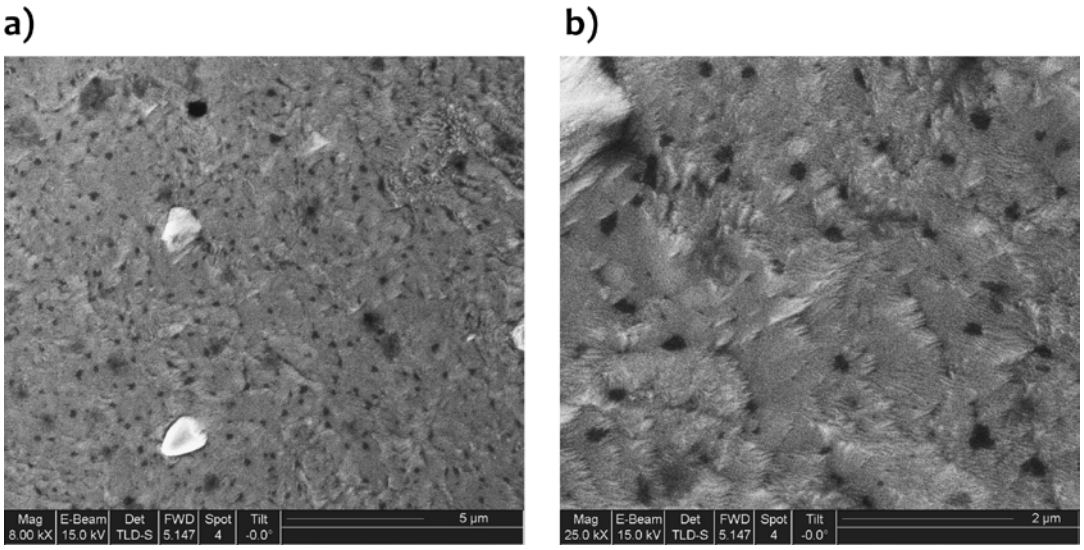

Figure 82. Surface morphology for $1 \times 10^{20} \text{ions/cm}^3$ at -1.0 kV and 392 mTorr - (a) 8 kx (b) 25 kx

The following SEM and TEM images are of a sample that was treated for $1 \times 10^{20} \text{ions/cm}^3$ at -1.0 kV and 1 Torr but was not subsequently used for TDS. However, it did produce the clearest SEM images. Figure 83 displays the surface morphology which appears to have highly irregular swelled blisters and crater formations with diameters $\sim 1\ \mu m$ as seen in (a). (b) and (c) are increased magnifications at the red circled section in (a) and they show further crater and hole formations with diameters on the order of $\sim 10\ nm$.

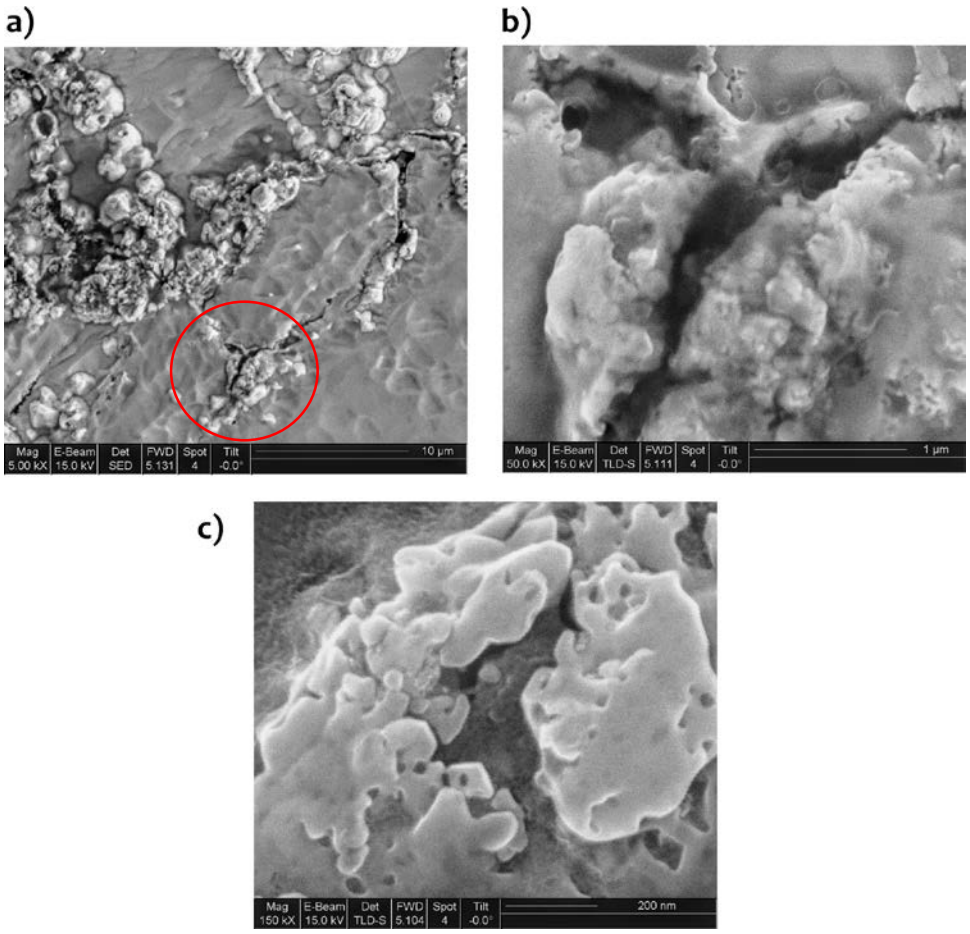

Figure 83. Surface morphology for $1 \times 10^{20} \text{ions/cm}^3$ at -1.0 kV and 1.0 mTorr - (a) 5.0 kx (b) 50 kx (c) 150 kx

Figure 84 shows the cross sections of this sample beneath the blister and crater surface formations. (a) and (b) are from a cross-section that was previously coated with a thin Pt coating to protect the surface features, while (c) and (d) forwent this step in an attempt to get more surface definition for context. (a) shows signs of subsurface voids at the darker colored grain boundaries. (b) shows crack formations. (d) is an enhancement of the red circle in (c) and it shows holes being formed between $200 - 300\,nm$ beneath the surface. All four images show signs of vertical grains.

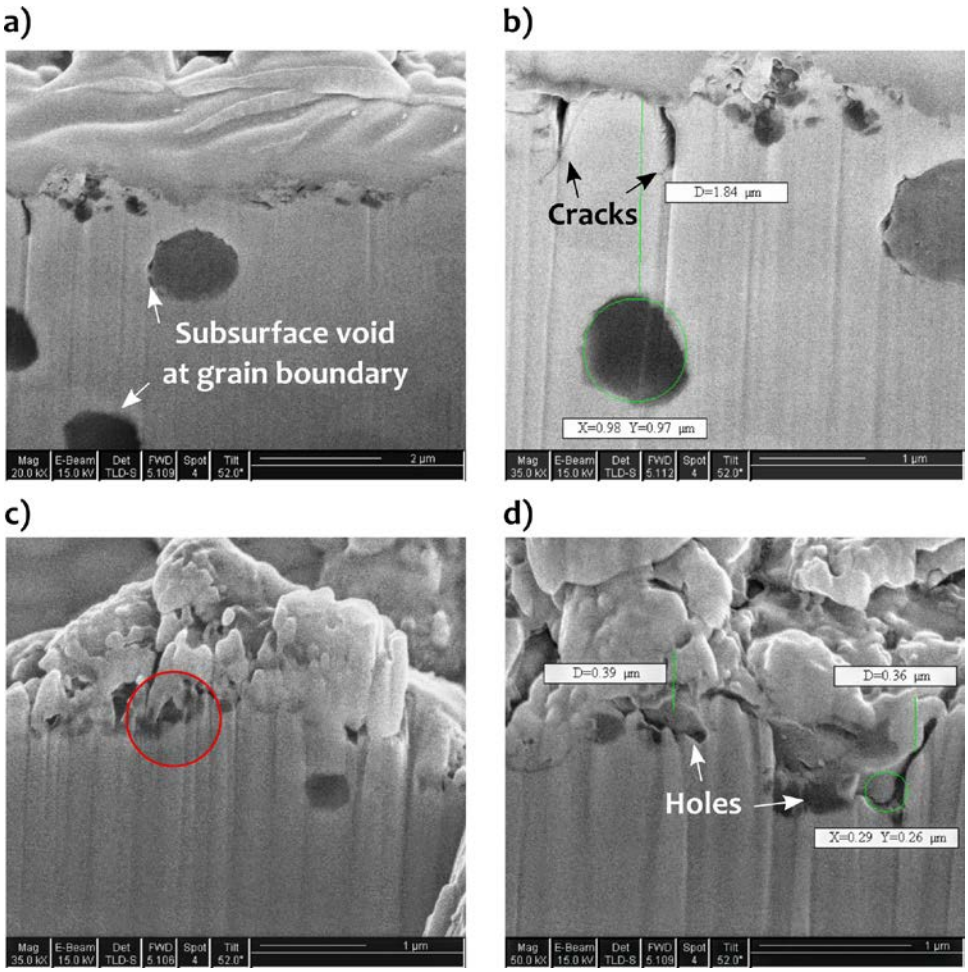

Figure 84. Cross sections for $1 \times 10^{20} ions/cm^3$ at -1.0 kV and 1.0 mTorr - (a) 20 kx (b) 35 kx (c) 35 kx (d) 50 kx

Figure 85 shows TEM images of the sample that was treated with $1 \times 10^{20} ions/cm^3$ at -1.0 kV and 1 Torr. It displays damage cascades propagating ~350 nm beneath the surface. (c) is the enhanced image of the red circle in (a) and the same for (d) with the red circle in (b).

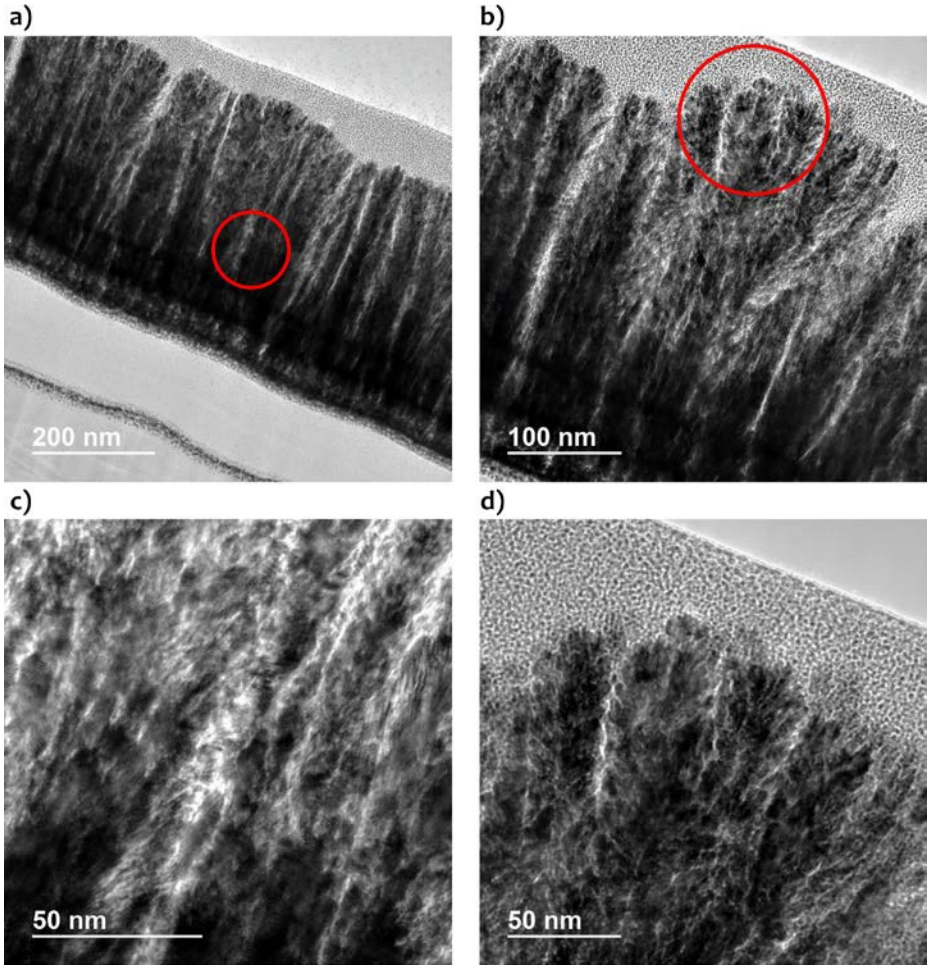

Figure 85. TEM images for 1×10^{20} ions/cm^3 at -1.0 kV and 1.0 mTorr - (c) corresponds with the circled section in (a) and (d) corresponds with the circled section in (b)

With these SEM and TEM images, it is apparent that the plasma treatments do indeed produce subsurface damage characteristic features such as holes, voids, grain boundaries, etc. These surface morphology changes not only increase the surface area of the material but also create more sites that have lower activation energies for the absorption of deuterium. While cross-section and TEM images were only obtained for one set of treatment parameters, it is possible in combination with the COMSOL ion energy data and SRIM to infer the features from other plasma treatments. Such as, with increasing cathode voltage and decreasing pressures comes higher penetration into the material and damage cascades similar to Figure 85 propagating further into the bulk.

CHAPTER 5: CONCLUSION AND FUTURE WORK

5.1 Conclusions

The hydrogen-metal interaction stands as one of the most studied solute-solvent systems. However, questions remain on how hydrogen is affected by defects and how best to model these interactions. This gets further convoluted when coupled to the dynamic effects of ion bombardment resulting in a rich interplay of coinciding effects: athermal ion interactions, non-equilibrium hydrogen concentrations, and local thermodynamic properties. Incident ions produce damage cascades that lead to hydrogen trapping defects. Occupied defects go on to yield strain in the material lowering the activation barrier for further damage - resulting in even more trapped deuterium. However, as this work shows there seems to be a damage concentration limit that once passed, additional interaction with ions is counterproductive to deuterium retention at high binding energy sites.

Utilizing the Druyvesteyn method for Langmuir probe analysis, EEDFs and their corresponding electron densities and temperatures were found as a function of position from the cathode. The review was relegated to argon at 100 mTorr as it is necessary for the plasma to be in a collisionless regime for the Druyvesteyn method to be applicable and the current apparatus was not capable of producing a deuterium plasma that met these conditions. The electron density showed an increase as the probe distance to the cathode decreased until reaching a maximum of $1.85 \pm 0.42\ x\ 10^{15}\mathrm{m}^{-3}$ at 35 mm and then decreased as it neared the plasma sheath. The electron temperature showed a general trend of increasing as the probe approached the cathode towards a maximum of 1.53 ± 0.15 eV at 25

mm. The EEDFs displayed more Druyvesteyn-like characteristics at the higher electron density middle region and more Maxwellian-like characteristics at the low-density edges. The trends of the electron densities and temperatures were also apparent in the EEDFs: higher densities correlated to a more elevated magnitude in the EEDF and higher temperatures connected to higher energy tails.

The estimation of incident ion energies on the Pd cathode began with COMSOL simulations. Since the Langmuir probe EEDFs were found in a 100 mTorr argon plasma, that was the benchmark. The argon plasma chemistry is relatively simple and straightforward consisting of seven reactions. The difficulty came in estimating EEDFs as a function of position from the cathode. To do this the Plasma Module was coupled to the Boltzmann Equation, Two-Term Approximation Module which fed input parameters to one another, e.g. electron transport properties and electron temperature and density, until a convergent solution was found. The resulting EEDFs as a function of position matched well with the Langmuir probe measurements showing the same trends: electron density increasing to a maximum and then decreasing and the electron temperature steadily increasing. The only difference was in the magnitudes: $n_e = 2.88 \pm 0.58$ x 10^{15} m^{-3} at 37.5 mm and $T_e = 2.2 \pm 0.22$ eV at 25 mm. The refined Orbital Motion Limit theory also called the Laframboise method was also done and resulted in similar results, but with significantly higher standard deviations: $n_e = 3.96 \pm 2.1$ x $10^{15} m^{-3}$ at 30 mm and $T_e = 0.88 \pm 0.13$ eV.

Once the COMSOL model was shown to produce results matching the Langmuir probe measurements it was expanded to the higher pressures and voltages of the plasma treatments, i.e. 392 mTorr and -0.75 kV, -0.875 kV, and -1.0 kV. The COMSOL Particle Tracing Module was then implemented taking the final solution of the electric potential as

input to find the Incident Ion Angular Energy Distribution Functions as they impact the cathode. This produced relatively stable average particle kinetic energies, ~24 eV, and a ma

This produced relatively stable average particle kinetic energies, 24.4 eV, 21.3 eV, and 25.2 eV, and a slight increase in maximum particle kinetic energy, 736 eV, 951.1 eV, and 921 eV, for the increasing voltages. The Ion Energy Probability Functions were also found and showed what appeared to be two linear Maxwellian sections. Linear fits were done to obtain electron temperatures as the cathode voltage increased, they showed little change and hovered around 7-8 eV and 55 eV for the respective low and high energy fitting windows.

Modeling a deuterium discharge was saved for last due to not being able to validate it with Langmuir probe measurements. Simulating a hydrogen plasma is difficult on its own as it has a far more complex set of reaction pathways including ionizations, electron attachments, excited atoms and molecules, dissociations, etc. Additionally, deuterium poses isotropic differences in its vibrational and rotational energy levels leading to different cross sections the affected reactions, i.e. dissociation and excitations. These considerations were taken into account and resulted in a plasma chemistry consisting of 28 reactions, not including the de-excitation reactions, and 10 surface reactions.

The same modules were used along with the Particle Trajectories module for estimating incident ion energies in a 392 mTorr plasma. The particle statistics showed a direct dependence to the cathode voltage with the highest average and maximum particle kinetic energies of 160.3 eV add 988.2 eV respectively - refer back to Table 11 for the other data on average particle kinetic energy and maximum particle kinetic energy. The IEPFs also showed a more affected trend with increasing voltage for both low and high energy windowed linear

fits with the low energy temperature going from 5 eV to 13 eV and the high energy temperature going from 130 eV to 273 eV. Lastly, in an attempt to further increase the ion energies, a simulation was done at 85 mTorr. This produced the highest average and maximum particle energies of 288.42 eV and 1005.2 eV and low and high-temperature linear fits of 9.3 eV and 376 eV.

The TDS results showed deuterium desorption between 600 − 800 K which is below the high binding energy sites shown in Figure 17 with desorption temperatures between 1000 − 1200 K. For low fluence, increasing voltage led to enhanced deuterium trapping, but an increase in pressure had a more drastic effect. As the fluence increased, the voltage and pressure had an inverse relationship with trapped deuterium.

SEM and TEM images were taken of various samples and displayed what appeared to be surface holes or pits and swelling which increased in concentration with fluence. Cross section images revealed that the swelled structures had holes and voids in them. These subsurface expansions were purported to cause the swelling behavior and led credence to refer to the structures more as blisters, similar to that found in helium irradiation of metals. A postulate is that these structures are what contain the deuterium, and with a high enough damage production rate or absorption rate of deuterium, they either are damaged or grow to such an extent that they inevitably rupture.

The TEM images also introduce a concern on the possibility that the deeper voids and grain boundaries result from incident ions. They show the damage propagating only ~250 nm into the surface, while the SEM images show defects and grains ~1 μm beneath the surface. SRIM studies also produced depth ranges of ~250 nm suggesting the structures extending further from the surface do not result from incident ions. In light of

this, a suggestion was that the incident ions could channel deeper into the bulk similar to the ion-channeling method previously mentioned in 1.1 Palladium - Hydrogen Properties. Then thermal processes could lead to hydrogen α-β phase interfaces with concentration gradients and accompanying stresses. While this seems plausible, a simpler explanation is that the deeper defects were already present in the materials received from the manufacturer and not enough cross-section SEM locations were studied to expose them.

5.2 Future Work

Multiple paths of future work can be taken: extending the plasma parameters to various pressures and voltages, including new analytical measurement tools, or focusing on computational methods attempting to simulate the deuterium-metal interaction. The first would be the simplest to perform, and some promising results are currently underway. Below is a TDS for -1.0 kV at 1.0 Torr for $2 \times 10^{20} \text{ions/cm}^2$ which shows a stark deuterium peak at high temperature and is reminiscent of Figure 17.

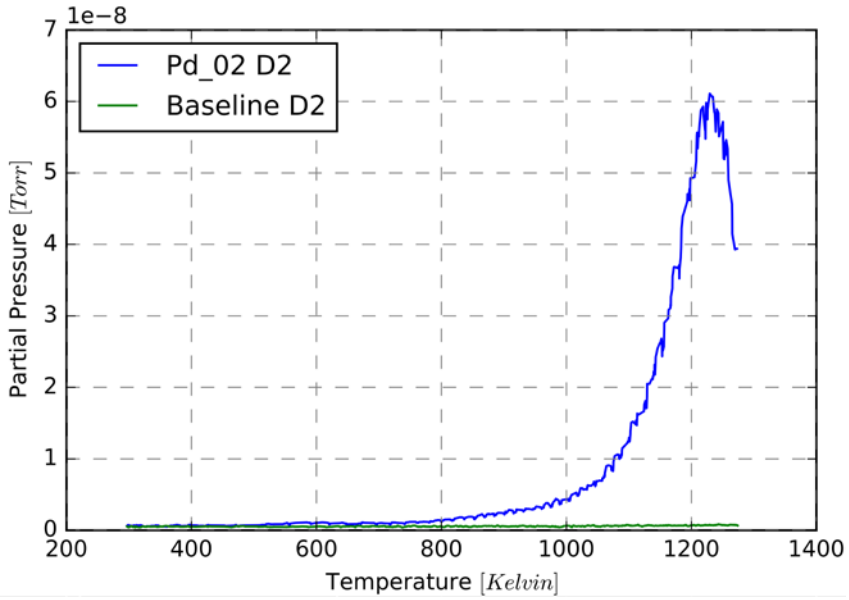

Figure 86. TDS for $2\,x\,10^{20} ions/cm^2$ at -1.0 kV and 1.0 Torr

The operational parameters would also have to be modified along with the electrode's gap distance to achieve a collisionless plasma for deuterium which would allow using the Druyvesteyn method for EEDF measurements. The comparison of the measured and simulated EEDFs would aid in the validation of the COMSOL model for the incident ion energies.

It would be beneficial to determine what was the origin of the circular grains $\sim 0.35 - 1\mu m$ beneath the surface after ion bombardment. It is possible they were present in the as-received foils from Alfa Aesar, but the multiple cross-sections taken did not display any. Seeing as cracks appeared near these grains and those at lower depths $\sim 0.35\mu m$ being in the range of damage production as shown through TEM, these could be due to hydrogen absorption and stresses forming from α-β interfaces. Explaining the formations at increased depths is more difficult assuming they are due to the ions and relies on ion-channeling type effects for the particles to reach further into the material. A more straightforward explanation is the grain structures were already present in the material and not enough SEM sites were studied to uncover them. Future TEM samples could be prepared that include the different grain structures and measuring the lattice constants would provide insight on their origin.

New analytical equipment such as a Retarding Potential Analyzer (RPA) could be implemented. This consists of a series of biased grids that can measure the ion distribution if adequately utilized which it would be difficult to do for a DC glow discharge in the current chamber's confined space.

The project identified the plasma-metal interaction as a topic requiring further investigation analytically. The work outlined here used the Binary Collision Approximation (BCA) software SRIM to gain estimates of sputtering and subsurface vacancy creation and ion implantation depth. While computationally inexpensive, this

methodology does not take into account atomistic multi-bodied interactions which become significant for lower energy incident ions as is the case at a plasma-metal interface. It also does not take into account the athermal interactions affecting the thermodynamics of the system which in turn affect the athermal kinetics resulting in a type of feedback loop. Incorporating these effects into a computational study would be difficult but would drastically increase its accuracy. It requires coupling plasma dynamics to atomistic processes occurring at the plasma-material interface, and COMSOL's continuum based Plasma Module is not in its current form capable of the task.

A particular computational method that would immediately be elucidating for damage depth profiles would be further SRIM studies using energy distributions as input parameters. The current SRIM method used only had one ion energy and the damage cascades were computed for a set number of particles, but the COMSOL simulations showed the ion energies have broad energy ranges.

Another computational avenue would be pursuing the formation of the blister type structures similar to studies being done on the retention of helium in tungsten. These would present different problems as it is the insolubility of helium that leads to its coalescence forming bubbles whereas deuterium is effortlessly soluble in palladium. The mechanism for the blister and void production could, therefore, be entirely different. These models typically rely on Monte Carlo approaches, but it might be necessary first to compute DFT models to produce proper correlation functions between energetic ions entering the lattice and deuterium occupied defects.

References

[1] G. Alefeld *et al.*, *Hydrogen in Metals I*. Berlin: Springer Berlin Heidelberg, 1978.

[2] J. P. Hirth, J. Lothe, and T. Mura, "Theory of Dislocations," *Journal of Applied Mechanics*, vol. 50, no. 2. p. 476, 1983.

[3] Comsol, "Introduction to Plasma Module," 2013.

[4] Y. Fukai, *The Metal-Hydrogen System: Basic Bulk Properties*, vol. 21. Springer Berlin Heidelberg, 2006.

[5] T. Graham, "On the Absorption and Dialytic Separation of Gases by Colloid Septa," *Philos. Trans. R. Soc. London Giv. Some Accounts Present Undertakings, Stud. Labours, Ingenious, Many Considerable Parts World*, vol. 53, no. v. 156, pp. 1689-1699, 1866.

[6] C. Wagner, "The kinetics of the H-2 (Gas) 2H (dissolved in Pd) reaction.," *Zeitschrift für Phys. Chemie. Abteilung A, Chem. Thermodyn. Kinet. Elektrochemie, Eig.*, vol. 159, no. 6, pp. 459-469, 1932.

[7] E. Wicke, H. Brodowsky, and H. Züchner, "Hydrogen in palladium and palladium alloys," in *Hydrogen in Metals II: Application-Oriented Properties*, G. Alefeld and J. Völkl, Eds. Berlin, Heidelberg: Springer Berlin Heidelberg, 1978, pp. 73-155.

[8] T. B. Flanagan, R. Balasubramaniarn, and R. Kirchheim, "Exploring lattice defects in palladium and its alloys using dissolved hydrogen. Part I: Hydrogen solubility and its segregation to dislocations and vacancies," *Platin. Met. Rev.*, vol. 45, no. 3, pp. 114-121, 2001.

[9] S. M. Myers *et al.*, "Hydrogen interactions with defects in crystalline solids," *Rev. Mod. Phys.*, vol. 64, no. 2, pp. 559-617, 1992.

[10] K. Momma and F. Izumi, "VESTA: A three-dimensional visualization system for electronic and structural analysis," *J. Appl. Crystallogr.*, vol. 41, no. 3, pp. 653-658, 2008.

[11] H. Okuyama, W. Siga, N. Takagi, M. Nishijima, and T. Aruga, "Path and mechanism of hydrogen absorption at Pd(100)," *Surf. Sci.*, vol. 401, no. 3, pp. 344-354, 1998.

[12] M. Lischka and a Groß, "Hydrogen on palladium: a model system for the interaction of atoms and molecules with metal surfaces," *Recent Dev. Vac. Sci. Technol.*, vol. 661, no. 2, pp. 111-132, 2003.

[13] X. T. Zu *et al.*, "Properties of helium defects in bcc and fcc metals investigated with density functional theory," *Phys. Rev. B - Condens. Matter Mater. Phys.*, vol. 80, no. 5, pp. 1-6, 2009.

[14] J. K. Nørskov, "Electron structure of single and interacting hydrogen impurities in free-electron-like metals," *Phys. Rev. B*, vol. 20, no. 2, pp. 446-454, 1979.

[15] J. Roques, C. Lacaze-Dufaure, and C. Mijoule, "Dissociative adsorption of hydrogen and oxygen on palladium clusters: A comparison with the (111) infinite surface," *J. Chem. Theory Comput.*, vol. 3, no. 3, pp. 878-884, 2007.

[16] T. B. Flanagan and W. A. Oates, "The Palladium-Hydrogen System," *Annu. Rev. Mater. Sci.*, vol. 21, no. 1, pp. 269-304, 1991.

[17] C. A. Wert, "8. Trapping of hydrogen in metals.," *Hydrog. Met. II. Appl. Prop.*, p. 305-330 [1-2], 1978.

[18] Y. Sakamoto, K. Takai, I. Takashima, and M. Imada, "Electrical resistance measurements as a function of composition of palladium - hydrogen(deuterium)

systems by a gas phase method," *J. Phys. Condens. Matter*, vol. 8, no. 19, pp. 3399-3411, 1999.

[19] Y. Fukai and N. Okuma, "Formation of Superabundant Vacancies in Pd Hydride under High Hydrogen Pressures," vol. 73, no. 12, pp. 1640-1643, 1994.

[20] S. M. Myers, P. M. Richards, D. M. Follstaedt, and J. E. Schirber, "Superstoichiometry, accelerated diffusion, and nuclear reactions in deuterium-implanted palladium," *Phys. Rev. B*, vol. 43, no. 12, pp. 9503-9510, 1991.

[21] M. Nastasi, J. W. Mayer, and J. K. Hirvonen, *Ion-Solid Interactions: Fundamentals and Applications*. Cambridge: Cambridge University Press, 1996.

[22] J. F. Ziegler, J. P. Biersack, and M. D. Ziegler, *SRIM, the Stopping and Range of Ions in Matter*. SRIM Company, 2008.

[23] J. F. Lynch, J. D. Clewley, and T. B. Flanagan, "The formation of voids in palladium, metal by the introduction and removal of interstitial hydrogen," *Philos. Mag.*, vol. 28, no. 6, pp. 1415-1418, 1973.

[24] F. Besenbacher, B. B. Nielsen, J. K. Nørskov, S. M. Myers, and P. Nordlander, "Interaction of hydrogen isotopes with metals: Deuterium trapped at lattice defects in palladium," *J. Fusion Energy*, vol. 9, no. 3, pp. 257-261, 1990.

[25] T. B. Flanagan, J. F. Lynch, J. D. Clewley, and B. Von Turkovich, "The effect of lattice defects on hydrogen solubility in palladium. I. Experimentally observed solubility enhancements and thermodynamics of absorption," *J. Less-Common Met.*, vol. 49, no. C, pp. 13-24, 1976.

[26] H. Ibach and H. Lüth, *Solid-State Physics An Introduction to Principles of Materials Science*. 2009.

[27] C. Kittel and P. McEuen, *Introduction to solid state physics*, vol. 8. 1986.

[28] B. J. Heuser and J. S. King, "Effect of Dislocation Trapping on Deuterium Diffusion in Deformed, Single Crystal Pd," *Metall. Mater. Trans. A*, vol. 29A, no. June, p. 1593, 1998.

[29] W. C. Chen, B. J. Heuser, and J. S. King, "Small-angle neutron scattering investigation of deuteride (hydride) precipitation and decomposition in single-crystal Pd," *J. Appl. Crystallogr.*, vol. 33, no. 3 I, pp. 442-446, 2000.

[30] B. J. Heuser, D. R. Trinkle, D. R. Yang, and L. He, "Hydrogen trapping at dislocation cores at room temperature in deformed Pd," *J. Alloys Compd.*, vol. 577, pp. 189-191, 2013.

[31] R. Kirchheim, "Interaction of hydrogen with dislocations in palladium-II. Interpretation of activity results by a fermi-dirac distribution," *Acta Metall.*, vol. 29, no. 5, pp. 845-853, 1981.

[32] A. G. Lipson, B. J. Heuser, C. H. Castano, B. F. Lyakhov, and A. Y. Tsivadze, "Magnetic characterization of a hydrogen phase trapped inside deep dislocation cores in a hydrogen-cycled PdH x (x ≈ 4.5 × 10−4) single crystal," *J. Exp. Theor. Phys.*, vol. 103, no. 3, pp. 385-397, 2006.

[33] M. Maxelon, A. Pundt, W. Pyckhout-Hintzen, J. Barker, and R. Kirchheim, "Interaction of hydrogen and deuterium with dislocations in palladium as observed by small angle neutron scattering," *Acta Mater.*, vol. 49, no. 14, pp. 2625-2634, 2001.

[34] J. H. Evans, "The role of implanted gas and lateral stress in blister formation mechanisms," *J. Nucl. Mater.*, vol. 76-77, no. Supplement C, pp. 228-234, 1978.

[35] G. H. Miley, A. Lipson, N. Luo, H. Hora, and P. J. Shrestha, "DPD cluster reactions in low energy nuclear reactions (LENRS)," *AIP Conf. Proc.*, vol. 1154, p. 82, 2009.

[36] R. Kirchheim, "Solid solutions of hydrogen in complex materials," *Solid State Phys. - Adv. Res. Appl.*, vol. 59, no. C, pp. 203-291, 2004.

[37] N. W. Ashcroft, "Hydrogen dominant metallic alloys: High temperature superconductors?," *Phys. Rev. Lett.*, vol. 92, no. 18, pp. 187002-1, 2004.

[38] G. Alefeld *et al.*, *Hydrogen in Metals II*. Berlin: Springer Berlin Heidelberg, 1978.

[39] R. A. Huggins, "Materials Aspects of the Electrochemical Insertion of Hydrogen and Deuterium Into Mixed Conductors," in *Fourth International Conference on Cold Fusion*, 1993.

[40] A. G. Lipson, B. J. Heuser, C. H. Castano, and A. Celik-Aktas, "Observation of a low-field diamagnetic contribution to the magnetic susceptibility of deformed single crystal PdHx (x = 4.0 x 10-4)," *Phys. Lett. Sect. A Gen. At. Solid State Phys.*, vol. 339, no. 3-5, pp. 414-423, 2005.

[41] V. a Godyak and V. I. Demidov, "Probe measurements of electron-energy distributions in plasmas: what can we measure and how can we achieve reliable results?," *J. Phys. D. Appl. Phys.*, vol. 44, no. 26, p. 269501, 2011.

[42] M. A. Lieberman and A. J. Lichtenberg, *Principles of Plasma Discharges and Materials Processing*. Wiley, 2005.

[43] V. A. Godyak and B. M. Alexandrovich, "Comparative analyses of plasma probe diagnostics techniques," *J. Appl. Phys.*, vol. 118, no. 23, 2015.

[44] M. J. Druyvesteyn and F. M. Penning, "The mechanism of electrical discharges in gases of low pressure," *Rev. Mod. Phys.*, vol. 12, no. 2, pp. 87-174, 1940.

[45] F. Magnus and J. T. Gudmundsson, "Digital smoothing of the Langmuir probe Digital smoothing of the Langmuir probe I - V characteristic," vol. 73503, 2008.

[46] T. K. Popov *et al.*, "Second derivative Langmuir probe diagnostics of gas discharge

plasma at intermediate pressures (review article)," *J. Phys. Conf. Ser.*, vol. 44, pp. 60-69, 2006.

[47] Fridman, "Electron energy distribution function measurements and plasma parameters in inductively coupled argon plasma," *Plasma Sources Sci. Technol*, vol. 11, pp. 525-543, 2002.

[48] M. U. A. Bromba and H. Ziegler, "Application hints for Savitzky-Golay digital smoothing filters," *Anal. Chem.*, vol. 53, no. 11, pp. 1583-1586, 1981.

[49] M. Boudart, "Heterogeneous Catalysis By Metals," *J. Mol. Catal.*, vol. 30, pp. 27-38, 1985.

[50] T. B. Flanagan, D. Wang, and K. Shanahan, "The effect of CO on hydrogen permeation through Pd and through internally oxidized and un-oxidized Pd alloy membranes," *Sep. Purif. Technol.*, vol. 79, no. 3, pp. 385-392, 2011.

[51] Z. P. Liu and P. Hu, "General rules for predicting where a catalytic reaction should occur on metal surfaces: A density functional theory study of C-H and C-O bond breaking/making on flat, stepped, and kinked metal surfaces," *J. Am. Chem. Soc.*, vol. 125, no. 7, pp. 1958-1967, 2003.

[52] V. Ersion, "Plasma Module," *Interfaces (Providence).*, 2013.

[53] A. L. Manual, "Mixer Module Application Library Manual," 2013.

[54] D. N. Ruzic, W. Weed, and A. V. Society., *Electric probes for low temperature plasmas TT* -. New York : American Vacuum Society,.

[55] V. A. Godyak, R. B. Piejak, and B. M. Alexandrovich, "Probe diagnostics of non-Maxwellian plasmas," *J. Appl. Phys.*, vol. 73, no. 8, pp. 3657-3663, 1993.

[56] J. Liu and M. Zhang, "Two-Dimensional Simulation of Hydrogen Direct-Current Discharge Plasma," *Plasma Sci. Technol.*, vol. 14, no. 8, pp. 693-698, 2012.

[57] T. Kimura and H. Kasugai, "Properties of inductively coupled rf Ar/ H2 plasmas: Experiment and global model," *J. Appl. Phys.*, vol. 107, no. 8, 2010.

[58] J.-S. Yoon *et al.*, "Electron-impact cross sections for deuterated hydrogen and deuterium molecules," *Reports Prog. Phys.*, vol. 73, no. 11, p. 116401, 2010.

[59] R. K. Janev, D. Reiter, and U. Samm, "Collision Processes in Low-Temperature Hydrogen Plasmas," *Sci. York*, p. 190, 2003.

APPENDIX

A1. Standard Deviation

$$\sigma = \sqrt{\frac{1}{N}\sum_{i=1}^{N}(x_i - \mu)^2}, \qquad where \qquad \mu = \frac{1}{N}\sum_{i=1}^{N} x_i \tag{A2.1}$$

A2. Ideal Maxwellian Current

Beginning with a normalized Maxwellian distribution given by (2.5) and setting it equal to (2.7) where a negative sign is added to represent negative current being from electrons

$$\frac{2}{(kT_e)^{\frac{3}{2}}}\sqrt{\frac{\epsilon}{\pi}}exp\left(-\frac{\epsilon}{kT_e}\right) = \frac{-4}{e^2 A_p}\sqrt{\frac{m_e V}{2e}}\frac{d^2 I}{dV^2} \tag{A3.2}$$

The right hand side needs to have a change in variables from V to ϵ.

$$\epsilon = -e\left(\phi_p - V_p\right), d\epsilon = edV, \qquad where\ V = \phi_p - V_p \tag{A3.3}$$

Using these relations and solving for $d^2I/d\epsilon^2$

$$\frac{d^2 I}{d\epsilon^2} = -\frac{aeA_p}{4}\sqrt{\frac{2}{m_e}}\exp\left(-\frac{\epsilon}{kT_e}\right), \qquad where\ a = \frac{2\pi}{(\pi kT_e)^{\frac{3}{2}}} \tag{A3.4}$$

This is integrated with respect to ϵ

$$\frac{dI(V)}{d\epsilon} = -\frac{aeA_p}{4}\sqrt{\frac{2}{m}}\int_{\epsilon}^{\infty} exp\left(-\frac{\epsilon'}{kT_e}\right)d\epsilon' = -\frac{aeA_p}{4}\sqrt{\frac{2}{m}}\left(kT_e \exp\left(-\frac{\epsilon}{kT_e}\right)\right) \tag{A3.5}$$

Integrating again with respect to ϵ

$$I(V) = -\frac{aeA_p}{4}\sqrt{\frac{2}{m}}\left((kT_e)^2 \exp\left(-\frac{\epsilon}{kT_e}\right)\right) \tag{A3.6}$$

$$= \frac{2\pi}{(\pi kT_e)^{\frac{3}{2}}}\frac{eA_p}{4}\sqrt{\frac{2}{m}}\left((kT_e)^2 \exp\left(-\frac{\epsilon}{kT_e}\right)\right)$$

Which is simplified to

$$I(V_{probe}) = -eA_p\sqrt{\frac{kT_e}{2\pi m_e}}\exp\left(\frac{e(\phi_p - V_p)}{kT_e}\right) \tag{A3.7}$$

A3. Ideal Druyvesteyn Current

Beginning with a normalized Druyvesteyn distribution given by (2.6) and setting it equal to (2.7) where a negative sign is added to represent negative current being from electrons

$$\frac{0.5648}{(kT_e)^{\frac{3}{2}}}\sqrt{\epsilon}\, exp\left(-0.243\left(\frac{\epsilon}{kT_e}\right)^2\right) = \frac{-4}{e^2A_p}\sqrt{\frac{m_eV}{2e}}\frac{d^2I}{dV^2} \tag{A3.8}$$

As before, a change in variables is made for the right hand from V to ϵ.

$$\epsilon = -e(\phi_p - V_p), d\epsilon = edV, \qquad where\ V = \phi_p - V_p \tag{A3.9}$$

Using these relations and solving for $d^2I/d\epsilon^2$

$$\frac{d^2I}{d\epsilon^2} = -\frac{aeA_p}{4}\sqrt{\frac{2}{m_e}}\exp\left(-0.243\left(\frac{\epsilon}{kT_e}\right)^2\right), \qquad where\ a = \frac{0.5648}{(kT_e)^{\frac{3}{2}}} \tag{A3.10}$$

This is integrated with respect to ϵ

$$\frac{dI(V)}{d\epsilon} = -\frac{aeA_p}{4}\sqrt{\frac{2}{m}}\int_{\epsilon}^{\infty} exp\left(-0.243\left(\frac{\epsilon'}{kT_e}\right)^2\right)d\epsilon' \tag{A3.11}$$

$$= \left[C_1 1.7978kT_e\, erf\left(\frac{0.49295\epsilon'}{kT_e}\right)\right]_{\epsilon}^{\infty}$$

$$= C_1\left(1.7978kT_e - 1.7978kT_e\,\mathrm{erf}\left(\frac{0.49295\epsilon}{kT_e}\right)\right)$$

Integrating again with respect to ϵ

$$I(V) = C_1 1.7978kT_e\int_{\epsilon}^{\infty}\left(1 - erf\left(\frac{0.49295\epsilon'}{kT_e}\right)\right)d\epsilon' \tag{A3.12}$$

$$= C_1 1.7978kT_e\left[-\epsilon'\mathrm{erf}(\frac{0.493\epsilon'}{kT_e} - 1.1445kT_e\exp(-0.243'\right]_{\epsilon}^{\infty}$$

$$= C_1 1.7978kT_e\left[\epsilon\,\mathrm{erf}\left(\frac{0.493\epsilon}{kT_e}\right)\right.$$

$$\left. + 1.1445kT_e\exp\left(-0.243\left(\frac{\epsilon}{kT_e}\right)^2\right) - \epsilon\right]$$

A4. Deuterium Reactions and Electron Energy Losses

Table 16. Relevant reactions, their type, and their electron energy loss - de-excitation reactions are not shown to conserve space - it is to be assumed that whenever an excitation reaction occurs there is an associated de-excitation reaction unless specified as irreversible

Reaction	Formula	Type	$\Delta\epsilon$ [eV]
1	$e + D \rightarrow e + D_2$	Elastic	0

2	$e + D_2 \rightarrow 2e + D_2^+$	Ionization	15.467
3	$e + D_2 \rightarrow e + D + D$	Excitation	8
4	$e + D \rightarrow e + D(2p)$	Excitation	10.2
5	$e + D \rightarrow e + D(2s)$	Excitation	10.2
6	$e + D \rightarrow e + D(n = 3)$	Excitation	12.3
7	$e + D(2s) \rightarrow e + D(2p)$	Irreversible Excitation	1.93×10^{-5}
8	$e + D(2s) \rightarrow e + D(n = 3)$	Irreversible Excitation	1.889
9	$e + D(2p) \rightarrow e + D(n = 3)$	Irreversible Excitation	1.889
10	$e + D \rightarrow 2e + D^+$	Ionization	13.6
11	$e + D(2s) \rightarrow 2e + D^+$	Ionization	3.4
12	$e + D(2p) \rightarrow 2e + D^+$	Ionization	3.4
13	$e + D(n = 3) \rightarrow 2e + D^+$	Ionization	1.51
14	$e + D^+ \rightarrow D$	Attachment	
15	$e + D^+ \rightarrow D(2s)$	Attachment	
16	$e + D^+ \rightarrow D(2p)$	Attachment	
17	$e + D^+ \rightarrow D(n = 3)$	Attachment	
18	$e + D_2 \rightarrow e + D_2 B^1\Sigma_u^+$	Excitation	12.754
19	$e + D_2 \rightarrow e + D_2 C^1\Pi_u$	Excitation	13.29
20	$e + D_2 \rightarrow e + D_2 E, F^1\Sigma_g^+$	Excitation	13.13
21	$e + D_2 \rightarrow 2e + D + D_2$	Dissociative Ionization	18.15
22	$e + D_2^+ \rightarrow D + D$	Attachment	
23	$e + D_2^+ \rightarrow e + D + D^+$	Irreversible Excitation	14.4

24	$\mathrm{e} + \mathrm{D}_2^+ \rightarrow 2e + D^+ + D^+$	Ionization	15.2
25	$D_2 + D_2^+ \rightarrow D_3^+ + D$	Ion-neutral	
26	$\mathrm{e} + \mathrm{D}_3^+ \rightarrow e + D^+ + D_2$	Irreversible Excitation	14.75
27	$\mathrm{e} + \mathrm{D}_3^+ \rightarrow D + D_2$	Attachment	
28	$\mathrm{D}(2\mathrm{p}) \rightarrow \mathrm{D}$	Spontaneous de-excitation	